Review Article

Nano Research
2023, 16(8): 11054–11083

ISSN 1998-0124 CN 11-5974/O4
https://doi.org/10.1007/s12274-023-5654-6

Advances in microwave absorbing materials with broad-bandwidth response

Susu Bao[§], Meixi Zhang[§], Zhiyuan Jiang (✉), Zhaoxiong Xie, and Lansun Zheng

State Key Laboratory for Physical Chemistry of Solid Surfaces, College of Chemistry and Chemical Engineering, Xiamen University, Xiamen 361005, China

[§] *Susu Bao and Meixi Zhang contributed equally to this work.*

Received: 11 January 2023 / **Revised:** 22 February 2023 / **Accepted:** 8 March 2023

ABSTRACT

Microwave absorbing materials (MAMs) are playing an increasingly essential role in the development of wireless communications, high-power electronic devices, and advanced target detection technology. MAMs with a broad-bandwidth response are particularly important in the area of communication security, radiation prevention, electronic reliability, and military stealth. Although considerable progress has been made in the design and preparation of MAMs with a broad-bandwidth response, a number of challenges still remain, and the structure–function relationship of MAMs is still far from being completely understood. Herein, the advances in the design and research of MAMs with a broad-bandwidth response are outlined. The main strategies for expanding the effective absorption bandwidth of MAMs are comprehensively summarized considering three perspectives: the chemical combination strategy, morphological control strategy, and macrostructure control strategy. Several important results as well as design principles and absorption mechanisms are highlighted. A coherent explanation detailing the influence of the chemical composition and structure of various materials on the microwave absorption properties of MAMs is provided. The main challenges, new opportunities, and future perspectives in this promising field are also presented.

KEYWORDS

microwave absorbing materials, broad-bandwidth response, magnetic–dielectric synergy, morphology control, macrostructure control

1 Introduction

Microwave absorbing materials (MAMs) are a class of materials that have the capacity to convert the energy of microwaves within a certain frequency range into other forms of energy, such as dielectric, magnetic, or thermal energy. In doing so, these materials reduce the scattering cross section of microwaves or attenuate the energy of incident microwaves. With the rapid development of wireless networks, fifth-generation (5G) communications, high-power electronic devices, new-type radars, intelligent transportation systems, and portable digital hardware, MAMs have attracted increasing attention in the fields of communication security, electronic reliability, healthcare, and military stealth [1–11]. In the past decades, research on the design and construction of various novel MAMs with enhanced performance has progressed substantially [12–25]. As shown in Fig. 1, the number of publications related to MAMs shows a trend of accelerating increase year by year, indicating the importance of MAMs.

For practical applications, the ideal MAM should be lightweight and small in thickness, have a strong absorption ability, and have a broad-bandwidth response. Of these characteristics, the broad-bandwidth response is of particular importance. With the development of the 5G technology and the advent of the Internet of Things, the environments in which humans live are increasingly subject to large quantities of microwaves of different frequencies; MAMs with a narrow-bandwidth response are insufficient to meet the growing demand for electromagnetic protection. Furthermore, for use in military stealth-related applications, MAMs are widely used to absorb radar waves and reduce the radar cross section of a given object. However, different radar systems, long-range surveillance, and guidance technologies can be designed to work with different frequencies, such as the L band (1–2 GHz), S band (2–4 GHz), C band (4–8 GHz), X band (8–12 GHz), Ku band (12–18 GHz), K band (18–27 GHz), and Ka band (27–40 GHz). With the scientific progress in microelectronics and other fields, novel advanced anti-stealth radars, such as ultrawide band radars, frequency agile radars, phased array radars, and passive radars, have gradually matured; these technologies lead to new requirements for counter-detection MAMs. Therefore, the development of high-performance MAMs with a broad-bandwidth response is of great significance in both military and civil fields.

When microwave is incident on a material surface, it experiences three processes: reflection, absorption, and transmission. The reflection coefficient is defined as the ratio of reflected wave to incident wave at a reference plane. Bandwidth is the range of frequencies and defined as the difference between the upper and lower frequency components present in a signal ($\Delta\lambda = \lambda_{max} - \lambda_{min}$, where $\Delta\lambda$, λ_{max}, and λ_{min} are bandwidth, maximum waveband, and minimum waveband, respectively). In most of the

Address correspondence to zyjiang@xmu.edu.cn

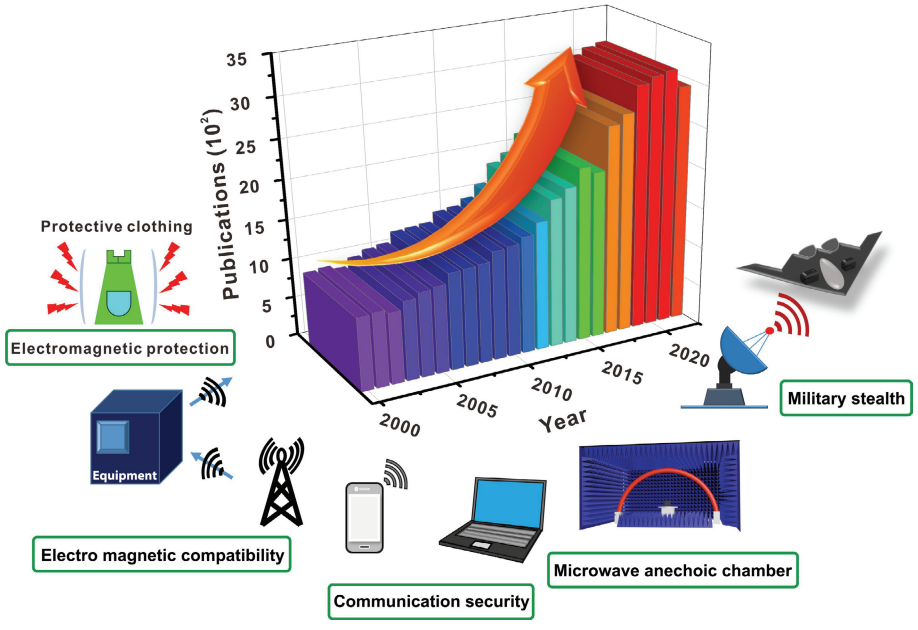

Figure 1 By December 2022, the statistical data comes from the Web of Science, and the retrieval subject is microwave absorption. Some main applications of MAMs are also shown schematically in the figure.

practical applications, due to the existence of backed metal plate, the transmitted wave is reflected at the absorber/metal plate interface and re-enters the absorber. Thus the essence of microwave absorption (MA) by microwave absorbers is anti-reflection. Microwaves in the frequency range of 2–18 GHz are commonly used in the majority of the electronic instruments and military equipment. For example, the operating frequencies of most aviation and marine radars are in the range of 2–18 GHz. Accordingly, MAMs operating in this band have become a focus of considerable research. Usually, the absorption bandwidth with an absorption efficiency greater than 90%, a reflection loss (RL) lower than −10 dB, or a reflectivity below 0.1 is defined as the effective absorption bandwidth (EAB). Considering the effect of microwave absorber on microwave, the broadband microwave absorption means that the absorber can obtain EAB in the wide working band through inherent loss mechanism of the components of the absorber to the microwave, the resonance loss of the thickness of the absorber and the specific microwave frequency, and the reflection cancellation of the microwave at the absorption–reflection interface within the tested frequency range. The largest possible relative bandwidth for a normally incident wave is given by Rozanov et al.: $\Delta\lambda/\lambda_0 = (2R_0)/((\pi d/\lambda_0)|\varepsilon - \mu|)$, where $\Delta\lambda$, λ_0, R_0, d, ε, and μ are bandwidth of a radar absorber, the middle of the operating band of wavelengths, reflectance level, thickness, permittivity, and permeability, respectively [26, 27]. It is shown that the wideband of microwave absorption depends on the thickness, permittivity, and permeability of the absorber within a given operating frequency range. This requires the material to obtain well-match between permittivity and permeability in a wide frequency range [28]. The electromagnetic parameters of the absorber are determined by the shape, size, and content of the MAMs. It is very difficult for a single-layer absorber to achieve multiband absorption at a thin thickness [29]. A nonmagnetic broadband absorber cannot provide effective absorption unless its thickness exceeds $\lambda_{max}/17.2$ [27]. For thin absorbers, there are two main performance limitations: One is the matching of the input impedance to the free-space impedance of any passive absorber that can only be achieved at a specific frequency resulting from the reactance theorem; and the other is the sensitivity of the absorber to incident angle and polarization [30, 31]. In terms of impedance matching, the electromagnetic parameters of materials vary with frequency, so the impedance matching of materials under different frequencies of the same thickness is not the same. Materials usually only have good impedance matching in a specific frequency range, which makes them unable to achieve full-band microwave absorption in 2–18 GHz. As far as the attenuation capability is concerned, it is also true that the material cannot maintain the same attenuation capability at different frequencies. In addition, according to the quarter-wavelength relationship, the impedance matching can only be satisfied in a narrow frequency band near the matching frequency [32, 33]. When the frequency deviates greatly from the matching frequency, the matching performance deteriorates sharply. Thus, it is not easy for a single material to realize broadband and effective MAMs with a small thickness. Therefore, it is difficult to realize effective absorption in broadband. As a result of considerable research efforts, the design of MAMs with a broad-bandwidth response has made great progress in recent years. For example, the EAB of Fe encapsulated within carbon nanotubes (CNTs) can cover the range of 2–18 GHz utilizing a 1.2-mm-thick layer coated on a 180 mm × 180 mm Al substrate [1]. The EAB of Fe_3O_4@Zn-N-carbon microspheres can reach 11.5 GHz using a 2.5-mm-thick layer [34]. Dendrite-like Fe microstructure-based samples have been found to have an EAB of more than 15 GHz in the frequency range of 2–18 GHz [35]. Optimized multiwall CNT (MWCNT)/graphene foam (GF) structures have been found to have an EAB of up to 16 GHz [36]. A microwave metamaterial absorber combining a dual-band absorber and a single-band absorber has achieved an EAB from 1.4 to 17.31 GHz [37]. Considering the type of MAMs, the coating-MAMs are usually composed of absorbent particles and matrix, and the performance is highly dependent on the material composition, morphology, particle size, and distribution of the absorbent [38, 39]. Although the performance of multi-component composites is generally better than that of single-component materials, there are still unclear interactions between different components (which may be synergistic or containment), and the interaction mechanism between materials and microwaves is not clear. Therefore, the coating-absorbents achieved broad-bandwidth response are mainly based on trial-and-error method, so it is urgent to obtain reliable summary from existing experience. For structural-MAMs, enough space can be used to improve the impedance matching, extend the interaction

time between microwaves and structural components, thus improve the performance. However, the actual application scenarios have not plenty of space usually, and it is difficult to obtain the required microwave absorption performance in a specific environment at the expense of the volume of the structural member. In addition, the optimization of the structure, the material composition of the filling structure, and how to reduce the influence of the structure on the shape of the object requiring the use of the absorbing parts also need to be studied. For metamaterials in special structural-MAMs, metamaterial-based absorbers can only display near-perfect absorption at either one frequency or several discretized frequencies due to the inherent resonance-based mechanism of metamaterials and their attendant dispersive characteristics [40]. In addition, the data acquisition from simulations is expensive in terms of time and effort [41]. Therefore, it is necessary to summarize the research points of structural-MAMs with broad-bandwidth response for their future applications and development.

There are already some excellent reviews concerning the advances of MAMs, and most of them focused on introducing MAMs on basis of material categories and structure types, such as metal-organic framework (MOF)-based MAMs [8, 18], graphene-based MAMs [12, 17], and core–shell-structured MAMs [3, 20]. Whereas, the rules and key points for the synthesis and mechanism of MAMs with broad-bandwidth response have not been systematically summarized. Herein, we focus on the recent progresses in the design and construction of MAMs with a broad-bandwidth response, especially related materials that can be used with a specific thickness whose EAB is greater than 8 GHz in the frequency range of 2–18 GHz. We also highlight the methods that can be used to expand the EAB of MAMs. The main body of this review is divided by the typical strategies used in the design and construction of MAMs with a broad-bandwidth response, including the chemical combination strategy, morphological control strategy, and macrostructure control strategy. We present a coherent overview of the influence of the chemical composition and structure of various materials on their MA performances, and some key findings in the field of MAMs as well as the related design principles are discussed. In the last section, we present the challenges and future trends in this research field. This review presents valuable insights into the design and fabrication of high-performance MAMs, especially those with a broad-bandwidth response.

2 Design and construction of MAMs with broad-bandwidth response

2.1 Chemical combination strategy for MAMs with broad-bandwidth response

Traditional MAMs mainly include dielectric materials and magnetic materials. Dielectric materials have a certain absorption of electromagnetic waves due to their high dielectric loss tangent values. However, their permittivity and permeability are usually quite different, resulting in the impedance mismatch and large reflection of electromagnetic waves. Therefore, dielectric materials often need a large thickness to achieve a broad absorption, which are usually used in structural MAMs or microwave anechoic chambers that have low requirements on the thickness of materials. Compared with dielectric MAMs, the permeability dispersion effect and additional magnetic loss of magnetic materials make them more favorable for impedance matching and microwave absorption. Typically, the absorbent composed of flaky carbonyl iron (FCI) particles can achieve more than 85% absorption in the range of 8–18 GHz (corresponding to reflection loss less than −8 dB) at a thickness of only 1.4 mm [42]. Nevertheless, there is still a problem that the high and low frequency absorption cannot be taken into account at the same time, especially the absorption in the range of 2–4 GHz [43–48]. Single-component MAMs have been extensively studied, and the advantages and disadvantages of typical materials have been summarized in Table 1. A practical method to enhance the properties of materials consists of compounding a variety of chemical components into a material system. For example, Li et al. developed a confined liquid–solid redox reaction strategy to fabricate FeCoNi ternary alloy particles with a u-channelled spherical morphology. Owing to the multiple polarization relaxation and magnetic resonances generated by the unique

Table 1 The advantages and disadvantages of typical materials for microwave absorption

Category	MAMs	Advantages	Disadvantages
Carbon materials	Carbon nanotubes	High conductivity, low density, large aspect ratio, and excellent mechanical strength	Poor dispersion, complicated synthesis process, improper conductivity, high cost, and poor impedance matching
	Graphene	Extraordinary electrical, thermal, and mechanical properties, high specific surface area, low content, ultrathin thickness, and abundant defects	
	Biomass-derived carbon materials	Plentiful resources, low density, and highly environment-friendly	Disordered pore structure and limited EAB
	MOF-derived carbon materials	Tunable chemical structures, diverse properties, large specifc surface area, uniform pore distribution, and strong dopability	Simple loss mechanism and limited EAB
Magnetic materials	Carbonyl iron	Good temperature stability, high saturation magnetization (~ 191 emu/g), and strong magnetic loss	High density, corrosion susceptibility, easy to aggregate, strong eddy effect, and snoek's limit of permeability
	Metals and alloys	High saturation magnetization, high conductivity, and high Curie temperature	
	Iron oxides/ferrite	Good magnetic loss ability, environmental stability, strong spin polarization, half-metallic character, corrosion resistance, and low cost	High density, lack of dielectric loss, and limited EAB
Oxides	SiO_2	Good isolation, effective protection of the substrate materials, and low cost	High density, poor conductivity, and narrow EAB
	ZnO	Favorable dielectric, semiconductor properties, low cost, large-scale synthesize, and morphology versatility	
	TiO_2	Excellent chemical stability, semiconductor properties, non-toxic, and low cost	
Ceramics	SiC	Adjustable resistivity, strong oxidation resistance, and high strength	Poor dielectric property and narrow EAB
Others	MXene	Perfectly layered structure, extraordinary electric conductivity, tunable active surface, adjustable layer spacing, and excellent mechanical strength	Simple loss mechanism and limited EAB
Polymers	Polyprrole and polyaniline	Environmental stability, simple preparation, controllable conductivity, non-toxic, strong composability, and high mechanical strength	Poor high-temperature resistance, single loss mechanism, and narrow EAB

structure and multiple magnetic components, the proposed 2.0-mm-thick absorber showed an ultrawide EAB of 9.2 GHz [49]. To construct an effective composite material, the properties and functions of the different components should be complementary or synergistic. The ingenious combination of dielectric loss materials and magnetic loss materials aids the optimization of the impedance matching in a wider frequency range, thus broadening the response bandwidth. For instance, Darvishzadeh and Nasouri coated magnetic Ni particles on the surface of carbon fibers via an electroplating process. The magnetic Ni layer on the carbon fibers not only resulted in the establishment of magnetic properties and an evident magnetic loss performance but also enhanced the electrical conductivity of the composites. Therefore, a wide EAB (5.2–18.0 GHz) of the optimized Ni-coated carbon fiber composite was achieved at a thickness of only 3.0 mm [50]. Traditional magnetic loss materials, such as CI powder, magnetic metals (Fe, Ni, Co, etc., and their corresponding alloys), metal oxides (γ-Fe_2O_3, Fe_3O_4, etc.), and ferrites (MFe_2O_4, with M = Co, Ni, Mn, etc.), generally possess a large saturation magnetization and a high complex permeability in the GHz band and thus have a strong magnetic loss capacity. Among the various dielectric loss materials, graphene and MXene are often used as alternative materials for MAMs due to their large aspect ratios, active chemical surface, tunable electrical properties, abundant functional groups, and varieties of synthesis processes. These features make them the ideal nanosubstrates for hybridization with other lossy materials to realize high-performance microwave attenuation. Thus, the effective assembly of the above materials to obtain MAMs with a broadband response has become an important research direction. The main research results on the design of (1) graphene/magnetic composites, (2) MXene/magnetic composites, and (3) other dielectric/magnetic composites are highlighted below.

2.1.1 *Graphene/magnetic composites*

Graphene is a type of two-dimensional (2D) carbon nanomaterial with a hexagonal honeycomb lattice structure that consists of sp^2-bonded carbon atoms, and its outstanding intrinsic properties (such as ultrathin thickness, light weight, high dielectric constant, and electrical conductivity, as well as good chemical and thermal stability) have made it a research hotpot [51, 52]. The 2D nature and large specific surface area of graphene are conducive to the capture and attenuation of incident microwaves. Furthermore, the multiple polarization relaxation processes induced by the layered structure, functional groups, and residual defects contribute to the significant dielectric loss [53–55]. Therefore, graphene-based materials have become one of the most interesting materials in the field of MA [56–58]. The microwave absorption process in graphene is a result of combined effects of polarization, conductive losses, interfacial, and multiple scattering [29]. However, being a non-magnetic material, sole graphene exhibits a limited loss mechanism, while its high dielectric constant and improper electrical conductivity can easily cause interfacial impedance mismatch without modification or structural optimization, which prevents microwaves from entering the absorbing material [59]. Combining graphene with magnetic materials is the most effective strategy to optimize its impedance matching because the introduction of magnetic components can directly improve the μ_r of the composite and change its input impedance (Z_{in}). At the same time, the magnetic component can provide additional magnetic loss and enhance the attenuation of incident microwaves. For example, Wang et al. prepared G-Fe_3O_4 composites with Fe_3O_4 nanoparticles (NPs) decorated on the surface of graphene sheets [60]. Their results demonstrated that the RL values of the G-Fe_3O_4 nanohybrids were considerably larger than those of pure graphene sheets at 2 mm. Such improved properties are assigned to the interfacial polarization of the Fe_3O_4/graphene interfaces, the uniform distribution of the magnetic NPs and their small size effect, and the cooperation between dielectric loss and magnetic loss. Therefore, introducing magnetic nanostructures into graphene represents a very attractive strategy to develop lightweight high-performance MAMs.

Due to the high electrical conductivity of graphene, the ε_r of the magnetic component/graphene composites is very sensitive to the graphene content; this phenomenon provides a very effective method to adjust the ε_r of the composite and reduce its reflectivity to microwaves [61, 62]. Recently, we successfully fabricated $Co_{15}Fe_{85}$@C/reduced graphene oxide (RGO) multicomponent composites (Figs. 2(a)–2(c)) using $Co_{1-x}Fe_{2+x}O_4$ spheres, phenolic resin (PR), and GO sheets as raw materials. The MA performance of the composite can be easily tailored by controlling the weight ratio of the $Co_{1-x}Fe_{2+x}O_4$ spheres to the GO sheets. The ε_r and attenuation constant of the $Co_{15}Fe_{85}$@C/RGO composites were found to be increased continuously with increasing GO ratio in the raw materials. However, an excessive GO content resulted in a poor impendence matching if ε_r was too high. Only 2 wt.% GO in the raw materials is required for the $Co_{15}Fe_{85}$@C/RGO composites to achieve an optimal EAB of 9.2 GHz at 2.5 mm [61].

To construct magnetic component/graphene composites, one obvious and simple approach is to deposit or grow magnetic particles on the surface of graphene-based nanosheets. Many composites, such as $MnFe_2O_4$/RGO [63], α-Fe_2O_3-RGO [64], RGO-carbonyl iron [65], and CoFeAl-layered double hydroxide (LDH)/graphene hybrids [66], have been obtained in this way. Wang et al. synthesized Fe-Co/NC/RGO composites with a hierarchical structure by first growing an Fe-Co MOF on a cocoon-like RGO and subsequently annealing the obtained system [67]. The introduction of Fe-Co alloys in RGO improved the impedance matching of the composite and increased considerably its magnetic loss ability via hysteresis loss and magnetic resonance; thus, a wide EAB of 9.29 GHz was achieved at 2.63 mm. Additionally, several polymers can be introduced into the composite to obtain MAMs with a broad bandwidth. For example, Liu's research group synthesized $CoFe_2O_4$@polypyrrole (PPy) core–shell structures and bound them to RGO via covalent bond linking to form filled biscuit-shaped $CoFe_2O_4$@PPy-RGO composites (Figs. 2(d)–2(f)) [68]. Benefiting from the synergy of a suitable magnetic loss due to the cobalt ferrite core, a good conduction loss due to the PPy shell, a good dielectric loss due to the RGO, and multiple reflections resulting from the unique structure, the EAB of the as-prepared composites could reach 13.12 GHz at 3.6 mm. Weng et al. synthesized a series of ternary CI/RGO/polyvinyl pyrrolidone (PVP) composites with tunable electromagnetic parameters by simply controlling the PVP content [69]. Thanks to the cooperation of the dielectric and magnetic constituents with the ternary nanostructure, the optimized carbonyl iron/RGO/PVP composites could achieve an EAB of 13.8 GHz at 2.5 mm.

If the magnetic component is in the form of magnetic metal/alloy NPs, a better strategy to increase the oxidation resistance of the composites consists of encapsulating the magnetic NPs in graphene (or few-layer graphite) via chemical vapor deposition (CVD) or high-temperature carbonization. The highly dielectric graphene shell can not only improve the complex permittivity of magnetic NPs, but also prevent to a certain extent the magnetic metal NPs from aggregating, thereby retaining the magnetic loss ability of metal cores at high frequency [70]. For example, Afghahi and Shokuhfar synthesized FeCo@C core–shell NPs via the microemulsion technique and the alcohol catalytic CVD method [70]. Benefiting from the multiple dielectric

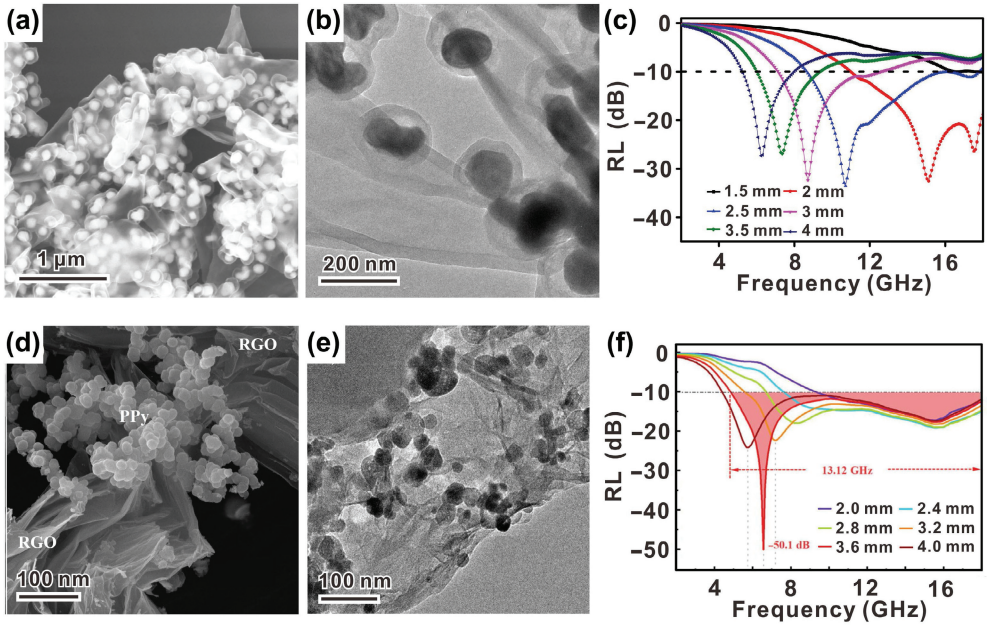

Figure 2 (a) Scanning electron microscopy (SEM) image, (b) TEM image, and (c) RL curves of sandwich-like $Co_{15}Fe_{85}$@C/RGO composites. Reproduced with permission from Ref. [61], © The Royal Society of Chemistry 2020. (d) SEM image, (e) TEM image, and (f) RL curves of $CoFe_2O_4$@PPy-RGO. Reproduced with permission from Ref. [68], © Elsevier Inc 2021.

relaxation resulting from the nanocapsules and the magnetic resonance due to the FeCo NPs, the optimized sample exhibited an EAB of 13.4 GHz at 2.5 mm. Chen's group synthesized nickel NPs wrapped in six-layer N-doped graphene anchored to carbon sheets by heating a mixture of urea and nickel acetylacetonate under Ar atmosphere and then treating it in a hot H_2SO_4 solution. The resulting Ni@N-doped graphene NPs were found to have superior acid corrosion resistance and oxidation resistance, and the EAB of the optimized Ni@NG/NC composite could reach 8.5 GHz at 3.0 mm with a filling ratio of 20 wt.% [71].

Aiming to reveal the enhancement mechanism of graphene coating on the MA performance of magnetic metals, Cui et al. synthesized FeCo-alloy NPs wrapped with single-layer graphene (FeCo@Cs) via the SBA-15 template-assisted CVD method [72]. By varying the absorber thickness, the as-prepared FeCo@Cs could achieve full absorption in the range of 4–18 GHz (Figs. 3(a)–3(c)), while the EAB could reach 8.3 GHz at 2.1 mm. Furthermore, numerical simulations revealed that the tangent direction at the contact point between spheres can largely affect the propagation of the electromagnetic field (Fig. 3(d)). Due to the considerable dielectric loss of graphene, the electric field loss mainly originates from the graphene layer (Fig. 3(e)), while the magnetic field loss is mainly caused by the FeCo core (Fig. 3(f)). Notably, the reflection coefficient of the FeCo spheres encapsulated by multilayer graphene (FeCo@Cm) was significantly larger than the reflection coefficient of FeCo@Cs (Fig. 3(g)). In contrast, the loss density of the electric field (Fig. 3(h)) and the magnetic field (Fig. 3(i)) of FeCo@Cm decreased significantly. These results indicated that a thick graphene shell does not promote microwaves entering the composite; only a single graphene layer can achieve the best match between electric and magnetic fields and lead to a considerable enhancement of the MA performance.

2.1.2 *MXene/magnetic composites*

MXene is a newly-emerged 2D carbon/nitride material, which is usually obtained by removing the A-atom layer of the precursor from the MAX phase of a ternary ceramic [73, 74]. Owing to its perfectly layered structure, extraordinary electric conductivity, tunable active surface, adjustable layer spacing, and excellent mechanical strength, MXene has attracted widespread attention for use as an electromagnetic-interference (EMI) shielding material and a MAM [75–77].

Pure MXene does not exhibit any magnetic loss mechanism, and its MA ability cannot easily meet the requirements of practical applications [77]. In order to obtain MAMs with good impedance matching and strong attenuation ability, it is necessary to add magnetic components to widen the EAB of MXene-based MAMs. As reported by He et al., pure laminated Ti_3C_2 MXene achieved an EAB of only 3.2 GHz because of the lack of magnetic loss and impedance mismatch, while the EAB of $CoFe_2O_4$-decorated Ti_3C_2 MXene composites was up to 8.5 GHz (Figs. 4(a)–4(c)) [78], and FeCo-alloy decorated Ti_3C_2 MXene composites displayed a broad EAB of 8.8 GHz at 1.6 mm [79]. Yan et al. demonstrated that the combination of magnetic NPs and MXene is helpful to expand the EAB of MXene-based materials by introducing magnetic loss mechanisms. By thoroughly blending Ti_3C_2 MXenes with milled FCI using an ultrasonic bath, they fabricated hybrid Ti_3C_2/FCI powders with an optimal EAB of 8.16 GHz at 1.0 mm [80].

Besides incorporating magnetic components to improve the magnetic loss ability, the impedance matching of MXene-based materials can be further optimized through the introduction of oxides and amorphous carbon to realize an excellent MA performance. Feng et al. synthesized an amorphous carbon-supported laminated magnetic composite through the hydrothermal oxidization of nickel-ion-intercalated Ti_3C_2. During the low-temperature oxidation, TiO_2 and NiO NPs were embedded in highly disordered carbon sheets to obtain a sandwich-like structure. The EAB of the layered hybrid NiO&TiO_2@C could reach 11.1 and 9.0 GHz at 3.0 and 2.0 mm, respectively (Figs. 4(d) and 4(e)) [81]. It is believed that the incorporation route is effective to obtain MXene-based MAMs with a broad-bandwidth response.

2.1.3 *Other dielectric/magnetic composites*

Besides graphene and MXene, TiO_2 NPs [82–86], CNTs [87, 88], porous carbon materials [89–91], and ZnO NPs [92–94] are other representative dielectric materials that can also be rationally combined with magnetic components to prepare high-

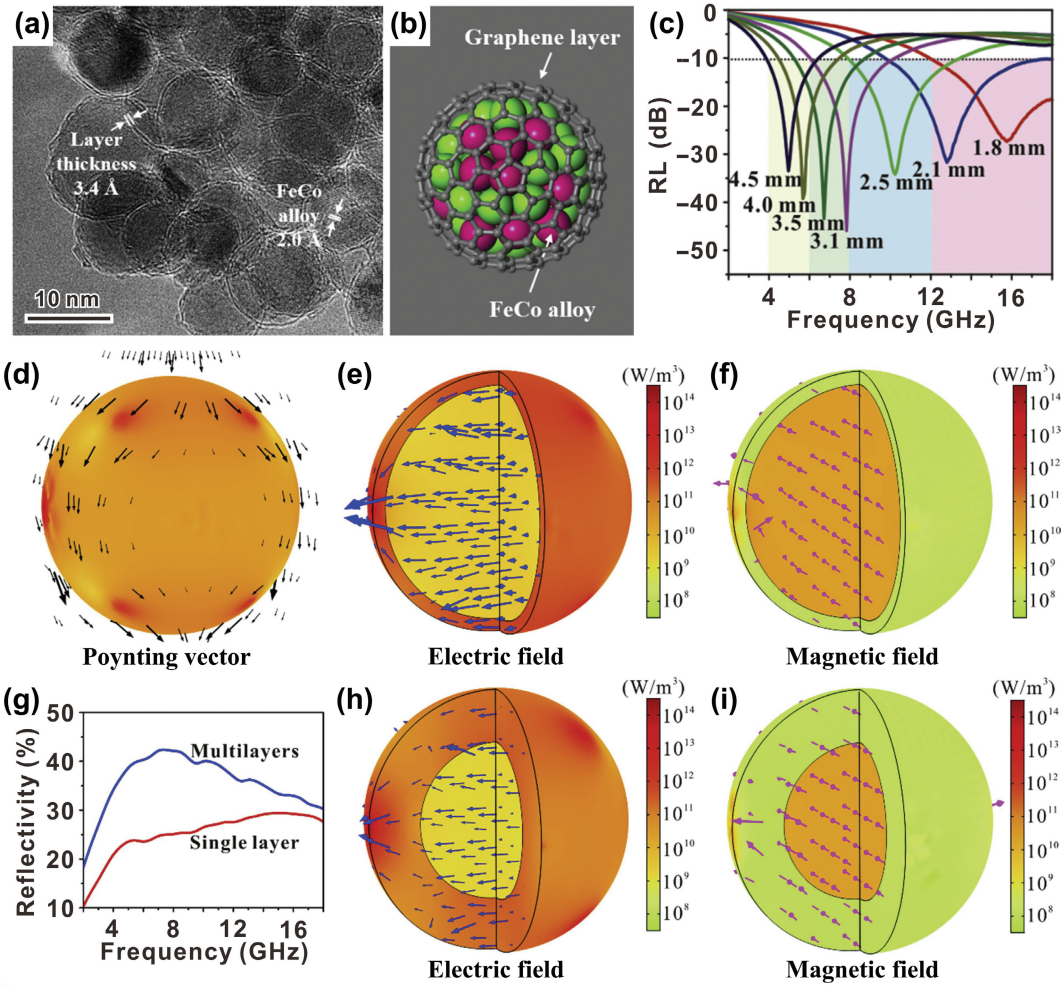

Figure 3 (a) Typical TEM image, (b) a schematic illustration, (c) RL curves of the FeCo@Cs sample, (d) the Poynting vector, (e) the electric field loss and vector, and (f) the magnetic field loss and vector of the FeCo@Cs sphere. (g) The reflection coefficients of FeCo@Cm and FeCo@Cs. (h) The electric field loss and vector and (i) the magnetic field loss and vector of FeCo@Cm. Reproduced with permission from Ref. [72], © Elsevier Ltd. 2021.

performance MAMs.

Pure TiO_2 is not a traditional MAM candidate because of its poor response in the GHz region [95–97]. However, the dipolar polarization and associated relaxation phenomenon induced by polar groups, ions, and oxygen vacancies in TiO_2 can contribute to the occurrence of considerable loss [86–99]. Xia et al. obtained hydrogenated TiO_2 with a strong MA performance by introducing disordered/anatase/rutile interfaces into crystalline TiO_2 via a high-temperature hydrogenation reaction [95]. A creative MA mechanism was proposed, namely the fact that the accumulation and assembled movements of collective interfacial dipoles at the rutile/anatase and crystalline/disordered interfaces are beneficial to the absorption of the electric field energy, thereby further enhancing the MA ability. As a result, the hydrogenated TiO_2 NPs with 8% rutile exhibited outstanding absorption in the range of 4–16 GHz. Furthermore, encapsulating magnetic particles in the TiO_2 shell to form core–shell structures is helpful to enhance the capture and attenuation of the incident microwaves and leads to remarkable MA properties. For example, Che and coworkers prepared Fe_3O_4@TiO_2 core–shell microspheres via a solvothermal reaction and subsequent high-temperature treatment [82]. Due to the cooperation of multiple components and the special core–shell structure, the Fe_3O_4@TiO_2 microspheres possessed an EAB of more than 14 GHz, which is considerably wider than that of pure Fe_3O_4. Hua et al. synthesized dual-shelled Fe_3O_4@TiO_2 hollow nanospheres via a template method [84]. Besides the Debye relaxation and magnetic loss, the accumulation of free charge carriers within multiple heterogeneous interfaces (Fe_3O_4/air and TiO_2/air) promotes the absorption of electric fields by distorting the electric field and increasing the capacitance and loss of the composite. An EAB of 10.5 GHz (7.5–18 GHz) was realized at only 1.8 mm by adjusting the thickness of TiO_2 and the width of the shell gap in the Fe_3O_4@TiO_2 nanocomposites.

CNTs have been widely used as MAMs for their good conductivity, large aspect ratio, and excellent mechanical strength. These features endow them with a tailorable ε_r and permit the construction of lightweight MAMs with good mechanical properties [100, 101]. The combination of CNTs with magnetic metals, magnetic metal oxides, or ferrites has been explored as a strategy to achieve broadband MA through both dielectric and magnetic losses [102–107]. Cao et al. fabricated Fe_3O_4/MWCNT heterostructures by co-precipitating Fe^{2+} and Fe^{3+} ions [87]. The introduction of Fe_3O_4 promoted both the interfacial polarization and the magnetic loss, thus widening the EAB. As a consequence, Fe_3O_4/MWCNT composites exhibited a broad EAB of 11 GHz in the range of 2–18 GHz. By introducing conductive polymers as the matrix, several issues can be solved, such as the oxidation of the magnetic raw materials, poor dispersion, and lack of control of the decoration process of magnetic particles on the surface of the CNTs, while the dielectric loss can be tailored by rationally using the low electrical conductance of polymers. Saeed et al. prepared Fe_2O_3/Fe_3O_4/polyaniline (PANI)/MWCNT quaternary nanocomposites, wherein the Fe_2O_3/Fe_3O_4/PANI nanocomposites were uniformly decorated on the entire surface of the MWCNTs [108]. The different spinel arrangements between Fe_3O_4 and Fe_2O_3 and the noncontinuous arrangement of the Fe_2O_3/Fe_3O_4 NPs in

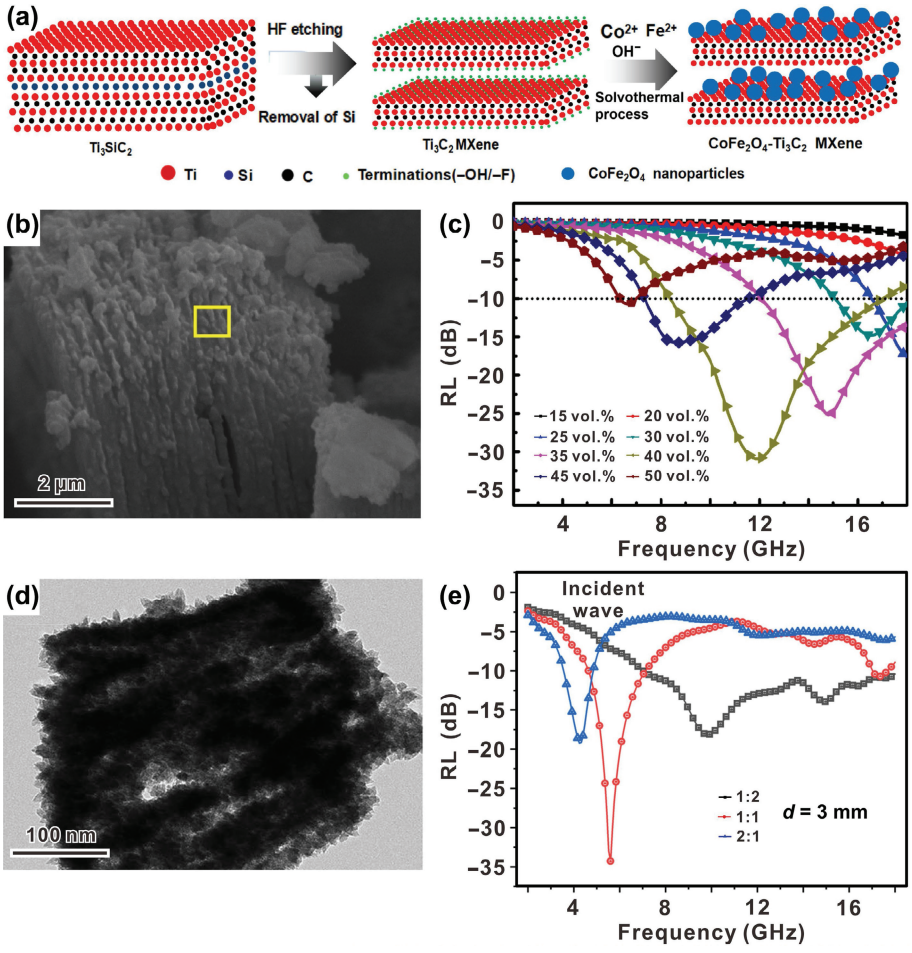

Figure 4 (a) Schematic of the synthetic process for the $CoFe_2O_4$-Ti_3C_2 MXene composite, (b) SEM image, and (c) RL curves of the $CoFe_2O_4$-Ti_3C_2 composite. Reproduced with permission from Ref. [78], © Elsevier B.V. 2019. (d) Typical TEM image and (e) RL curves of NiO&TiO_2@C composite. Reproduced with permission from Ref. [81], © Feng, W. L. et al. 2019.

polyaniline led to an enhanced attenuation of the magnetic field and multiple reflections between the discrete NPs, respectively. The Fe_2O_3/Fe_3O_4/PANI/MWCNT with an optimized ratio of Fe_2O_3/Fe_3O_4/PANI to the nanotubes showed a wide EAB of 8.3 GHz (9.7–18 GHz) at 3.0 mm.

Porous carbon materials with abundant free space and conductive networks, such as porous carbon nanofibers [109], ordered mesoporous carbon [110], biomass-derived porous carbon materials [111], and MOF-derived porous carbon materials [112–114], have been proven to have excellent MA performance because of their strong interfacial polarization and multiple reflections. Among these, MOF-derived porous carbon materials are preferred because of their simple fabrication process, adjustable aperture, and topological diversity [115]. By using MOFs containing magnetic metals as the precursors, nanocomposites with a broad EAB can be obtained. For instance, Wu et al. fabricated nanoporous Co/CoO particles containing hexagonal close packed (hcp)-Co and face centered cubic (fcc)-Co phases via a two-step method [89]. The numerous interfacial polarization processes generated by the existence of many heterogeneous interfaces contribute to the attenuation of the incident microwaves. The optimized sample showed the widest EAB of 8.2 GHz (9.8–18 GHz) at 1.5 mm. Wang et al. synthesized hierarchical nest-like CoFe@C composites using CoFe-MOF-74 as the precursors [90]. An ultrabroad EAB of 9.2 GHz (8.8–18.0 GHz) was achieved by changing the Co/Fe molar ratio in CoFe-MOF-74 (Figs. 5(a)–5(c)). This outstanding MA performance was assigned to the improved impedance matching, increased number of reflections and diffractions of incident microwaves, and multiple polarization relaxation processes due to the residual groups, defects, and different interfaces. On the other hand, the MAMs obtained via the pyrolysis of MOFs usually have a low content of the magnetic components and a poor oxidation resistance, which leads to a poor magnetic loss ability. Therefore, a further modification of metal/carbon composites is required for improving MA properties.

ZnO nanostructures are also considered as promising candidates of MAMs owing to their semiconductor properties, environmentally stable dielectric properties, surface electric polarization effect, morphology versatility, and low cost of their preparation process for commercial application [116–118]. The numerous different morphologies of ZnO nanostructures provide researchers with a sufficiently broad range of materials. Particularly, tetra-needle-like ZnO (T-ZnO) whiskers show excellent MA performance due to the networks formed by T-ZnO, the piezoelectric character of T-ZnO, and the diffuse reflections caused by quasi-antenna [119]. To further improve their MA performance in a wide frequency range, ZnO nanostructures were doped with transition metals or combined with magnetic materials [120, 121]. For example, with increasing dopant concentration, both the ε' and the ε'' of the Mn- and Ni-doped rodlike ZnO samples decreased, and the resonance peaks shifted toward higher frequencies; a wide EAB of 8.6 GHz could be achieved for the 10% Ni-doped sample [120]. Benefiting from the cooperation of dielectric dissipation and magnetic attenuation, the ZnO nanotubes/$CoFe_2O_4$ nanocomposite with 40 wt.% ZnO displayed an EAB of around 9 GHz (Figs. 5(d)–5(f)) [122].

The combination of dielectric and magnetic materials can not only optimize the impedance matching characteristic of materials

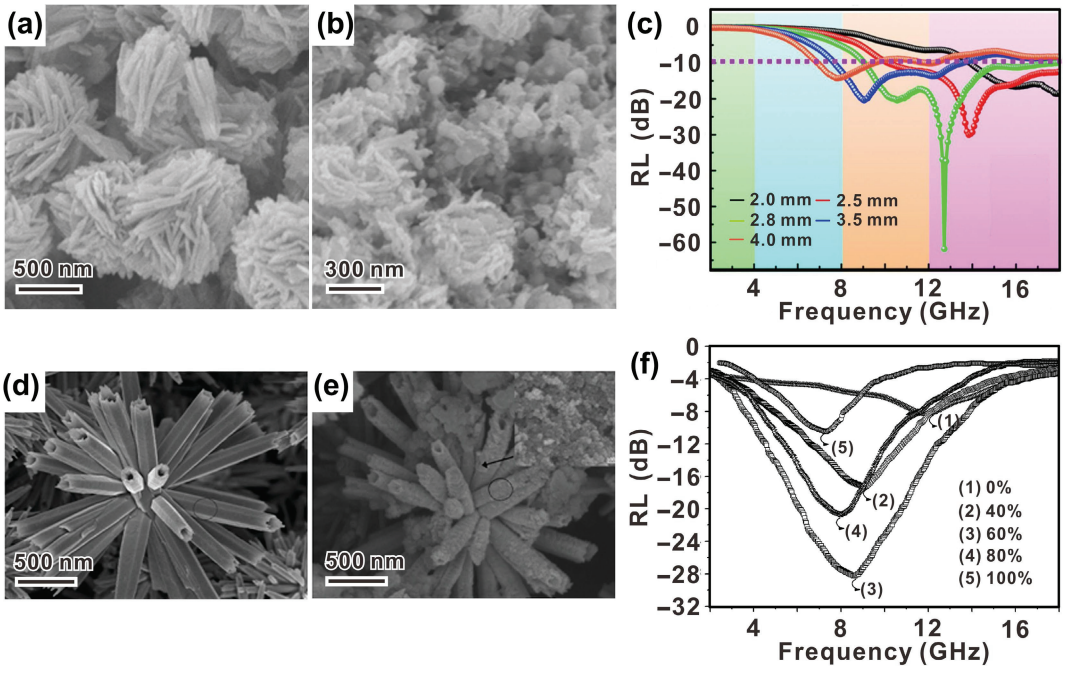

Figure 5 SEM images of (a) CoFe-MOF-74 precursor and (b) CoFe@C composites, and (c) RL values of the CoFe@C composites. Reproduced with permission from Ref. [90], © Elsevier Ltd. 2020. SEM images of (d) ZnO nanotube bundles and (e) ZnO nanotubes/$CoFe_2O_4$ composites, and (f) RL curves of the composites with different contents of ZnO. Reproduced with permission from Ref. [122], © American Chemical Society 2009.

but also combine two forms of energy attenuation mechanisms. Especially, the interface plays an important role in improving the properties of the dielectric/magnetic composites. On the one hand, the difference in Fermi energy levels between two materials will produce an internal electric field, which can greatly promote the migrating and hopping of electrons at the interface and inside the materials, and further enhance the conduction loss [123, 124]. On the other hand, the uneven distribution of positive and negative charges inside the composite can induce the generation of space charge regions. The resulting spatial electric dipoles and generated lattice defects in the composite further excite dipole polarization and interface polarization [125, 126]. Furthermore, the existence of multiple interfaces contributes to the further attenuation of incident electromagnetic waves by enhancing the scattering effect. Consequently, MAMs with a broad-bandwidth response can be obtained through a rational design by effectively controlling the material composition [127, 128]. Some typical cases of MAMs with broad-bandwidth response designed by chemical combination strategy are summarized in Table 2.

2.2 Morphological control strategy for MAMs with broad-bandwidth response

Being able to control the permittivity and permeability is very important to expand the EAB of MAMs. In addition to the intrinsic physical properties of the materials, the microstructure, morphology, grain size, and other characteristics of the individual particles are also closely related to the ε_r and μ_r of materials [129–132]. A reasonable adjustment of these parameters can enhance the attenuation behavior and broaden the EAB of the MAMs [133, 134]. Among the various parameters that can be controlled, the absorbent morphology is one of the most extensively studied features because of its intuitive and adjustable characteristics. For example, materials with a one-dimensional (1D) structure have a larger complex permittivity than zero-dimensional (0D) materials due to the multiple polarization effects [135]; the increased shape anisotropy will improve the ε_r and μ_r of 2D flaky magnetic metals [136]; and the hybrid composites with hollow structures or voids have a better impedance matching performance [137]. The most significant advances in MAMs with specific morphologies, namely the (1) 1D morphology, (2) 2D morphology, and (3) hybrid structure with cavities, are presented below.

2.2.1 *Broadband MAMs with the 1D morphology*

The space charge polarization of a 1D structure is greater than that of a 0D structure due to the high surface ratio of the 1D structure [138]. The high surface atomic utilization, multiple surface hanging bonds, and large unsaturated coordination originate from the higher surface ratio and result in more heterogeneous interfaces and an enhancement of the interfacial polarization [139, 140]. Cheng et al. assembled Cu/ZnO core–shell composites with different morphologies via a simple one-pot process by controlling the heating rate. They demonstrated that the aspect ratio of the hybrid Cu/ZnO nanocomposites has a significant effect on the MA performance because of the anisotropy effect. Compared with the spherical-shaped sample, the intrinsic shape-dependent field induced by charge accumulation at the edge of rod-shaped sample interacts more strongly with the incident microwaves. Therefore, the EAB of rod-shaped Cu/ZnO core–shell composites is wider than that of the spherical Cu/ZnO core–shell nanocomposites [141]. Liu et al. obtained an EAB of around 9.8 GHz using the dipolar polarization and interfacial polarization of helical carbon nanofiber-coated carbon fibers [142]. In addition, the orientation polarization of the 1D structure resulting from the shape anisotropy further improves the complex permittivity of the materials [143]. For example, the complex permittivity of rod-like Fe_3O_4 is considerably higher than that of spherical Fe_3O_4 (Figs. 6(a)–6(d)) [135]. The enhanced interfacial polarization and dipole polarization endow 1D SiC@C hybrid nanowires with an EAB of 8 GHz (Figs. 6(e) and 6(f)) [144]. Huang et al. synthesized a ternary core–shell heterostructure by embedding Fe_7S_8 NPs between S-doped carbon nanoshells and carbonized bacterial cellulose nanofibers. Owing to the enhancement of the multiple interfacial polarization and sulfur dipolar polarization, the ternary composites achieved an EAB of 8.5 GHz at a low loading content (5.0 wt.%) [145].

Additionally, a crosslinked network can form more easily in a 1D structure than in a 0D structure, which may cause the

Table 2 Typical cases of MAMs with broad-bandwidth response designed by chemical combination strategy

Chemical combination strategy	MAMs	Max EAB (GHz)	Thickness (mm)	Filling ratio	References
Graphene/magnetic composites	$Co_{15}Fe_{85}$@C/RGO	9.2 GHz	2.5 mm	60 wt.%	[61]
	Fe–Co/NC/RGO	9.29 GHz	2.63 mm	25 wt.%	[67]
	$CoFe_2O_4$@PPy-RGO	13.12 GHz	3.6 mm	25 wt.%	[68]
	CI/RGO/PVP	13.8 GHz	2.5 mm	50 wt.%	[69]
	FeCo@graphite	13.4 GHz	2.5 mm	40 wt.%	[70]
	Ni@NG/NC	8.5 GHz	3 mm	20 wt.%	[71]
	FeCo@Cs	8.3 GHz	2.1 mm	50 wt.%	[72]
MXene/magnetic composites	$CoFe_2O_4$-Ti_3C_2	8.5 GHz	1.5 mm	40 vol.%	[78]
	FeCo-Ti_3C_2	8.8 GHz	1.6 mm	70 wt.%	[79]
	Ti_3C_2/FCI	8.16 GHz	1.0 mm	60 wt.%	[80]
	NiO&TiO_2@C	11.1 GHz	3.0 mm	33.3 wt.%	[81]
	Fe_3O_4@TiO_2	>15 GHz	2.0 mm	16.7 wt.%	[82]
	Fe_3O_4@TiO_2 yolk–shell	>14 GHz	2.0 mm	16.7 wt.%	[83]
	DS-Fe_3O_4@TiO_2-HNs	10.5 GHz	1.8 mm	20 wt.%	[84]
	Co_3O_4@TiO_2	~ 12.5 GHz	5.0 mm	30 wt.%	[85]
	Fe_3O_4/MWCNTs	11 GHz	3.0 mm	20 wt.%	[87]
	HCF@CZ-CNTs	8.02 GHz	2.0 mm	10 wt.%	[88]
	CoFe@C	9.2 GHz	2.8 mm	10 wt.%	[90]
	C/Co	9.0 GHz	2.9 mm	10 wt.%	[91]
	Ni-P coated T-ZnO	10.0 GHz	3.4 mm	90 wt.%	[93]
	Fe_3O_4@b-TiO_{2-x}	13 GHz	2.9 mm	75 wt.%	[97]
	CNT@$BaTiO_3$@PANI	10 GHz	4.0 mm	20 wt.%	[100]
Other dielectric/magnetic composites	NZCoF-CNT	10 GHz	1.0 mm	—	[103]
	Fe_3O_4-Coated CNTs	8.3 GHz	1.75 mm	30 wt.%	[104]
	MWCNTS-SDBS/Fe_3O_4	8 GHz	2.5 mm	25 wt.%	[105]
	FeNi-CNTs	11.3 GHz	3.5 mm	16.7 wt.%	[106]
	Fe_2O_3/Fe_3O_4/MWCNTs	8.80 GHz	2.4 mm	25 wt.%	[107]
	Fe_2O_3/Fe_3O_4/PANI/MWCNT	8.3 GHz	3.0 mm	25 wt.%	[108]
	FeCo@C-PCF	8.3 GHz	2.5 mm	30 wt.%	[109]
	C/$Co_{0.4}$	8.4 GHz	2.9 mm	20 wt.%	[111]
	LDH@C	9.0 GHz	3.35 mm	20 wt.%	[113]
	Co/NPC	9.4 GHz	3.2 mm	20 wt.%	[114]
	CC@ZnO	10.6 GHz	2.0 mm	40 wt.%	[117]
	Ni-doped ZnO	8.6 GHz	2.0 mm	70 wt.%	[120]
	ZnO/$CoFe_2O_4$	~ 9 GHz	1.5 mm	—	[122]
	CoFe/C	8.4 GHz	1.65 mm	60 wt.%	[127]

electrons to transform easily and increase the electrical conductivity [146]. Niu et al. found that the dielectric properties of Co-Ni-P nanoalloys could be significantly improved by introducing a suitable amount of 1D SiC nanowires [147]. Similarly, Si-C-N nanofibers could reach an EAB of 8.9 GHz at 3.0 mm due to the fact that the continuity and alignment of the Si-C-N nanofibers might form crosslinked networks with an enhanced conductive loss [148]. Yang et al. reported the fabrication of FeCo/ZnO nanofibers via electrospinning and a hydrogen reduction process. Within the 1D nanospace, the magnetic FeCo alloy and dielectric ZnO show a good synergistic effect. In addition, the 1D nanofibers form a three-dimensional (3D)-network hierarchical structure with distributed microcurrents and multiple reflections. The as-prepared FeCo/ZnO nanofibers exhibited outstanding MA performance with an effective absorption frequency ranging from 10.0 to 18 GHz at 1.3 mm [149].

For ferromagnetic materials, the elongated shape of 1D structures can provide an additional shape anisotropy to the magnetocrystalline anisotropy, which results in an increase in the effective anisotropy and the anisotropy field H_a [135]. According to the natural resonance equation $2\pi f_r = \gamma H_a$ (where γ is the gyromagnetic ratio) [150], a larger H_a will cause the natural resonance to shift toward a higher frequency, which is beneficial to the attenuation of microwaves at higher frequency. Usually, the natural ferromagnetic resonance of bulk Fe_3O_4 is around 1.2 GHz. He et al. found that Fe_3O_4 nanotubes have a higher f_r (4 GHz) than bulk Fe_3O_4 and other Fe_3O_4 nanostructures due to their large

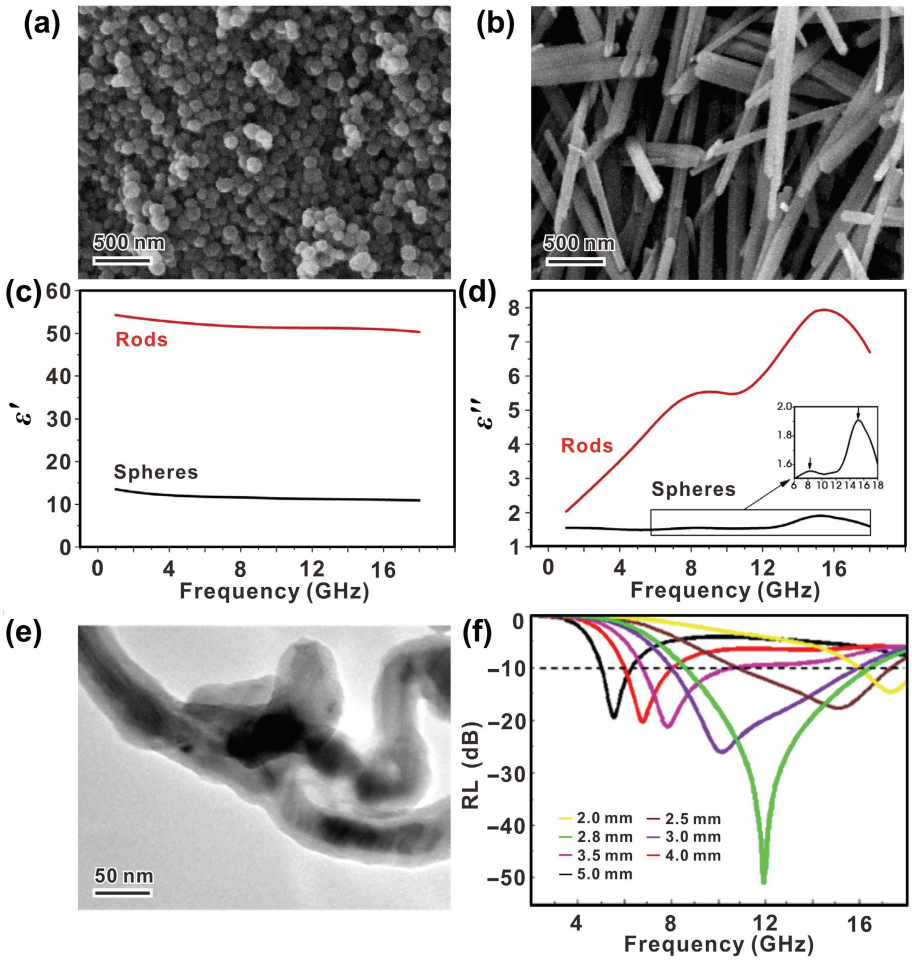

Figure 6 SEM images of (a) goethite spherical nanoparticles and (b) goethite nanorods. (c) and (d) the permittivity of the spherical nanoparticles and nanorods. Reproduced with permission from Ref. [135], © Elsevier B.V. 2015. (e) TEM image and (f) RL curves of SiC@C hybrid nanowires. Reproduced with permission from Ref. [144], © American Chemical Society 2017.

shape anisotropy, which leads to a higher magnetic loss and a better MA performance in the range of 2–18 GHz [151]. Among the series of $Co_{20}Ni_{80}$ alloys with different morphologies synthesized by Che's research group, chain-like particles showed the best MA performance; their optimal EAB could reach 13 GHz at 5 mm [130].

2.2.2 *Broadband MAMs with the 2D morphology*

For 2D materials, the increase in the aspect ratio, number of point defects, and number of interface dangling bonds leads to an enhancement of the dipole polarization, interface polarization, and space charge polarization, which improves the permittivity and loss ability of the materials [152–155]. Different from graphene, MXene, and other non-metallic 2D materials [156, 157], 2D magnetic metal materials for MAMs have unique characteristics and enhancement mechanisms [157].

Firstly, 2D magnetic materials with a large shape anisotropy are promising candidates for exceeding Snoek's limit in the GHz range and limiting the skin effect under the excitation of external electromagnetic fields [158–160]. Liu et al. demonstrated that when ball milling bulk FeCoNi Kovar alloy to flaked powders, the permeability increased significantly by increasing ball milling time [159]. The enhancement of the complex permeability can substantially enhance the properties of MAMs. Zhang et al. synthesized mesoporous hexagonal cobalt nanosheets through the reduction of $Co(OH)_2$ precursors. The nanosheets are beneficial for breaking Snoek's limit, giving rise to a considerable permeability in the high-frequency range. The mesoporous structure can decrease the permittivity and suppress the eddy current effect. The synergistic effect of the attenuation capability and the impedance matching yielded an EAB of 8.5 GHz [161].

Secondly, the 2D morphology can affect the natural resonance and exchange resonance of magnetic metal materials, and even result in multiple resonance peaks, which effectively enhance the attenuation of microwaves and broaden the EAB of the materials [162–164]. The natural resonance frequency depends on the effective anisotropy field [165, 166]. Flaky materials usually have a high in-plane anisotropy due to their low geometric symmetry, high aspect ratio, and small thickness [136]. An exchange resonance often results from the small size effect, surface effect, and spin wave excitation [167, 168]. Peng et al. demonstrated that an increasing number of flake-like particles could enhance the shape anisotropy field H_s and cause the natural resonance frequencies of the $(FeCo)_{100-x}Ni_x$ particles to shift toward higher frequencies. Additionally, the wide distribution of particle sizes and shapes induces multiple exchange resonances [169].

Thirdly, a proper stacking of the 2D materials may lead to a strong magnetic coupling and the formation of a significant magnetic network, which may enhance the MA performance [170]. You and Che synthesized NiO-Ni nanoplates by reducing $Ni(OH)_2$@polydopamine precursors. Due to the antiferromagnetism of NiO, the NiO-Ni nanoplates showed a strong micromagnetism. The strong external magnetic stray field and the magnetic coupling greatly enhanced the magnetic loss. The EAB of the NiO-Ni nanoplates could reach 10.2 GHz (Figs. 7(a) and 7(b)) [170]. They also constructed 1D/2D Fe composites by assembling Fe nanosheets along the axis orientation of the Fe chain [171]. The multidimensional composites exhibited the large

planar anisotropy of the Fe nanosheets in combination with the anisotropy field of the Fe chains, which endowed the composites with a strong anisotropy for magnetic response enhancement. The high-density magnetic flux lines resulting from the ultrathin magnetic nanosheets formed 3D coupling nets. The 3D network formed by iron-chain crosslinking could also improve the loss capacity. Therefore, the multidimensional Fe composites could achieve an EAB of 11.5 GHz at 1.9 mm.

Finally, the parallel-oriented structure formed by a 2D magnetic material under application of an external magnetic field can trigger a higher complex permeability, which can further improve the MA performances [172]. Zheng et al. designed a magnetorheological elastomer film by mixing Fe flakes into a silicone rubber matrix [173]. The Fe flakes in the matrix can be well rearranged under curing magnetic fields. Due to the oriented structure, the reinforced anisotropic permittivity/permeability of the composites could substantially improve the dielectric/magnetic loss. Furthermore, the discontinuous network perpendicular to the curing magnetic field could also improve the impedance matching. With a filler loading of 28 wt.%, the optimal EAB was 12.5 GHz at 5.0 mm (Figs. 7(c)–7(e)). Min et al. prepared oriented FCI/epoxy resin composites using a magnetic field to realize the parallel arrangement of FCI [174]. They demonstrated that the electromagnetic parameters could be optimized by tuning the FCI orientation, which improved the impedance matching and broadened the EAB of the composites. The widest EAB of these oriented samples was 12.5 GHz (5.5–18.0 GHz) at 1.4 mm.

2.2.3 Broadband hybrid structures with cavities for MAMs with broad-bandwidth response

Cavities are ubiquitous in all natural and engineered materials. Introducing cavities into material units is an effective strategy to optimize the impedance matching, which is crucial for expanding the EAB of MAMs. For example, the air (cavity) in CoNi@Air@TiO_2 microspheres ensures that most incident microwaves penetrate the magnetic cores without undergoing reflection; therefore, an EAB of around 8 GHz can be obtained [175]. On top of optimizing the impedance matching to improve the penetrability of incident waves, cavities also confer several interesting functionalities on MAMs. Firstly, the existence of cavities enhances the interface polarization and improves the charge density fluctuations between the medium and the cavity [176]. Li et al. fabricated yolk–shell-structured Co_3Fe_7@C composites by annealing $(Co_{0.9}Fe_{0.1})Fe_2O_4$@PR spheres. In addition to the complementary and synergistic features of the different components, the presence of cavities can increase the number of multiple interfaces among the amorphous carbon shells, Co_3Fe_7 cores, and cavities, which results in additional interfacial polarizations and improves the MA performance. The optimized Co_3Fe_7@C composite could achieve an EAB of 9.2 GHz (8.8–18.0 GHz) at 1.6 mm (Figs. 8(a)–8(c)) [177]. Liu et al. fabricated Fe/C hollow microspheres with a 3D interpenetrating network and multidomain structures using a solvothermal method and H_2/Ar gas reduction. This unique structure not only promoted the generation of abundant Fe/C interfaces for interfacial polarization relaxation but also endowed the composites with a high magnetic loss. The EAB of the optimal sample was 12.5 GHz at 2.5 mm [178]. Secondly, the empty regions and additional interfaces originated from the cavities caused an increase in the number of reflection and refraction interfaces for the microwaves in the materials, which is conducive to extending the transmission path of the microwaves in the material, thereby enhancing the microwave loss [179]. Zeng et al. prepared Fe_3O_4-embedded RGO hollow microspheres via a W/O emulsion technique and a calcination treatment [180]. Acting as a resonator, the hollow structure can trap the incident microwaves and improve the attenuation capacity of the material through multiple scattering behaviors. Thus, the widest EAB of the as-

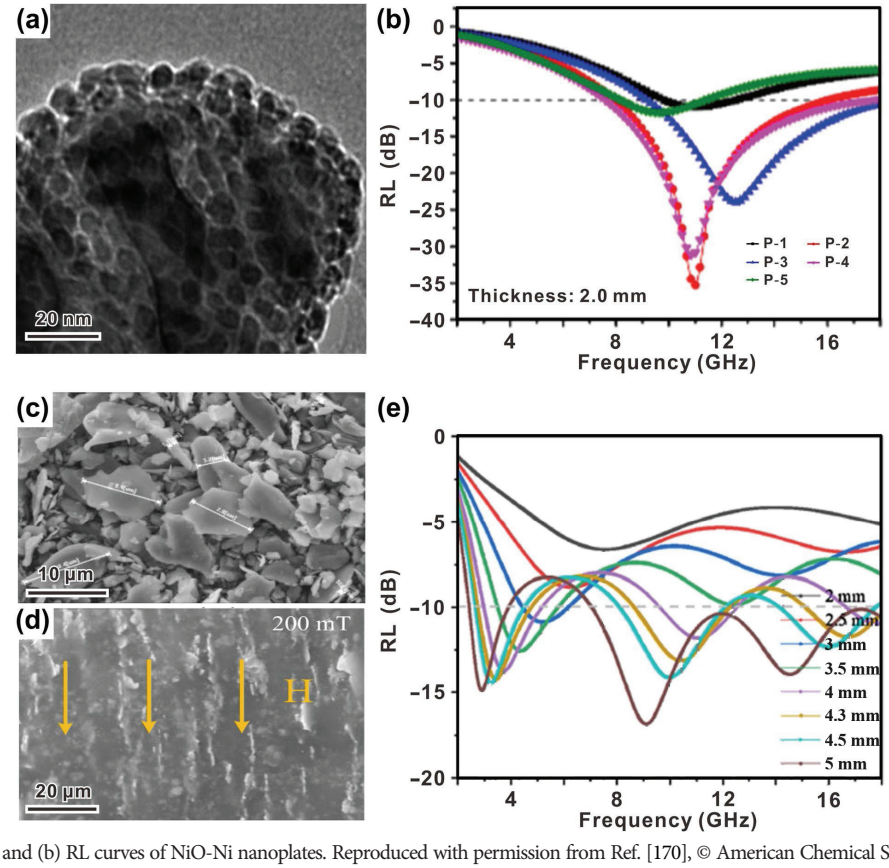

Figure 7 (a) TEM image and (b) RL curves of NiO-Ni nanoplates. Reproduced with permission from Ref. [170], © American Chemical Society 2018. (c) SEM image of flaky Fe particle, (d) SEM image, and (e) RL curves of F-Fe/MREF. Reproduced with permission from Ref. [173], © American Chemical Society 2020.

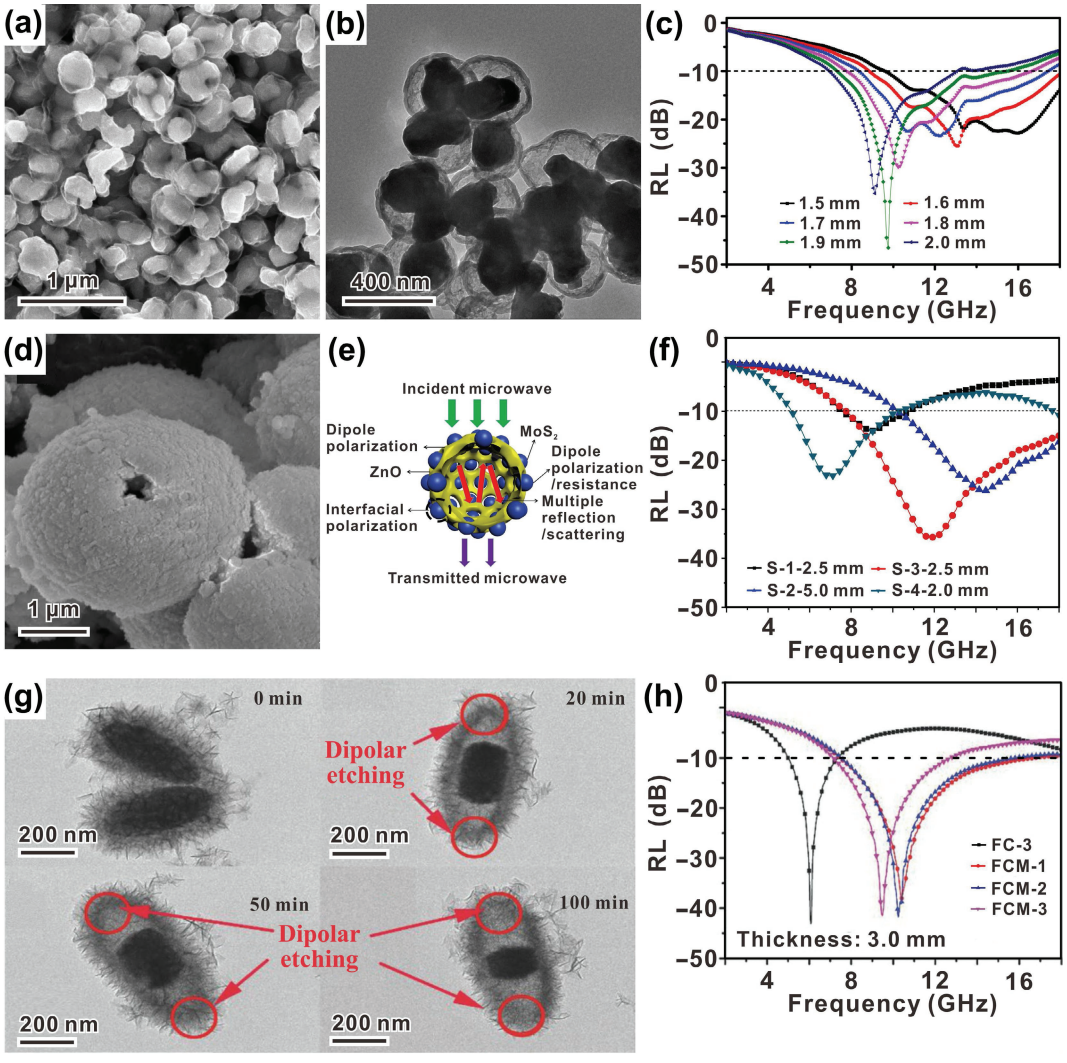

Figure 8 (a) SEM image, (b) TEM image, and (c) RL curves of Co_3Fe_7@C yolk–shell structures. Reproduced with permission from Ref. [177], © American Chemical Society 2018. (d) SEM image, (e) The MA mechanism schematic diagram, and (f) RL curves of ZnO/MoS_2 composites. Reproduced with permission from Ref. [92], © Elsevier B.V. 2019. (g) TEM images and (h) RL curves of γ-Fe_2O_3@C@α-MnO_2 nanospindles with different etching time. Reproduced with permission from Ref. [184], © Wiley-VCH Verlag GmbH & Co. KGaA, Weinheim 2016.

prepared hybrid microspheres was around 9 GHz at 3.5 mm.

Because of these clear advantages, researchers have extensively investigated the design of hybrid structures with voids and the selection of appropriate chemical components, and considerable progress has been achieved, especially regarding MAMs with a broad-bandwidth response. He et al. synthesized a series of Co_xNi_{1-x}-alloy hollow microspheres with tunable composition and shell thickness via a liquid-phase reduction method; the optimized sample could achieve an EAB of 10 GHz at 2.6 mm [181]. Cheng et al. demonstrated that Fe_3O_4@C hollow spheres could achieve an EAB of 8.0 GHz at 2.6 mm [182]. Liu et al. designed and constructed hierarchical hollow CuS@CoS_2 nanoboxes with double shells; their EAB could reach 8.2 GHz at 2.2 mm [183]. Luo et al. prepared ZnO/MoS_2 composites by decorating MoS_2 on hollow porous ZnO microspheres; the optimal EAB was 10.24 GHz at 2.5 mm (Figs. 8(d)–8(f)) [92].

To further optimize the MA performance, in addition to incorporating suitable chemical components and considering an appropriate morphology, a fine balance between the core, cavity, and shell should be maintained. Using γ-Fe_2O_3@C composites as precursors, You et al. synthesized a series of γ-Fe_2O_3@C@α-MnO_2 nanospindles with different cavity volumes by controlling the etching time (Figs. 8(g) and 8(h)) [184]. The dipolar cavity was beneficial for improving the impedance matching. The magnetic–dielectric synergism could be optimized by controlling the shell thickness and the cavity volume. An optimal EAB of 9.2 GHz could be achieved at 3.0 mm. Liu et al. prepared yolk–shell-structured Fe_3O_4@CuSilicate microspheres with an adjustable core size and shell thickness via a versatile sol–gel process and hydrothermal reaction [185]. The optimized structure with a 450-nm-diameter core and a 125-nm-thick shell could achieve an EAB of 10.4 GHz at 2.5 mm.

Thus, building a hybrid structure with cavities is an approach that can effectively optimize the impedance matching characteristics, enhance the polarization relaxation, and promote multiple scattering events. Combining the dielectric loss and/or magnetic loss of the core–shell components, an appropriate void structure can enhance the absorption capacity and expand the EAB of the MAMs. In addition, materials with cavities are lighter than solid materials, and are beneficial to the development of lightweight MAMs with a broad-bandwidth response.

Some typical cases of MAMs with broad-bandwidth response designed by morphological control strategy are summarized in Table 3.

2.3 Macrostructure control of MAMs with broad-bandwidth response

Through the rational selection of chemical components and a good morphology control, the intrinsic characteristics of MAMs can be tailored in order to adjust their electromagnetic parameters

Table 3 Typical cases of MAMs with broad-bandwidth response designed by morphological control strategy

Morphological control strategy	MAMs	Max EAB (GHz)	Thickness (mm)	Filling ratio (wt.%)	References
1D morphology	HCNFs coated-CFs	9.8 GHz	2.5 mm	15 wt.%	[142]
	SiC@C	8.0 GHz	2.8 mm	50 wt.%	[144]
	SdC@Fe/CBC	8.5 GHz	3.51 mm	5 wt.%	[145]
	Si-C-N	8.93 GHz	3.0 mm	10 wt.%	[148]
	FeCo/ZnO NFs	8.0 GHz	1.3 mm	50 wt.%	[149]
	$Co_{20}Ni_{80}$ chains	~ 13 GHz	5 mm	16.7 wt.%	[130]
2D morphology	Co	8.5 GHz	2.0 mm	70 wt.%	[161]
	NiO-Ni	11.2 GHz	2.0 mm	75 wt.%	[170]
	1D/2D Fe	11.5 GHz	1.9 mm	75 wt.%	[171]
	F-Fe/MREF	12.5 GHz	5.0 mm	28 wt.%	[173]
	FCI/EP	12.5 GHz	1.4 mm	75 wt.%	[174]
	ZnO/MoS_2	10.24 GHz	2.5 mm	30 wt.%	[92]
	$CoNi@Air@TiO_2$	8.1 GHz	2.1 mm	25 wt.%	[175]
	$Co_3Fe_7@C$	9.2 GHz	1.6 mm	65 wt.%	[177]
	Fe/C	12.5 GHz	2.5 mm	16.7 wt.%	[178]
Hybrid structure with cavities	Co_xNi_{1-x}	10.08 GHz	2.6 mm	50 wt.%	[181]
	Fe_3O_4 nanocrystals/MCHS	8.0 GHz	2.6 mm	20 wt.%	[182]
	$CuS@CoS_2$	8.2 GHz	2.2 mm	30 wt.%	[183]
	γ-Fe_2O_3@C@α-MnO_2	9.2 GHz	3.0 mm	16.7 wt.%	[184]
	Fe_3O_4@CuSilicate	10.4 GHz	2.5 mm	16.7 wt.%	[185]

and optimize their absorbing performance. To use these absorbing materials in practical application, the absorbing materials must be processed into an absorbing plate, absorbing coating, absorbing foam, or other structural parts. Therefore, it is very important to control the macrostructure of these components. Lightweight carbon foams (CFs) with a porous structure have attracted significant attention due to their very high specific surface area, diverse morphology, and chemical stability. Thanks to the large interfaces generated by the highly porous nature of the material, the attenuation capacity for incident electromagnetic waves can be significantly increased by enhancing the interface polarization and related relaxation loss. Single-layer absorbers that exhibit broadband absorption are rare [186]. Multilayered structures combine the MA properties of each layer at different frequencies, and the EAB can then be expanded by adjusting the thicknesses and properties of the different layers [187]. Recently, it has been found that electromagnetic metamaterials consisting of resistive element and dielectric substrates can overcome the limitations of the intrinsic properties of a single component. The design and use of metamaterials is expected to permit the realization of broadband absorption ranging from microwaves to visible light [188]. More importantly, the reflectivity of these large bulk materials in a given frequency range can be tested directly using the waveguide method or arch method without subsequent processing. In this section, broadband MAMs based on (1) porous foam structures, (2) multilayer structures, and (3) novel electromagnetic metamaterials are highlighted; their fabrication, underlying mechanisms, and MA performance are also discussed.

2.3.1 Porous-foam-structured MAMs with broad-bandwidth response

Besides the intrinsic properties of the building units, foam structures with a low density and a light weight display a broad bandwidth and tunable MA characteristics for many critical applications [189]. Firstly, there is large amount of air in the cell structures, and the overall impedance of the material is equivalent to that of air (377 Ω). The good impedance matching enables most of the incident microwaves to enter the interior of the material without being reflected from the surface. Secondly, the large specific surface area of foam structures can increase the number of multiple reflection events and trap the microwaves for continuous attenuation, which results in a large attenuation constant [190]. Simultaneously, the large specific surface area provides the material with a strong interfacial polarization, which can effectively enhance the polarization loss of the absorbing material [191]. Finally, the substrate units of the foam or honeycomb structure are interconnected. The energy transformed by the microwaves, such as the thermal energy, can be conducted rapidly, which can enhance the conduction loss of the absorbing material [192].

Numerous carbon foams with a 3D interconnected network have been developed based on graphene [193–195], CNTs [196], biomass materials [191, 197], ordered porous carbon [198], polymers [199–201], and so on. Especially, 3D GFs have shown great potential for achieving multiple absorption peaks and an excellent MA performance in an ultrawide spectral range from the GHz to the THz. The huge 3D intricate conductive network realized through the 2D graphene is the primary reason for the extraordinary MA properties of GFs [36]. Huang's research group obtained outstanding achievements in the preparation of graphene-based foams with an excellent performance. As early as 2015, they reported a macroscopic 3D free-standing GF with an excellent MA performance in a wide frequency range [202]. The EAB of the original GF could cover the frequency ranges of 4.1–18.0, 26.5–29.8, and 75–110 GHz for a sample with dimensions of 180 mm × 180 mm × 15 mm. The MA performance could be further improved upon application of a compressive strain. Especially, the total EAB of GF under 90% compressive strain was 60.5 GHz (6.0–18.0, 26.5–40.0, and 75–110 GHz) with a 1 mm thickness. They demonstrated that the MA performance of GF

depends strongly on the composition, conjugated carbon domain size, and microstructure of the graphene framework. Benefiting from the synergy between the good impedance matching and high loss characteristics, the optimal sample with a density of 1.6 mg/cm^3 achieved an EAB of 14.3 GHz (3.7–18 GHz) (Figs. 9(a)–9(c)). In order to expand the EAB to the low-GHz band, MWCNT/graphene hybrid foams (CGFs) were prepared by integrating 1D CNTs into a 3D GF [36]. The introduction of the MWCNTs could effectively improve the bulk electrical conductivity and polarization loss of GF by avoiding the stacking of the graphene sheets and strengthening the crosslinked network. The EAB of the optimized CGFs (CG7F-400) could cover the entire tested range of 2–18 GHz (Fig. 9(d)–9(f)).

Furthermore, foam structure has been demonstrated to possess excellent absorption properties in the THz frequency range (0.1–10 THz) [203]. For example, Chen et al. prepared 3D Fe_3O_4/graphene (3DFG) composites by combining Fe_3O_4 NPs with the highly porous graphene bulk material [204]. The huge number of multiinterfaces and defects generated by the introduction of the Fe_3O_4 NPs can considerably improve the interface polarization, resonance relaxation, and scatter response, which can effectively enhance the microwave loss capability of the composites. As a result, the macroscopic 3DFG exhibited strong MA performance across an extremely wide spectral range, from 3.4 GHz to 2.5 THz. Foam-structured MAMs can also maintain well-EAB in a wide temperature range. Yang et al. prepared a three-dimensional reticulated CI/CF composite. Resulting from the structural magnetic loss of magnetic components in 3D reticulated structure and well-defined conductive paths provided by the complete reticulated structure, the composite showed stable-wide EABs (8.32-8.48 GHz) in the temperature range of 298–573 K [205].

To further optimize the mechanical strength, bearing capacity, and process ability of carbon foams, the combination of carbon foams and polymer foams is a promising strategy to prepare multifunctional MAMs for practical applications. The complex relative permittivity of polymer foams can be easily tuned by filling them with different types or different contents of carbon materials [206]. Guo et al. fabricated CNT-filled polysiloxane foams and demonstrated that the complex relative permittivity and volume resistivity of the CNT/polysiloxane foams can be easily adjusted by filling them with different types and/or amounts of CNTs or applying different compression ratios [196]. The 3.5-mm-thick single-walled carbon nanotube (SWNT)/polysiloxane foam with 1.8 wt.% SWNTs and a compression ratio of 30% could achieve an EAB of > 9.5 GHz in a wide frequency range. Wu et al. prepared polypropylene (PP)/carbon black (CB) foams using subcritical CO_2 as a blowing

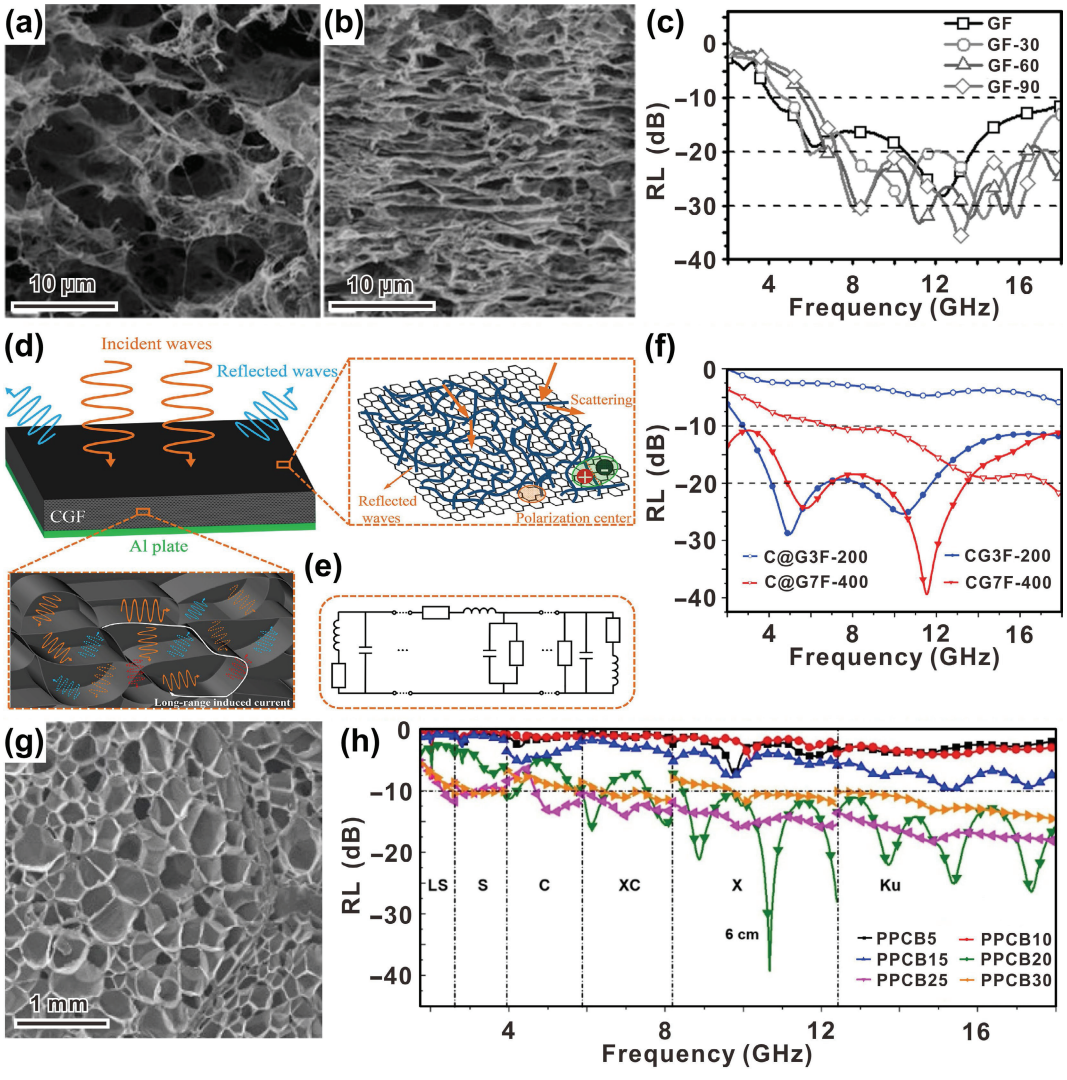

Figure 9 The SEM images of (a) GF and (b) GF under 90% compressive strain, (c) RL curves for the GFs under different compressive strains. Reproduced with permission from Ref. [202], © WILEY-VCH Verlag GmbH & Co. KGaA, Weinheim 2015. (d) Schematic diagram of microwave attenuation mechanism, (e) coupled circuits of 3D CGFs, and (f) RL values of C@GFs and CGFs. Reproduced with permission from Ref. [36], © Elsevier Ltd. 2017. (g) SEM image and (h) RL curves of PPCB composite foams. Reproduced with permission from Ref. [207], © Elsevier Ltd. 2020.

agent via a bath-foaming process [207]. They demonstrated that a certain amount of CB is required to construct effective networks for achieving a good dielectric loss, but an excessive amount of fillers deteriorates the impedance matching. The optimized 6-cm-thick foam containing 25 wt.% CB exhibited an EAB of 14.1 GHz over the 2.3–3.1 and 4.7–18 GHz ranges (Figs. 9(g) and 9(h)).

Besides carbon and polymers, several other materials, such as SiC, metals, and metal oxides, can be used as the substrates of foam-based MAMs. In addition to their light weight and broad-bandwidth response, these foams may show good fire resistance and high-temperature resistance, which is useful in extreme working conditions [208–211]. Li et al. prepared ceramic foams with a gradient SiC distribution and a high closed porosity by sintering a powder blend containing quartz, talc, $CaCO_3$, Si_3N_4, and SiC [209]. The gradient SiC distribution and high porosity improved considerably the impedance matching and energy attenuation capability of the materials. The mean reflectivity of the optimized sample was lower than −11.9 dB in the range from 8.0 to 18.0 GHz and remained almost unchanged after heating at 1000 °C for 20 h in air atmosphere. Qin et al. synthesized $NiFe_2O_4$/NiO/Ni foam using the leaven dough route [211]. The foam structure resulted in a good impedance matching and provided abundant pathways for the propagation of the incident microwaves. The interfacial polarization and defect-induced polarization provided by the NiO/$NiFe_2O_4$ structure endow the material with considerable microwave loss. As a result, the sample could achieve an EAB of 14.24 GHz at 0.6 mm.

2.3.2 Multilayer-structured microwave absorbers with broad-bandwidth response

Multilayer absorbers have strong design ability and low surface density, which can effectively improve the MA properties under the same thickness restrictions with single-layer absorbers [212, 213]. The design of multilayer MAMs can be divided into two types: the impedance gradient design and the impedance alternation design. Multilayer absorbing structures with a gradually changing impedance can improve the impedance matching characteristics between the material surface and air as well as between different layers, which are beneficial for the entry and absorption of incoming electromagnetic waves [214]. The impedance alternation structure refers to adding a lossless low dielectric constant layer between the loss layers with high dielectric constant and high permeability, and the multiple reflections and absorption between the layers help to widen the EAB. Liu et al. constructed a double-layer absorber composed of a CI-filled absorbing layer and a $CoFe_2O_4$-filled matching layer. They demonstrated that the MA performance of these double-layer absorbers is significantly better than that of single-layer absorbers. With a 2.4-mm-thick matching layer and a 0.5-mm-thick absorbing layer, the EAB of the double-layer absorber could achieve 9.4 GHz (8.6–18 GHz) [186]. Liu et al. designed a dual-layer absorber with an infiltrating activated carbon–paraffin matching layer and a Fe/C–paraffin absorbing layer. With a 3-mm-thick matching layer and a 1.5-mm-thick absorbing layer, the EAB of the dual-layer absorber could reach around 10 GHz [215]. Bai and collaborators reported on dual-layer absorbers composed of epoxy foam with different GO-CNT contents. The impedance layer consisted of an epoxy foam with 0.5 wt.% GO-CNTs, while the absorbing layer comprised an epoxy foam with 3.0 wt.% GO-CNTs. Compared with single-layer absorbers, the EAB of this dual-layer absorber was significantly improved to 11.5 GHz (6.5–18 GHz) using a 2.6-mm-thick impedance layer and a 1.3-mm-thick absorbing layer [216].

Using multiple impedance layers or absorption layers is expected to further broaden the response bandwidth and the input impedance of each layer can be easily adjusted by controlling the type and proportion of absorbent in each layer. Yang et al. proposed a type of sandwich absorber with strontium ferrite ($SrFe_{12}O_{19}$) microfibers as the outer layer, α-Fe microfibers as the interlayer, and NiZn ferrite ($Ni_{0.5}Zn_{0.5}Fe_2O_4$) microfibers as the inner layer. The small and similar values of the ε_r and μ_r of the ferrite hollow microfibers enabled microwaves to enter the adjacent layer, and the presence of the α-Fe interlayer resulted in a strong absorption accompanied by significant reflection. The optimal sandwich absorber composed of a 1.6-mm-thick outer layer, a 0.2-mm-thick interlayer, and a 0.2-mm-thick inner layer could achieve an EAB of 9.1 GHz (8.9–18 GHz) [217]. Furthermore, the gradient lamination of materials with matching frequencies at different frequencies is conducive to achieving broadband strong absorption of the total absorber under thin layer conditions. Choi et al. reported a triple-layered absorber containing a thin resistive layer (MWCNT-filled cotton fabric/epoxy resin) sandwiched between two different dielectric absorbing layers (MWCNT-filled E-glass fiber/epoxy resin layers with different MWCNT concentrations) [218]. The different dielectric properties of each absorption layer could lead to double resonance absorption peaks. Additionally, the EAB of the total absorber could be significantly improved by controlling the sheet resistance of the resistive layer and the permittivity of the absorbing layers. Thus, the EAB of the optimized triple-layered absorber could reach 9.0 GHz (4.7–13.7 GHz). Wang et al. prepared a CI composite/amorphous alloy slice/CI composite sandwich structure. The thin amorphous alloy slice inserted between the two CI layers led to double absorption peaks, which could dramatically broaden the EAB to 11.7 GHz (Figs. 10(a) and 10(b)) [219]. Ling et al. prepared a multilayer absorber containing a CI/polyurethane (PU) matching layer (layer 1), a MWCNT/PU filtering layer (layer 2), and a $Ce_2Fe_{17}N_{3-\delta}$/PU absorbing layer (layer 3). The microwave selective filtering effect resulted in the appearance of double absorption peaks. With a total thickness of 2.3 mm, the EAB of the optimized multilayer absorber reached 12.6 GHz (5.4–18 GHz) (Figs. 10(c) and 10(d)) [187]. In addition to the chemical composition and thickness of each layer, in some cases, the overlap angle between the layers may also affect the MA properties of the multilayer absorbing structures [220], which may provide new opportunities to further optimize the performance of multilayer microwave absorbers.

2.3.3 Metamaterial-based microwave absorbers with broad-bandwidth response

Electromagnetic metamaterials are artificial structures composed of periodically arranged resonant units with supernormal physical properties that natural materials do not possess [213, 221]. It has been proved that metamaterials can achieve zero-reflection at a specific frequency, and they can break through the limitation of the influence of wavelength on absorption capacity in a certain frequency range under a given thickness, and are expected to expand the bandwidth to L band and S band, so as to achieve wider absorption response [31]. Microwave absorbers based on metamaterials can be mainly divided into three categories, namely monolayer metamaterial absorbers, multilayer metamaterial absorbers, and traditional/metamaterial composite absorbers. The frequency-selective surface (FSS) consisting of 2D periodic structures with a planar metallic array can also be attributed to monolayer metamaterial absorbers [222, 223]. The emergence of metamaterials affords new theories and strategies for the design and development of novel microwave absorbers. Changing the material composition, shape, cell size, array period, and other structural parameters of the metamaterials can effectively control the transmission and reflection characteristics of incident

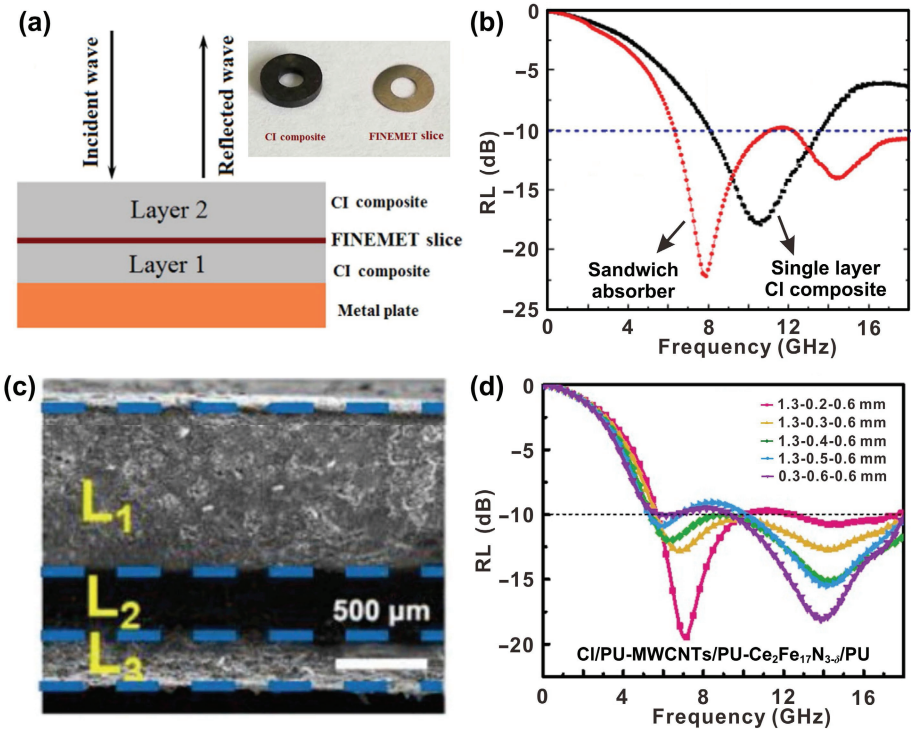

Figure 10 (a) The structure of sandwich absorber and (b) RL curves of single layer CI composite and sandwich absorber. Reproduced with permission from Ref. [219], © Elsevier Ltd. 2016. (c) SEM image of the cross section of multilayer absorbing structure and (d) RL curves of the absorbers with different L_1, L_2, and L_3 thicknesses. Reproduced with permission from Ref. [187], © Elsevier Ltd. 2019.

microwaves [224].

The rational design of metamaterial absorbers can achieve "perfect" absorption at certain resonant frequencies and provide an opportunity to broaden the EAB of the currently available MAMs [225]. The resonant units combining thin absorption layers can effectively suppress the average reflectivity and result in a strong absorption at different frequencies, which should ultimately help in achieving broadband absorption. Hannan et al. proposed a low-profile and application-targeted microwave metamaterial absorber with polarization and angle insensitivity by engineering the filling factor of the resonator of a hybrid FSS. The absorber can be applied in multiple scenarios by adjusting the resonance frequencies [226]. Zhang et al. demonstrated that metamaterial absorbers containing windmill-shaped elements display three absorption bands [227]. The optimal absorptivity was greater than 90% in the range of 8.3–17.4 GHz. Pang et al. designed a metamaterial absorber using water as the dielectric substrate [228]. The MA characteristics of this metamaterial absorber varied with the change in the environment temperature. The metamaterial absorber with optimized geometry parameters achieved an absorption efficiency exceeding 90% in the range from 4 to 20 GHz. Qu et al. designed a metamaterial absorber with hierarchical structures by introducing metallic ring structural dipole resonances and realized an averaged reflection loss of −19.4 dB in the range of 3–40 GHz [40].

Compared with monolayer metamaterial absorbers, multilayer metamaterial absorbers have more potential in broadening the EAB of microwave absorbers [229–232]. By combining the transfer-matrix method and the adaptive genetic algorithm, Li et al. designed a series of microwave absorbers containing a resistive FSS [233]. By inserting a layer of resistive FSS, the 5.0-mm-thick microwave absorber could achieve an EAB of 11.8 GHz. When the thickness of the absorption layer was increased to 10 mm, the EAB could be further extended to 12.9 GHz. Based on an improved genetic algorithm, Zhang et al. proposed a precise and comprehensive optimization method to design broadband absorbing structures [234]. They also fabricated several absorbing sandwich structures containing fiber-reinforced epoxy face sheets, polyvinyl chloride (PVC) foam, and double FSS films with square patterns of various periods. The FSS films separated by the PVC foam were considered as the main microwave absorbing components, and the EAB was proportional to the pattern period. The EAB of the optimized absorber was 15 GHz (2–17 GHz). Shen et al. proposed a plasmonic absorbing structure containing meandered/straight wire arrays. The excitation of these meandered wire arrays made the adjacent resonances close to each other, so the previously isolated absorption bands could be merged into a whole band. Simulations and experimental measurements demonstrated that this hybrid plasmonic absorbing structure could achieve an EAB of 26.6 GHz (5.0–31.6 GHz) [235].

The combination of microscopic and mesoscopic scale effects can cause multiscale effects; the metamaterial design of a multilayer topological gradient structure can introduce more abundant electromagnetic response [236]; the development of a multiscale structural absorber combined with traditional MAMs and metastructures may aid in the achievement of an efficient broadband MA [237, 238]. Lossy materials (such as CI, α-Fe, RGO, and CNTs) are responsible for the dissipation of the incident microwave energy through magnetic and/or dielectric losses, while the metastructure helps to broaden the working bandwidth by optimizing the impedance matching and manipulating the electromagnetic field [239, 240]. By manipulating the content of lossy materials or changing the geometry parameters of the macrostructures, the electromagnetic parameters of the composites can be effectively controlled to achieve superior impedance matching and wide-band absorption [241]. For instance, Zhou et al. reported a double-layer periodic microwave absorber, which was engraved by an α-Fe-reinforced epoxy resin using a numerically controlled lathe [237]. Compared with the flat structure, the impedance matching of the double-layer periodic absorber was optimized in a wide frequency range. Due to the synergy of the good impedance matching and the strong edge diffraction effects, the optimized absorber showed an

ultrabroadband absorption in the range from 2.64 to 40.0 GHz (Figs. 11(a) and 11(b)). Huang et al. prepared a series of CI/MWCNT/epoxy resin composites with different components [240]. The permittivity and permeability could be controlled by adjusting the contents of the MWCNTs and CI as well as the macrostructure; the composites with the best geometrical parameters achieved an EAB of 30 GHz. The broad-bandwidth response is attributed to the synergism of the energy dissipation due to the nano/micro design of the lossy composites, the impedance matching, and the field concentration due to the macro geometrical design. Compared with traditional manufacturing methods, the 3D printing technology has clear advantages in the manufacturing of complex MA structures [242–244]. Duan et al. fabricated a complex gradient composite microwave absorbing metastructure using the 3D printing technology; the microstructure was composed of flaky CI particles and a polyether ether ketone composite [242]. The as-prepared metastructure showed a wide EAB from 5.1 to 40 GHz but also possessed good compression strength and mechanical stability. Wang et al. used 3D printer to print a male resin mold with the designed periodical structure, and used the mixture of hollow carbon/MXene/Mo_2C (HCMM) powder and silica gel as the filler of the female mold. Such 3D metamaterial models based on the HCMM with EAB in 3.7–40.0 GHz were fabricated via a multi-scale design method [245].

The combination of metal-pattern metamaterials and traditional MAMs is another effective way to expand the EAB of microwave absorbers. Planar metal-pattern metamaterials on the top layer of microwave absorbers can reduce the overall reflectivity and improve the impedance matching, which helps to achieve broadband absorption [239]. Inserting planar metastructures into traditional microwave absorbers can induce the occurrence of electric and magnetic resonances, which can optimize the absorption characteristics of MAMs [246]. Li et al. constructed a four-layer microwave absorber. From the first to the fourth layer, this absorber was composed of an FR4 dielectric material, SiC/C foam, a combination of a periodic-array metal pattern and an FR4 dielectric material, and SiC/C foam, respectively [210]. The FR4 layer was used for mechanical support and microwave transmission; furthermore, it served as the impedance matching layer. The metal pattern contributed to frequency-resonance. The SiC/C foam rendered the structure lightweight and provided MA capabilities. Through the adjustment of the geometric parameters of the patterns (such as the side length, array period, line width, and split width), a high-efficiency absorption at certain frequencies could be realized. The optimized multilayer microwave absorber modeled through simulations and investigated via experiments could achieve a wide EAB of 14 GHz (4–18 GHz). In addition to the planar metal pattern, traditional absorbers can also be combined with metamaterials with a non-planar metal pattern. In this hybrid absorbing structure, the top non-planar metamaterial layer absorbs strongly low-frequency microwaves and allows high-frequency microwaves to pass through without reflection. The bottom layer of traditional absorbing materials absorbs strongly high-frequency microwaves. Li et al. designed a double-layer absorber with a non-planar metamaterial and flaky CI particles to increase the absorption [247]. The hybrid absorber could achieve 90% absorptivity over the whole range of 2–18 GHz. Shen et al. proposed a hybrid metamaterial absorber consisting of a plasmonic structure covering, a resistive FSS, a

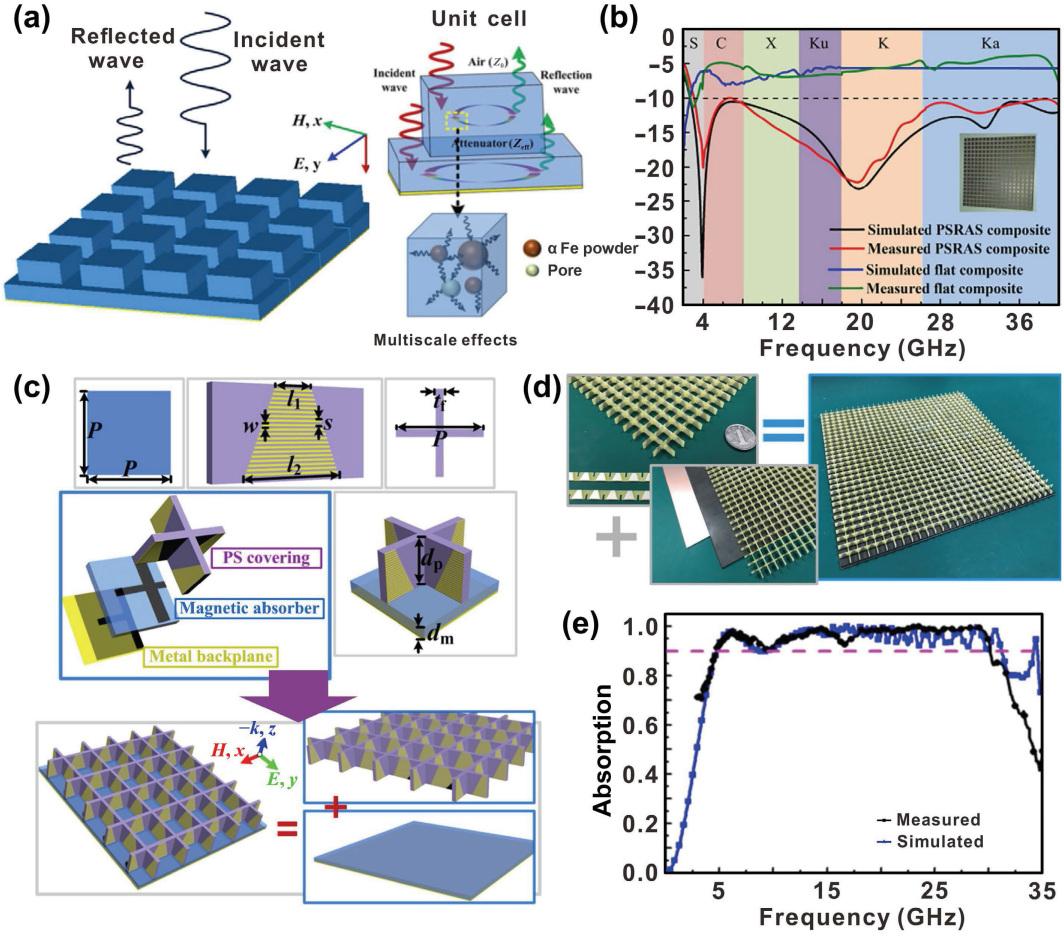

Figure 11 (a) Schematic diagram of the periodic stepped radar absorbing structure (PSRAS) and (b) RL curves of the composites. Reproduced with permission from Ref. [237], © Elsevier Ltd. 2017. (c) Schematic diagram of plasmonic metamaterial absorbers, (d) Fabricated sample, and (e) the absorption spectra of the hybrid metamaterial absorbers. Reproduced with permission from Ref. [248], © Shen, Y. et al. 2018.

polymethacrylimide foam spacer, and a metal backplane [248]. The plasmonic structure covering, which was based on a straight wire array, could enhance the *k*-vector matching absorption in a wider frequency band. These hybrid metamaterial absorbers could achieve an EAB of 30.9 GHz (4.1–35.0 GHz) under normal incidence (Figs. 11(c) and 11(d)).

Some typical cases of MAMs with broad-bandwidth response designed by macrostructure control strategy are summarized in Tables 4 and 5.

3 Conclusions and outlook

With the rapid development of modern electronics and the widespread use of microwave radiation in everyday life, high-performance MAMs with a broad-bandwidth response have received increased attention. Generally, the performance of MAMs is highly dependent on the impedance matching and attenuation constant, and the latter is affected by processes such as dielectric loss, magnetic loss, and conduction loss. On top of the intrinsic characteristics of the materials used for absorbing structures, impedance matching can be controlled by constructing hybrid structures, porous structures, multilayer structures, and metamaterials. The attenuation constant can also be tailored by carefully selecting the chemical components, morphology, and microstructure/macrostructure of the materials used. Through careful design, it is expected that high-performance MAMs with a broad bandwidth and strong absorption, that are lightweight and require only a small thickness, can be constructed. This review outlines the recent progress in the design and construction of high-performance MAMs with a broad-bandwidth response. The main strategies for expanding EAB of MAMs are comprehensively summarized from three aspects: chemical combination strategy, morphological control strategy, and macrostructure control strategy. Several important design principles have been highlighted: (1) The material systems with multiple chemical components, especially those combining dielectric loss materials and magnetic loss materials, can not only optimize the characteristic impedance matching in a broad frequency range but also effectively avoid the aggregation of magnetic particles and lead to a synergy between the magnetic loss and dielectric loss of the system; such combinations of materials can be used to improve the absorption capacity and broaden the response bandwidth of the system. (2) The interconnection of 1D or 2D units gives materials more heterogeneous interfaces, which can effectively improve the dielectric polarization and dissipation capacity of the system. 1D or 2D magnetic materials can lead to a high anisotropy and a strong magnetic coupling interaction, which decrease the original permeation threshold, increase the cut-off frequency, and enhance the magnetic loss capacity of the system. To make full use of the advantages of 1D and/or 2D materials, constructing 3D interconnected networks composed of 1D or 2D materials is helpful to transfer heat and electrons, improve the attenuation behavior of the system, and broaden the EAB of the resultant materials. (3) The careful design and construction of special structures including void regions or the inclusion of air, such as yolk–shell structures, hollow structures, and foam structures, can be used to effectively balance the electromagnetic parameters and optimize the impedance matching of the materials in order to broaden the EAB of the composites. The existence of void regions will increase the proportion of heterogeneous interfaces and lead to strong dipolar/interfacial polarizations, which can further improve the MA properties of the material. (4) The rational design and construction of multilayer structures can be used to improve the impedance matching as well as provide multiple resonance peaks at different frequencies; this can significantly broaden the EAB of the microwave absorbers. (5) Metamaterials provide new possibilities to design microwave absorbers with a broad-bandwidth response. Controlling the properties of metamaterials can effectively control the transmission and reflection characteristics of incident microwaves. The rational design of metamaterial absorbers can lead to a good impedance matching over a wider frequency band, and combining the resonant units with lossy materials can effectively decrease the average reflectivity and produce strong absorption at several

Table 4 Typical cases of MAMs with broad-bandwidth response designed by macrostructure control strategy

Macrostructure control strategy	Foam-structure MAMs	EAB	Thickness (mm)	References
Porous-foam-structured MAMs	MWCNT/graphene	16 GHz	10 mm	[36]
	Fish skin-derived 3D carbon	8.6 GHz	3.0 mm	[191]
	SWNT/polysiloxane	>9.5 GHz	3.5 mm	[196]
	Graphene	~ 13 GHz	10 mm	[202]
	3D graphene	0.1–1.2 THz	1 mm	[203]
	Fe_3O_4/graphene	3.4 GHz–2.5 THz	10 mm	[204]
	CNT/graphene/PI	8.5 GHz	3.3 mm	[206]
	Polypropylene/carbon black	14.1 GHz	60 mm	[207]
	Ceramic	10 GHz	11 mm	[209]
	$NiO/NiFe_2O_4/Ni$	14.24 GHz	0.6 mm	[211]
	CI/CF	8.48 GHz	1.0 mm	[205]
Multilayer-structured microwave absorbers	$(CoFe_2O_4)$/(carbonyl iron)	9.4 GHz	2.4 mm/0.5 mm	[186]
	(CI)/(MWCNTs)/$(Ce_2Fe_{17}N_{3-\delta})$	12.6 GHz	1.3 mm/0.4 mm/0.6 mm	[187]
	(Activated carbon)/(Fe/C)	~ 10 GHz	3 mm/1.5 mm	[215]
	(GO-CNTs)/(epoxy foam)	11.5 GHz	2.6 mm/1.3 mm	[216]
	$(SrFe_{12}O_{19})/(Ni_{0.5}Zn_{0.5}Fe_2O_4)$/(α-Fe)	9.1 GHz	1.6 mm/0.2 mm/0.2 mm	[217]
	(0.15 wt.% MWNT-filled E-glass fiber)/(6.6 wt.% MWNT-filled cotton fabric)/(0.5 wt.% MWNT-filled E-glass fiber)	9 GHz	3 mm/0.5 mm/2.5 mm	[218]
	(CI composite)/(thin amorphous alloy slice)/(CI composite)	11.7 GHz	0.5 mm/20 μm/1.6 mm	[219]

Table 5 Typical cases of metamaterial-based microwave absorbers with broad-bandwidth response

Unit cell	Substrate	Effective absorption range	Thickness	References
Square	FCI/epoxy resin	4–40 GHz	3.7 mm	[222]
Windmill-shaped elements	Indium tin oxide + polymethyl methacrylate + polyethylene glycol terephthalate	8.3–17.4 GHz	3.85 mm	[227]
Square copper patch array	Water + low-permittivity material	6.2–19 GHz	3.5 mm	[228]
Square	Flake ferrous microwave absorbent + polyurethane foam	3.19–18 GHz	5.0 mm	[229]
Square loop + interdigitated Jerusalem cross element	Foam spacer	~ 6–22 GHz	~ 5 mm	[232]
Square	Glass-fiber + polyvinyl chloride foam + carbon-fiber	2–17 GHz	17.4 mm	[234]
Meandered-wire-shaped	Dielectric substrate	5.0–31.6 GHz	10.0 mm	[235]
Two-layer PSRAS	α Fe reinforced epoxy resin	2.64–40.0 GHz	5.5 mm	[237]
Square-shaped	PMI foam + graphene films	1–18 and 26.5–40 GHz	26.0 mm	[238]
Cube	RGO/PP	2–40 and 75–110 GHz	15 mm	[239]
Protuberant blocks	MWCNT/CI/epoxy resin	2–2.36, 6.54–19.36, 19.89–21.57, and 25.1–40 GHz	45 mm	[240]
Central gradient cubes and four surrounding gradient cubes	FCI/polyether-ether-ketone	5.1–40 GHz	10.0 mm	[242]
Cross-helix array	Si–O–C ceramic	8.65–18.00 GHz	8.0 mm	[244]
Split ring resonators	FR-4 substrate	4.5–18 GHz	30 mm	[247]
Straight wire array	FR-4 substrate	4.1–35.0 GHz	8.0 mm	[248]
Multilayer gradient superstructure	S3PC	5.3–18 GHz	5.0 mm	[236]
Multi-scale square	Hollow carbon/MXene/Mo_2C	3.7–40.0 GHz	5.0 mm	[245]

resonant points. The use of a combination of metamaterials and traditional MAMs may provide another approach to broaden the EAB of the absorber materials.

Although considerable progress has been achieved in the design and construction of MAMs with a broad-bandwidth response, a number of challenges still remain in the characterization as well as in the understanding of the absorption mechanism and dynamics of MAMs: (1) In general, the electromagnetic properties and MA properties of lab-scale samples are measured via the transmission line method using a vector network analyzer (VNA). The measured permittivity and permeability can be affected by many factors such as the thickness of the tested sample consisting of paraffin and absorbent, and the content and orientation of absorbent [249, 250]. Thus, the obtained results only reflect the characteristics of the whole coaxial ring "device" (although we note that paraffin is transparent to microwave radiation) instead of the intrinsic properties of MAMs. The relationship between the actual permittivity and the absorbent content in the composite can be described by the percolation theory: $\varepsilon_r' \propto |f_{c,vol} - f_{vol}|^{-t}$, where $f_{c,vol}$ is the percolation threshold, f_{vol} is the absorbent content, and t is the dielectric critical exponent [251, 252]. The percolation threshold represents the critical filling content of absorbent when the composite is transformed from insulator to conductor. That is, there exists the best absorbent content in the paraffin/absorbent composite to ensure an adequate conductivity and good impedance matching, so as to achieve the best MA performance. In some cases, the increase of absorbent content can greatly reduce the matching thickness and adjust the strong absorption frequency range. In addition, as the thickness of the absorbing material increases, the RL peaks will move to low frequencies, and the MA performances in the high frequency range will deteriorate accordingly [32, 33]. For these reasons, the calculated MA properties of similar materials reported by different research groups can be seen to vary considerably, which makes it difficult to establish the relationship between the composition, structure, and performance of MAMs. Thus, more reliable measurement and theoretical investigation require further exploration. (2) The loss mechanisms of MA primarily include dielectric loss, magnetic loss, and conduction loss. Defect engineering, heterointerface engineering, and polarization strategies have been proposed to enhance the performance of MAMs [253–255]. The development of off-axis electron holography and Lorentz transmission electron microscopy (TEM) has provided insights into the intrinsic micromagnetic properties of magnetic metal-based composites; such measurements help to reveal the magnetic loss mechanism within MAMs [256]. Some scholars have effectively combined microscopic origin with macroscopic rules to explain and predict microwave absorption behavior [257]. However, the absorption mechanisms and dynamics of MAMs are still far from being completely understood. Furthermore, it is difficult to quantify the influence of the crystal structure, particle size, morphology, defect, grain boundaries, interface, porosity, magnetic domains, and random crystal orientation on the MA properties of a material. This lack of quantification has significantly impeded the design and development of high-efficiency MAMs with a broad-bandwidth response. In order to accurately predict and control the MA performance of a material, it is necessary to develop more advanced technologies for the *in situ* measurement of the electronic and magnetic domain structure of MAMs; such measurements may reveal the dynamic response that dictates the response to microwave radiation of a material. Artificial intelligence, big data, and machine learning may play an important role in addressing this shortcoming. (3) Numerical simulations have been widely used in the design and analysis of bulk MAMs. However, for the nanostructured materials, such methods are not readily applicable. The wavelength of microwave radiation is in the range of 1–1000 mm, whereas the structure unit of a nanostructured material is primarily on the nanometer scale. Thus, there is a difference of several orders of magnitude in the eigenvalues of the system, and thus, it is difficult to obtain numerical solutions using traditional simulation techniques [72]. The development of applicable numerical models and feasible simulation strategies is expected to elucidate the actual absorption mechanism and dynamics of the processes that occur in

nanostructured MAMs. Furthermore, the absorption mechanism and dynamic response of MAMs are extremely complex, and a variety of absorption mechanisms and dynamic processes may simultaneously coexist in a given microwave absorber. The quantification of the influence of various factors on the performance of microwave absorbers via simulation and the design of new MAMs based on this understanding are expected to be of great importance in this field.

In order to satisfy the requirements of MAMs for use in practical applications, further research into the following areas is necessary. (1) Improvement of magnetic permeability in GHz ranges. For MAMs, the impedance matching is an important prerequisite for achieving excellent MA performance. At present, the real part and imaginary part of the complex permittivity of dielectric loss materials can reach a wide range, but the complex permeability of magnetic materials is limited in small ranges, making it difficult to achieve impedance matching. In addition, the imaginary part of complex permeability often decreases with the increase of frequency due to the Snoek's limit. Therefore, improving the permeability in GHz range is very important to enhance the MA performance. So far, some measures have been found to improve the permeability, such as compounding, nano-materialization, and modifying shape anisotropy. However, the structure of the material is associated with many parameters (such as M_s, K_1, and internal strain (ξ)) that can affect the permeability. A certain operation will cause multiple parameters to change at the same time, which brings difficulties to studies. There is still a lack of corresponding theories to guide the improvement of permeability. (2) Magnetic metamaterials. Electromagnetic waves in the low-GHz frequency range, such as the L band, S band, and C band, are more difficult to be attenuated by absorbers due to their long wavelengths [258–260]. Recent years, researchers have made many beneficial attempts to develop MAMs with low-GHz absorption, such as $FeCoNiMn_{0.5}Al_{0.2}$ high entropy alloys [261], FeCoNi carbon fiber [140], and Fe_3O_4@polypyrrole [262]. Unfortunately, traditional MAMs based on magnetic or dielectric materials usually have problems such as thick thickness, high density, and narrow EAB in low-GHz due to the limitation of their inherent properties. Although metamaterials have been found to show better MA performances in low-GHz, their pure dielectric properties usually result in excessive thickness. Constructing magnetic metamaterials with both magnetic coatings and high dielectric substrates to improve the effective permeability of the absorber is conducive to improving the impedance matching at low-GHz, which can further reduce the effective absorption thickness and enlarge the EAB [263]. (3) Utilization of data-driven methods. At present, the small-scale synthesis of MAMs in the laboratory is difficult to meet the requirements of industrial production. A systematic analysis method that can guide the large-scale fabrication of MAMs and predict the MA properties of materials is still missing. The data-driven method combines numerical methods and machine learning, enabling scientists to obtain the optimal formula of MAMs through analysis automation, mathematical modeling, and material simulation [264]. This method can not only reduce the development cost and production time of known MAMs, but also promote the exploration of new MAMs [265, 266]. Therefore, it is a valuable research direction of using data-driven method to guide the manufacture and production of MAMs. (4) Flexible microwave absorbers. Flexible microwave absorbers can be used to directly cover the complex shape of the target, and such materials can be designed into wearable multifunctional stealth combat and protective clothing; such developments are of great significance in both military and civilian fields [253–269]. For example, Cao's group [24], Ji's group [263, 269], and others have made progress in this field. However, the development of flexible microwave absorbers with a broad-bandwidth response is still in its infancy; considerable work is still required in the material design and preparation methods related to flexible microwave absorbers. (5) Intelligent microwave absorbers. With the rapid development of dynamic and multisource electromagnetic equipment operating at a range of frequencies, intelligent microwave absorbers with frequency tuning, adjustable structure, and excellent performance are of particular importance [270]. The design and realization of absorbing materials with a dynamic adaptive structure and with structures that respond to a given stimulus will help the development of novel technologies and present new opportunities for the construction of microwave absorbers with a broad-bandwidth response. (6) Multifunctional MAMs. With the increasing complexity of electromagnetic environment, robust MAMs should be developed to meet the needs of military applications and harsh environmental conditions. However, different functions may have conflicting requirements for the application of MAMs, such as EMI shielding–MA and infrared (IR) stealth–MA, which adds difficulty to the development of multifunctional MAMs. For structural absorbing materials, the mechanical properties and bearing capacity of the material must also be considered. In order to ensure that these materials can be used when they are subject to high temperature, high humidity, and salt spray, it is imperative to develop multifunctional MAMs with a broad-bandwidth response.

4 Appendix: basic concepts of MAMs

4.1 The *S* parameter

Scattering parameters (*S* parameters) are used to describe the frequency domain characteristics of the transmission channel; their values are typically a complex number [271]. When tested using the coaxial method, the VNA has two ports. The values S_{12} (port 2 to port 1) and S_{21} (port 1 to port 2) represent the transmission characteristics between the two ports. The *S* parameters, given in dB, can be converted to magnitude using Eq. (1); the frequency (*f*)-dependent absorption rate can be calculated using Eq. (2) [272]

$$20\log_{10}|S| = S\,(\mathrm{dB}) \tag{1}$$

$$A(f) = 1 - R(f) - T(f) = 1 - |S_{11}|^2 - |S_{21}|^2 \tag{2}$$

where S_{11} (dB) is the reflection coefficient, S_{21} (dB) is the transmission coefficient, and *A*, *R*, and *T* represent the absorption rate, reflection rate, and transmission rate, respectively [273].

4.2 Electromagnetic parameters

4.2.1 Relative complex permittivity

The permittivity represents the polarizing capacity of a dielectric material in an applied electric field. The relative complex permittivity (ε_r) can be expressed as: $\varepsilon_r = \varepsilon' - j\varepsilon''$, where ε' represents the capacity of electric energy storage from the external electric field, and ε'' represents the loss capability of the electric field energy. ε' and ε'' can be expressed as a function of the response of the dielectric constants at low frequencies (ε_s) and high frequencies (ε_∞), the relaxation time constant (τ), and the frequency (*f*), as given in Eqs. (3) and (4) [274]

$$\varepsilon' = \varepsilon_\infty + \frac{\varepsilon_s - \varepsilon_\infty}{1 + f^2\tau^2} \tag{3}$$

$$\varepsilon'' = \varepsilon_\infty + \frac{(\varepsilon_s - \varepsilon_\infty)\omega\tau}{1+f^2\tau^2} \quad (4)$$

4.2.2 Relative complex permeability

The permeability indicates the ability of a material to obtain internal magnetization under an applied magnetic field. The relative permeability (μ_r) is given by the absolute permeability (μ) divided by the vacuum permeability (μ_0); the relative permeability can be expressed as: $\mu_r = \mu' - j\mu''$, where μ' and μ'' are defined in Eqs. (5) and (6), respectively. μ' represents the capacity of the material for magnetic energy storage, and μ'' represents the loss capability of the material for magnetic energy based on the existing relaxation mechanisms.

$$\mu' = \frac{B_m}{\mu_0 H_m}\cos\theta \quad (5)$$

$$\mu'' = \frac{B_m}{\mu_0 H_m}\sin\theta \quad (6)$$

where B_m and H_m are the amplitudes of the induced and applied magnetic fields, respectively, and θ is the phase angle which B lags behind H.

4.3 Loss mechanisms in MAMs

4.3.1 Dielectric loss

Dielectric loss refers to the process in which a dielectric converts electrical energy into thermal energy and other energy under the action of an external electric field. Dielectric loss is generally divided into relaxation polarization loss, conductivity loss, and resonance loss [275]:

(1) The relaxation polarization loss is due to the time required to establish dipole polarization or space-charge polarization. When the frequency of the external electric field is increased, the changes in dipole polarization cannot occur at the same rate as the change in the electric field; this results in polarization relaxation. The polarization of the medium thus lags behind the electric field, which consumes a proportion of the energy and induces the dielectric loss.

(2) The conduction loss is due to the directional drift of conductive carriers under the action of electric field, which forms a conduction current in the medium, and this part of the conduction current is consumed in the form of heat. The magnitude of the conduction current is determined by the nature of the dielectric itself.

(3) Resonance loss originates from the resonance effect of atoms, ions, and electrons when they vibrate or rotate. The phase velocity of the propagation of an electromagnetic wave in a medium and the refractive index of that medium depend on the frequency of the electromagnetic wave, and the refractive index induces a dispersion phenomenon with the change in frequency; this results in energy loss and absorption. The dispersion of the resonant polarization of electrons or atoms (ions) in the optical frequency range is considered to be a resonant dispersion, whereas the dispersion of the relaxation polarization due to dipole steering in the electrical frequency range is referred to as relaxation dispersion.

4.3.2 Magnetic loss

The conversion of magnetic energy into heat due to magnetic interactions between the magnetic components of a material and incident electromagnetic waves is referred to as magnetic loss. Generally, eddy current loss and resonance loss are the primary sources of magnetic loss in the range of 2–18 GHz; this is because the hysteresis loss is negligible under a weak electromagnetic field.

(1) Eddy current loss refers to the dissipation of magnetic energy by the induced currents that are generated inside a conductor within a changing magnetic field. If eddy current loss is the only magnetic loss mechanism, the values of the eddy current effect C_0 ($C_0 = \mu''(\mu')^{-2}f^{-1}$) will be constant under frequency variations.

(2) Resonance loss primarily includes natural resonance and exchange resonance. Natural resonance occurs when the characteristic frequency of the target material matches the cut-off frequency of the incident electromagnetic wave. Restricted by Snoek's limit, the natural resonance frequency and the initial permeability cannot be increased simultaneously (see Eqs. (7) and (8)). According to Eqs. (9) and (10), the natural resonance frequency can be effectively increased by enhancing the anisotropy field [276]. The exchange resonance induces energy loss via the oscillatory motion of the electron spins; this effect often occurs at higher frequencies than those at which natural resonance occurs [277, 278].

$$(\mu_i - 1)f_r^n = \frac{2\gamma M_s}{3\pi} \quad (7)$$

$$f_r^n = \frac{\gamma H_a}{2\pi} \quad (8)$$

$$H_a = 4|K|/3\mu_0 M_s \quad (9)$$

$$K = \mu_0 M_s H_c/2 \quad (10)$$

where μ_i, γ, f_r^n, M_s, and H_a are the initial permeability, spin-magnetic ratio, cut-off frequency, saturation magnetization, and anisotropy field, respectively. K represents the crystal anisotropy constant, and H_c represents the coercivity of the material.

4.3.3 Impedance matching characteristics

There are three processes that occur after an electromagnetic wave is incident on the surface of a material: reflection, absorption, and transmission. To realize effective attenuation, it is necessary for electromagnetic waves to enter the material to as large an extent as possible. The impedance matching coefficient (Z) is usually used to characterize the extent to which an electromagnetic wave enters the absorber; this quantity is expressed in Eq. (11)

$$Z = \frac{Z_{in}}{Z_0} = \sqrt{\frac{\mu_r}{\varepsilon_r}}\tanh\left(j\frac{2\pi fd}{c}\sqrt{\mu_r\varepsilon_r}\right) \quad (11)$$

where Z_0 is the impedance of free space, Z_{in} is the input impedance of the absorber, c is the velocity of light, and d is the thickness of the absorber. According to the impedance matching condition, the impedance is completely matched when Z_0 is equal to Z_{in}, and in this condition, all electromagnetic waves can enter the material. The smaller the proportion of electromagnetic waves that are reflected from the surface of an absorbing material, the more electromagnetic waves are able to enter the material. The reflective properties of the material surface on microwave radiation can be described using the reflection coefficient (Γ); a smaller value of Γ means a stronger absorbing capacity [279].

$$\Gamma = \frac{\sqrt{\frac{\mu_r}{\varepsilon_r}} - 1}{\sqrt{\frac{\mu_r}{\varepsilon_r}} + 1} \quad (12)$$

4.3.4 Attenuation constant

The attenuation constant represents the power attenuation of the

electromagnetic wave in the transmission process; this parameter indicates the extent to which a material attenuates microwave radiation. The value of this parameter can be obtained using Eq. (13)

$$\alpha = \frac{\sqrt{2}\pi f}{c}\sqrt{(\mu''\varepsilon'' - \mu'\varepsilon') + \sqrt{(\mu''\varepsilon'' - \mu'\varepsilon')^2 + (\mu'\varepsilon'' + \mu''\varepsilon')^2}} \quad (13)$$

4.4 Testing methods for evaluating the MA performance

There are both direct and indirect methods to measure the MA properties of materials. Direct measurement method refers to the method of directly measuring the reflectance of a material or calculating the reflectance from the measured data via approaches such as the arch method and radar cross section measurements. The indirect measurement method refers to measurements of the impedance or electromagnetic parameters of the material; these values are then used to calculate the reflectivity of the material; indirect methods include the coaxial method and the waveguide method. The coaxial method is more widely used in relevant research articles due to its small sample demand and simple test, and is taken as an example to introduce the indirect measurement method.

4.4.1 Arch method

The arch method is primarily used to measure the reflectivity of flat MAMs based on the plane wave reflection principle. The test system is composed of a bow device, a signal source, a network analyzer, background absorbing material, and other equipment. The sample of appropriate size is placed at the center of the bow frame to obtain approximate plane wave irradiation. The electromagnetic waves emitted by the transmitting antenna are reflected off the sample and accepted by the receiving antenna, while the other electromagnetic waves are absorbed by the background absorbing material. The two ports of the vector network analyzer are connected to the transmitting and receiving antennas respectively for reflectivity measurement. After measuring the reflected power in the mirror direction obtained from the tested sample and a good conductor with the same size, the RL of the absorbing material can be obtained via the expression RL (dB) = 10lg(P_a/P_m), where P_a is the reflected power of the plate made of the absorbing material, and P_m is the reflected power of the metal plate that is a good conductor of the same size. A large sample size or a short bow radius will cause the phase distribution of the electromagnetic wave irradiated on the sample to be different from the plane wave distribution. In order to reduce the influence of edge diffraction, the edge length of the square sample is generally required to be greater than three times the electromagnetic wavelength. The edge length can be selected according to the different test frequency range, for example, 50 cm for 1–8 GHz, 30 cm for 2–18 GHz, and 18 cm for 6–40 GHz.

4.4.2 Coaxial method

The values of ε_r and μ_r of the absorbing material can be calculated using the reflection and transmission coefficients of the tested sample; this measurement can be undertaken using the coaxial method based on the transmission line theory. The main device used in this method is APC–7 mm circular coaxial line, which is a guided system composed of two coaxial cylindrical conductors to propagate TEM (transverse electromagnetic) wave. When TEM wave propagates in the coaxial line, the direction of its propagation is perpendicular to the section of the coaxial line, which means the electromagnetic wave is vertically incident on the surface of the sample. In addition, because the annular tube of the coaxial line is made of metal materials of high conductivity, the reflectance of absorbing materials can be measured without interference from external electromagnetic waves under laboratory conditions. The test toroidal sample with an outer diameter of 7.0 mm, inner diameter of 3.0 mm, and thickness d is filled between the inner and outer conductors of the circular coaxial line with a material of impedance Z_0. The electromagnetic wave will be reflected and transmitted multiple times in the absorber, leading to a phase shift and energy attenuation. The measured S parameters can be converted into electromagnetic parameters by using data processing software, and then the reflective loss of materials can be calculated based on the transmission line theory, as described in the following expression

$$\mathrm{RL\,(dB)} = 20\lg\left|\frac{Z_{in} - Z_0}{Z_{in} + Z_0}\right| \quad (14)$$

Acknowledgements

This work was supported by the National Natural Science Foundation of China (Nos. 21771151 and 21931009).

References

[1] Che, R. C.; Peng, L. M.; Duan, X. F.; Chen, Q.; Liang, X. L. Microwave absorption enhancement and complex permittivity and permeability of Fe encapsulated within carbon nanotubes. *Adv. Mater.* **2004**, *16*, 401–405.

[2] Zhang, Y.; Huang, Y.; Chen, H. H.; Huang, Z. Y.; Yang, Y.; Xiao, P. S.; Zhou, Y.; Chen, Y. S. Composition and structure control of ultralight graphene foam for high-performance microwave absorption. *Carbon* **2016**, *105*, 438–447.

[3] Wu, Z. C.; Cheng, H. W.; Jin, C.; Yang, B. T.; Xu, C. Y.; Pei, K.; Zhang, H. B.; Yang, Z. Q.; Che, R. C. Dimensional design and core–shell engineering of nanomaterials for electromagnetic wave absorption. *Adv. Mater.* **2022**, *34*, 2107538.

[4] Liang, L. L.; Gu, W. H.; Wu, Y.; Zhang, B. S.; Wang, G. H.; Yang, Y.; Ji, G. B. Heterointerface engineering in electromagnetic absorbers: New insights and opportunities. *Adv. Mater.* **2022**, *34*, 2106195.

[5] Watts, C. M.; Liu, X. L.; Padilla, W. J. Metamaterial electromagnetic wave absorbers. *Adv. Mater.* **2012**, *24*, OP98–OP120.

[6] Li, Q.; Zhang, Z.; Qi, L. P.; Liao, Q. L.; Kang, Z.; Zhang, Y. Toward the application of high frequency electromagnetic wave absorption by carbon nanostructures. *Adv. Sci.* **2019**, *6*, 1801057.

[7] Li, Y.; Liu, X. F.; Nie, X. Y.; Yang, W. W.; Wang, Y. D.; Yu, R. H.; Shui, J. L. Multifunctional organic–inorganic hybrid aerogel for self-cleaning, heat-insulating, and highly efficient microwave absorbing material. *Adv. Funct. Mater.* **2019**, *29*, 1807624.

[8] Shu, J. C.; Cao, W. Q.; Cao, M. S. Diverse metal-organic framework architectures for electromagnetic absorbers and shielding. *Adv. Funct. Mater.* **2021**, *31*, 2100470.

[9] Tao, J. Q.; Xu, L. L.; Jin, H. S.; Gu, Y. S.; Zhou, J. T.; Yao, Z. J.; Tao, X. W.; Chen, P.; Wang, D. H.; Li, Z. et al. Selective coding dielectric genes based on proton tailoring to improve microwave absorption of MOFs. *Adv. Powder Mater.* **2023**, *2*, 100091.

[10] Tirkey, M. M.; Gupta, N. The quest for perfect electromagnetic absorber: A review. *Int. J. Microw. Wireless Technol.* **2019**, *11*, 151–167.

[11] Cao, M. S.; Shu, J. C.; Wen, B.; Wang, X. X.; Cao, W. Q. Genetic dielectric genes inside 2D carbon-based materials with tunable electromagnetic function at elevated temperature. *Small Struct.* **2021**, *2*, 2100104.

[12] Song, Q.; Ye, F.; Kong, L.; Shen, Q. L.; Han, L. Y.; Feng, L.; Yu, G. J.; Pan, Y. A.; Li, H. J. Graphene and MXene nanomaterials: Toward high-performance electromagnetic wave absorption in gigahertz band range. *Adv. Funct. Mater.* **2020**, *30*, 2000475.

[13] Cao, M. S.; Wang, X. X.; Zhang, M.; Shu, J. C.; Cao, W. Q.; Yang,

H. J.; Fang, X. Y.; Yuan, J. Electromagnetic response and energy conversion for functions and devices in low-dimensional materials. *Adv. Funct. Mater.* **2019**, *29*, 1807398.

[14] Qiao, M. T.; Lei, X. F.; Ma, Y.; Tian, L. D.; He, X. W.; Su, K. H.; Zhang, Q. Y. Application of yolk–shell Fe_3O_4@N-doped carbon nanochains as highly effective microwave-absorption material. *Nano Res.* **2018**, *11*, 1500–1519.

[15] Quan, B.; Shi, W. H.; Ong, S. J. H.; Lu, X. C.; Wang, P. L.; Ji, G. B.; Guo, Y. F.; Zheng, L. R.; Xu, Z. J. Defect engineering in two common types of dielectric materials for electromagnetic absorption applications. *Adv. Funct. Mater.* **2019**, *29*, 1901236.

[16] Xiao, J. X.; Qi, X. S.; Gong, X.; Peng, Q.; Chen, Y. L.; Xie, R.; Zhong, W. Defect and interface engineering in core@shell structure hollow carbon@MoS_2 nanocomposites for boosted microwave absorption performance. *Nano Res.* **2022**, *15*, 7778–7787.

[17] Zhi, D. D.; Li, T.; Li, J. Z.; Ren, H. S.; Meng, F. B. A review of three-dimensional graphene-based aerogels: Synthesis, structure and application for microwave absorption. *Compos. Part B: Eng.* **2021**, *211*, 108642.

[18] Ren, S. N.; Yu, H. J.; Wang, L.; Huang, Z. K.; Lin, T. F.; Huang, Y. D.; Yang, J.; Hong, Y. C.; Liu, J. Y. State of the art and prospects in metal-organic framework-derived microwave absorption materials. *Nano-Micro Lett.* **2022**, *14*, 68.

[19] Guan, H. T.; Wang, Q. Y.; Wu, X. F.; Pang, J.; Jiang, Z. Y.; Chen, G.; Dong, C. J.; Wang, L. H.; Gong, C. H. Biomass derived porous carbon (BPC) and their composites as lightweight and efficient microwave absorption materials. *Compos. Part B: Eng.* **2021**, *207*, 108562.

[20] Bhattacharjee, Y.; Bose, S. Core–shell nanomaterials for microwave absorption and electromagnetic interference shielding: A review. *ACS Appl. Nano Mater.* **2021**, *4*, 949–972.

[21] Wang, G. H.; Ong, S. J. H.; Zhao, Y.; Xu, Z. J.; Ji, G. B. Integrated multifunctional macrostructures for electromagnetic wave absorption and shielding. *J. Mater. Chem. A* **2020**, *8*, 24368–24387.

[22] Yan, J.; Huang, Y.; Liu, X. D.; Zhao, X. X.; Li, T. H.; Zhao, Y.; Liu, P. B. Polypyrrole-based composite materials for electromagnetic wave absorption. *Polym. Rev.* **2021**, *61*, 646–687.

[23] Tao, J. Q.; Tan, R. Y.; Xu, L. L.; Zhou, J. T.; Yao, Z. J.; Lei, Y. M.; Chen, P.; Li, Z.; Ou, J. Z. Ion-exchange strategy for metal-organic frameworks-derived composites with tunable hollow porous and microwave absorption. *Small Methods* **2022**, *6*, 2200429.

[24] Zhang, M.; Cao, M. S.; Shu, J. C.; Cao, W. Q.; Li, L.; Yuan, J. Electromagnetic absorber converting radiation for multifunction. *Mater. Sci. Eng.: R: Rep.* **2021**, *145*, 100627.

[25] Green, M.; Tian, L. H.; Xiang, P.; Murowchick, J.; Tan, X. Y.; Chen, X. B. FeP nanoparticles: A new material for microwave absorption. *Mater. Chem. Front.* **2018**, *2*, 1119–1125.

[26] Rozanov, K. N.; Starostenko, S. N. Numerical study of bandwidth of radar absorbers. *Eur. Phys. J. Appl. Phys.* **1999**, *8*, 147–151.

[27] Rozanov, K. N. Ultimate thickness to bandwidth ratio of radar absorbers. *IEEE Trans. Antennas Propag.* **2000**, *48*, 1230–1234.

[28] Kuzhir, P.; Celzard, A.; Chen, X. B. Microwave absorption by carbon-based materials and structures. *J. Appl. Phys.* **2022**, *131*, 200401.

[29] Choudhary, A.; Pal, S.; Sarkhel, G. Broadband millimeter-wave absorbers: A review. *Int. J. Microw. Wireless Technol.*, in press, https://doi.org/10.1017/S1759078722000162.

[30] Tretyakov, S. Thin absorbers: Operational principles and various realizations. *IEEE Electromagn. Compat. Mag.* **2016**, *5*, 61–66.

[31] Ra'di, Y.; Simovski, C. R.; Tretyakov, S. A. Thin perfect absorbers for electromagnetic waves: Theory, design, and realizations. *Phys. Rev. Appl.* **2015**, *3*, 037001.

[32] Green, M.; Li, Y.; Peng, Z. H.; Chen, X. B. Dielectric, magnetic, and microwave absorption properties of polyoxometalate-based materials. *J. Magn. Magn. Mater.* **2020**, *497*, 165974.

[33] Green, M.; Xiang, P.; Liu, Z. Q.; Murowchick, J.; Tan, X. Y.; Huang, F. Q.; Chen, X. B. Microwave absorption of aluminum/hydrogen treated titanium dioxide nanoparticles. *J. Materiomics* **2019**, *5*, 133–146.

[34] Huang, M. Q.; Wang, L.; You, W. B.; Che, R. C. Single zinc atoms anchored on MOF-derived N-doped carbon shell cooperated with magnetic core as an ultrawideband microwave absorber. *Small* **2021**, *17*, 2101416.

[35] Sun, G. B.; Dong, B. X.; Cao, M. H.; Wei, B. Q.; Hu, C. W. Hierarchical dendrite-like magnetic materials of Fe_3O_4, γ-Fe_2O_3, and Fe with high performance of microwave absorption. *Chem. Mater.* **2011**, *23*, 1587–1593.

[36] Chen, H. H.; Huang, Z. Y.; Huang, Y.; Zhang, Y.; Ge, Z.; Qin, B.; Liu, Z. F.; Shi, Q.; Xiao, P. S.; Yang, Y. et al. Synergistically assembled MWCNT/graphene foam with highly efficient microwave absorption in both C and X bands. *Carbon* **2017**, *124*, 506–514.

[37] Yao, X.; Huang, Y. Q.; Li, G. Y.; He, Q. T.; Chen, H. Y.; Weng, X. L.; Liang, D. F.; Xie, J. L.; Deng, L. J. Design of an ultra-broadband microwave metamaterial absorber based on multilayer structures. *Int. J. RF Microw. Comput. Aid. Eng.* **2022**, *32*, e23222.

[38] Lin, H. R.; Green, M.; Xu, L. J.; Chen, X. B.; Ma, B. W. Microwave absorption of organic metal halide nanotubes. *Adv. Mater. Interfaces* **2020**, *7*, 1901270.

[39] Green, M.; Chen, X. B. Recent progress of nanomaterials for microwave absorption. *J. Materiomics* **2019**, *5*, 503–541.

[40] Qu, S. C.; Hou, Y. X.; Sheng, P. Conceptual-based design of an ultrabroadband microwave metamaterial absorber. *Proc. Natl. Acad. Sci. USA* **2021**, *118*, e2110490118.

[41] Wang, J. Y.; Xi, R.; Cai, T.; Lu, H.; Zhu, R. R.; Zheng, B.; Chen, H. S. Deep neural network with data cropping algorithm for absorptive frequency-selective transmission metasurface. *Adv. Opt. Mater.* **2022**, *10*, 2200178.

[42] Wang, W.; Guo, J. X.; Long, C.; Li, W.; Guan, J. G. Flaky carbonyl iron particles with both small grain size and low internal strain for broadband microwave absorption. *J. Alloys Compd.* **2015**, *637*, 106–111.

[43] Tong, G. X.; Wu, W. H.; Hua, Q.; Miao, Y. Q.; Guan, J. G.; Qian, H. S. Enhanced electromagnetic characteristics of carbon nanotubes/carbonyl iron powders complex absorbers in 2–18 GHz ranges. *J. Alloys Compd.* **2011**, *509*, 451–456.

[44] Zeng, X. J.; Cheng, X. Y.; Yu, R. H.; Stucky, G. D. Electromagnetic microwave absorption theory and recent achievements in microwave absorbers. *Carbon* **2020**, *168*, 606–623.

[45] Green, M.; Tian, L. H.; Xiang, P.; Murowchick, J.; Tan, X. Y.; Chen, X. B. Co_2P nanoparticles for microwave absorption. *Mater. Today Nano* **2018**, *1*, 1–7.

[46] Wang, L.; Li, X.; Shi, X. F.; Huang, M. Q.; Li, X. H.; Zeng, Q. W.; Che, R. C. Recent progress of microwave absorption microspheres by magnetic–dielectric synergy. *Nanoscale* **2021**, *13*, 2136–2156.

[47] Green, M.; Liu, Z. Q.; Xiang, P.; Liu, Y.; Zhou, M. J.; Tan, X. Y.; Huang, F. Q.; Liu, L.; Chen, X. B. Doped, conductive SiO_2 nanoparticles for large microwave absorption. *Light: Sci. Appl.* **2018**, *7*, 87.

[48] Green, M.; Liu, Z.; Smedley, R.; Nawaz, H.; Li, X.; Huang, F.; Chen, X. Graphitic carbon nitride nanosheets for microwave absorption. *Mater. Today Phys.* **2018**, *5*, 78–86.

[49] Li, H.; Cao, Z. M.; Lin, J. Y.; Zhao, H.; Jiang, Q. R.; Jiang, Z. Y.; Liao, H. G.; Kuang, Q.; Xie, Z. X. Synthesis of u-channelled spherical $Fe_x(Co_yNi_{1-y})_{100-x}$ Janus colloidal particles with excellent electromagnetic wave absorption performance. *Nanoscale* **2018**, *10*, 1930–1938.

[50] Darvishzadeh, A.; Nasouri, K. Broadband and tunable high-performance microwave absorption properties by Ni-coated carbon fibers. *Mater. Chem. Phys.* **2021**, *274*, 125127.

[51] Cao, M. S.; Han, C.; Wang, X. X.; Zhang, M.; Zhang, Y. L.; Shu, J. C.; Yang, H. J.; Fang, X. Y.; Yuan, J. Graphene nanohybrids: Excellent electromagnetic properties for the absorbing and shielding of electromagnetic waves. *J. Mater. Chem. C* **2018**, *6*, 4586–4602.

[52] Chen, C.; Xi, J. B.; Zhou, E. Z.; Peng, L.; Chen, Z. C.; Gao, C. Porous graphene microflowers for high-performance microwave absorption. *Nano-Micro Lett.* **2018**, *10*, 26.

[53] Meng, F. B.; Wang, H. G.; Huang, F.; Guo, Y. F.; Wang, Z. Y.;

Hui, D.; Zhou, Z. W. Graphene-based microwave absorbing composites: A review and prospective. *Compos. Part B: Eng.* **2018**, *137*, 260–277.

[54] Li, J. S.; Huang, H.; Zhou, Y. J.; Zhang, C. Y.; Li, Z. T. Research progress of graphene-based microwave absorbing materials in the last decade. *J. Mater. Res.* **2017**, *32*, 1213–1230.

[55] Chen, H. H.; Ma, W. L.; Huang, Z. Y.; Zhang, Y.; Huang, Y.; Chen, Y. S. Graphene-based materials toward microwave and terahertz absorbing stealth technologies. *Adv. Opt. Mater.* **2019**, *7*, 1801318.

[56] Zhang, M. M.; Zhang, J. W.; Lv, X. Y.; Zhang, L.; Wei, Y.; Liu, S. C.; Shi, Y. P.; Gong, C. H. How to exhibit the efficient electromagnetic wave absorbing performance of RGO aerogels: Less might be better. *J. Mater. Sci.: Mater. Electron.* **2018**, *29*, 5496–5500.

[57] Sun, G. B.; Wu, H.; Liao, Q. L.; Zhang, Y. Enhanced microwave absorption performance of highly dispersed CoNi nanostructures arrayed on graphene. *Nano Res.* **2018**, *11*, 2689–2704.

[58] Zhang, Y. L.; Wang, X. X.; Cao, M. S. Confinedly implanted $NiFe_2O_4$-rGO: Cluster tailoring and highly tunable electromagnetic properties for selective-frequency microwave absorption. *Nano Res.* **2018**, *11*, 1426–1436.

[59] Lv, H. L.; Guo, Y. H.; Yang, Z. H.; Cheng, Y.; Wang, L. P.; Zhang, B. S.; Zhao, Y.; Xu, Z. J.; Ji, G. B. A brief introduction to the fabrication and synthesis of graphene based composites for the realization of electromagnetic absorbing materials. *J. Mater. Chem. C* **2017**, *5*, 491–512.

[60] Wang, T. S.; Liu, Z. H.; Lu, M. M.; Wen, B.; Ouyang, Q. Y.; Chen, Y. J.; Zhu, C. L.; Gao, P.; Li, C. Y.; Cao, M. S. et al. Graphene-Fe_3O_4 nanohybrids: Synthesis and excellent electromagnetic absorption properties. *J. Appl. Phys.* **2013**, *113*, 024314.

[61] Bao, S. S.; Tang, W.; Song, Z. J.; Jiang, Q. R.; Jiang, Z. Y.; Xie, Z. X. Synthesis of sandwich-like $Co_{15}Fe_{85}$@C/RGO multicomponent composites with tunable electromagnetic parameters and microwave absorption performance. *Nanoscale* **2020**, *12*, 18790–18799.

[62] Zhang, H. X.; Jia, Z. R.; Feng, A. L.; Zhou, Z. H.; Chen, L.; Zhang, C. H.; Liu, X. H.; Wu, G. L. *In situ* deposition of pitaya-like Fe_3O_4@C magnetic microspheres on reduced graphene oxide nanosheets for electromagnetic wave absorber. *Compos. Part B: Eng* **2020**, *199*, 108261.

[63] Zhang, X. J.; Wang, G. S.; Cao, W. Q.; Wei, Y. Z.; Liang, J. F.; Guo, L.; Cao, M. S. Enhanced microwave absorption property of reduced graphene oxide (RGO)-$MnFe_2O_4$ nanocomposites and polyvinylidene fluoride. *ACS Appl. Mater. Interfaces* **2014**, *6*, 7471–7478.

[64] Hu, Q.; Qi, X. S.; Cai, H. B.; Xie, R.; Long, L.; Bai, Z. C.; Jiang, Y.; Qin, S. J.; Zhong, W.; Du, Y. W. Preparation of porous Fe_2O_3 nanorods-reduced graphene oxide nanohybrids and their excellent microwave absorption properties. *Sci. Rep.* **2017**, *7*, 11213.

[65] Zhu, Z. T.; Sun, X.; Xue, H. R.; Guo, H.; Fan, X. L.; Pan, X. C.; He, J. P. Graphene-carbonyl iron cross-linked composites with excellent electromagnetic wave absorption properties. *J. Mater. Chem. C* **2014**, *2*, 6582–6591.

[66] Quan, B.; Liang, X. H.; Ji, G. B.; Lv, J.; Dai, S. S.; Xu, G. Y.; Du, Y. W. Laminated graphene oxide-supported high-efficiency microwave absorber fabricated by an *in situ* growth approach. *Carbon* **2018**, *129*, 310–320.

[67] Wang, S. S.; Xu, Y. C.; Fu, R. R.; Zhu, H. H.; Jiao, Q. Z.; Feng, T. Y.; Feng, C. H.; Shi, D. X.; Li, H. S.; Zhao, Y. Rational construction of hierarchically porous Fe-Co/N-doped carbon/rGO composites for broadband microwave absorption. *Nano-Micro Lett.* **2019**, *11*, 76.

[68] Ding, L.; Zhao, X. X.; Huang, Y.; Yan, J.; Li, T. H.; Liu, P. B. Ultra-broadband and covalently linked core–shell $CoFe_2O_4$@PPy nanoparticles with reduced graphene oxide for microwave absorption. *J. Colloid Interface Sci.* **2021**, *595*, 168–177.

[69] Weng, X. D.; Li, B. Z.; Zhang, Y.; Lv, X. L.; Gu, G. X. Synthesis of flake shaped carbonyl iron/reduced graphene oxide/polyvinyl pyrrolidone ternary nanocomposites and their microwave absorbing properties. *J. Alloys Compd.* **2017**, *695*, 508–519.

[70] Afghahi, S. S. S.; Shokuhfar, A. Two step synthesis, electromagnetic and microwave absorbing properties of FeCo@C core–shell nanostructure. *J. Magn. Magn. Mater.* **2014**, *370*, 37–44.

[71] Yuan, H. R.; Yan, F.; Li, C. Y.; Zhu, C. L.; Zhang, X. T.; Chen, Y. J. Nickel nanoparticle encapsulated in few-layer nitrogen-doped graphene supported by nitrogen-doped graphite sheets as a high-performance electromagnetic wave absorbing material. *ACS Appl. Mater. Interfaces* **2018**, *10*, 1399–1407.

[72] Cui, X. J.; Jiang, Q. R.; Wang, C. S.; Wang, S. H.; Jiang, Z. Y.; Li, X. A.; Deng, D. H. Encapsulating FeCo alloys by single layer graphene to enhance microwave absorption performance. *Mater. Today Nano* **2021**, *16*, 100138.

[73] Naguib, M.; Kurtoglu, M.; Presser, V.; Lu, J.; Niu, J. J.; Heon, M.; Hultman, L.; Gogotsi, Y.; Barsoum, M. W. Two-dimensional nanocrystals produced by exfoliation of Ti_3AlC_2. *Adv. Mater.* **2011**, *23*, 4248–4253.

[74] Deng, R. X.; Chen, B. B.; Li, H. G.; Li, Z.; Zhang, T.; Yu, Y.; Song, L. X. Adjustable electromagnetic response of ultralight 3D $Ti_3C_2T_x$ composite via control of crystal defects. *Appl. Surf. Sci.* **2021**, *569*, 151053.

[75] Qing, Y. C.; Zhou, W. C.; Luo, F.; Zhu, D. M. Titanium carbide (MXene) nanosheets as promising microwave absorbers. *Ceram. Int.* **2016**, *42*, 16412–16416.

[76] Liu, J.; Zhang, H. B.; Sun, R. H.; Liu, Y. F.; Liu, Z. S.; Zhou, A. G.; Yu, Z. Z. Hydrophobic, flexible, and lightweight MXene foams for high-performance electromagnetic-interference shielding. *Adv. Mater.* **2017**, *29*, 1702367.

[77] Cao, M. S.; Cai, Y. Z.; He, P.; Shu, J. C.; Cao, W. Q.; Yuan, J. 2D MXenes: Electromagnetic property for microwave absorption and electromagnetic interference shielding. *Chem. Eng. J.* **2019**, *359*, 1265–1302.

[78] He, J.; Liu, S.; Deng, L. W.; Shan, D. Y.; Cao, C.; Luo, H.; Yan, S. Q. Tunable electromagnetic and enhanced microwave absorption properties in $CoFe_2O_4$ decorated Ti_3C_2 MXene composites. *Appl. Surf. Sci.* **2020**, *504*, 144210.

[79] He, J.; Shan, D. Y.; Yan, S. Q.; Luo, H.; Cao, C.; Peng, Y. H. Magnetic FeCo nanoparticles-decorated Ti_3C_2 MXene with enhanced microwave absorption performance. *J. Magn. Magn. Mater.* **2019**, *492*, 165639.

[80] Yan, S. Q.; Cao, C.; He, J.; He, L. H.; Qu, Z. W. Investigation on the electromagnetic and broadband microwave absorption properties of Ti_3C_2 Mxene/flaky carbonyl iron composites. *J. Mater. Sci.: Mater. Electron.* **2019**, *30*, 6537–6543.

[81] Feng, W. L.; Luo, H.; Wang, Y.; Zeng, S. F.; Tan, Y. Q.; Deng, L. W.; Zhou, X. S.; Zhang, H. B.; Peng, S. M. Mxenes derived laminated and magnetic composites with excellent microwave absorbing performance. *Sci. Rep.* **2019**, *9*, 3957.

[82] Liu, J. W.; Che, R. C.; Chen, H. J.; Zhang, F.; Xia, F.; Wu, Q. S.; Wang, M. Microwave absorption enhancement of multifunctional composite microspheres with spinel Fe_3O_4 cores and anatase TiO_2 shells. *Small* **2012**, *8*, 1214–1221.

[83] Liu, J. W.; Xu, J. J.; Che, R. C.; Chen, H. J.; Liu, M. M.; Liu, Z. W. Hierarchical Fe_3O_4@TiO_2 yolk–shell microspheres with enhanced microwave-absorption properties. *Chem.—Eur. J.* **2013**, *19*, 6746–6752.

[84] Hua, J. S.; Ma, W. J.; Liu, X. Y.; Zhuang, Q. X.; Wu, Z. Y.; Huang, H.; Lin, S. L. Efficient microwave traps with markedly enhanced interfacial polarization and impedance matching enabled by dual-shelled, dual-cavity magnetic@dielectric hollow nanospheres. *J. Mater. Chem. C* **2020**, *8*, 16489–16497.

[85] Zhang, C. W.; Peng, Y.; Zhang, T. L.; Guo, W. B.; Yuan, Y.; Li, Y. B. *In situ* dual-template method of synthesis of inverse-opal Co_3O_4@TiO_2 with wideband microwave absorption. *Inorg. Chem.* **2021**, *90*, 18455–18465.

[86] Dhawan, S. K.; Singh, K.; Bakhshi, A. K.; Ohlan, A. Conducting polymer embedded with nanoferrite and titanium dioxide nanoparticles for microwave absorption. *Synth. Met.* **2009**, *159*, 2259–2262.

[87] Cao, M. S.; Yang, J.; Song, W. L.; Zhang, D. Q.; Wen, B.; Jin, H.

B.; Hou, Z. L.; Yuan, J. Ferroferric oxide/multiwalled carbon nanotube vs polyaniline/ferroferric oxide/multiwalled carbon nanotube multiheterostructures for highly effective microwave absorption. *ACS Appl. Mater. Interfaces* **2012**, *4*, 6949–6956.

[88] Yang, M. L.; Yuan, Y.; Li, Y.; Sun, X. X.; Wang, S. S.; Liang, L.; Ning, Y. H.; Li, J. J.; Yin, W. L.; Che, R. C. et al. Dramatically enhanced electromagnetic wave absorption of hierarchical CNT/Co/C fiber derived from cotton and metal-organic-framework. *Carbon* **2020**, *161*, 517–527.

[89] Wu, Q.; Wang, B. L.; Fu, Y. G.; Zhang, Z. F.; Yan, P. F.; Liu, T. MOF-derived Co/CoO particles prepared by low temperature reduction for microwave absorption. *Chem. Eng. J.* **2021**, *410*, 128378.

[90] Wang, L.; Wen, B.; Yang, H. B.; Qiu, Y.; He, N. R. Hierarchical nest-like structure of Co/Fe MOF derived CoFe@C composite as wide-bandwidth microwave absorber. *Compos. Part A: Appl. Sci. Manuf.* **2020**, *135*, 105958.

[91] Wang, L.; Du, Z.; Bai, X. Y.; Lin, Y. Constructing macroporous C/Co composites with tunable interfacial polarization toward ultra-broadband microwave absorption. *J. Colloid Interface Sci.* **2021**, *591*, 76–84.

[92] Luo, J. H.; Zhang, K.; Cheng, M. L.; Gu, M. M.; Sun, X. K. MoS_2 spheres decorated on hollow porous ZnO microspheres with strong wideband microwave absorption. *Chem. Eng. J.* **2020**, *380*, 122625.

[93] Najim, M.; Modi, G.; Mishra, Y. K.; Adelung, R.; Singh, D.; Agarwala, V. Ultra-wide bandwidth with enhanced microwave absorption of electroless Ni-P coated tetrapod-shaped ZnO nano- and microstructures. *Phys. Chem. Chem. Phys.* **2015**, *17*, 22923–22933.

[94] Lu, M. M.; Cao, W. Q.; Shi, H. L.; Fang, X. Y.; Yang, J.; Hou, Z. L.; Jin, H. B.; Wang, W. Z.; Yuan, J.; Cao, M. S. Multi-wall carbon nanotubes decorated with ZnO nanocrystals: Mild solution-process synthesis and highly efficient microwave absorption properties at elevated temperature. *J. Mater. Chem. A* **2014**, *2*, 10540.

[95] Xia, T.; Zhang, C.; Oyler, N. A.; Chen, X. B. Hydrogenated TiO_2 nanocrystals: A novel microwave absorbing material. *Adv. Mater.* **2013**, *25*, 6905–6910.

[96] Xia, T.; Zhang, C.; Oyler, N. A.; Chen, X. B. Enhancing microwave absorption of TiO_2 nanocrystals via hydrogenation. *J. Mater. Res.* **2014**, *29*, 2198–2210.

[97] Shi, X. F.; Liu, Z. W.; Li, X.; You, W. B.; Shao, Z. Z.; Che, R. C. Enhanced dielectric polarization from disorder-engineered Fe_3O_4@black TiO_{2-x} heterostructure for broadband microwave absorption. *Chem. Eng. J.* **2021**, *419*, 130020.

[98] Green, M.; Van Tran, A. T.; Smedley, R.; Roach, A.; Murowchick, J.; Chen, X. B. Microwave absorption of magnesium/hydrogen-treated titanium dioxide nanoparticles. *Nano Mater. Sci.* **2019**, *1*, 48–59.

[99] Tian, L. H.; Xu, J. L.; Just, M.; Green, M.; Liu, L.; Chen, X. B. Broad range energy absorption enabled by hydrogenated TiO_2 nanosheets: From optical to infrared and microwave. *J. Mater. Chem. C* **2017**, *5*, 4645–4653.

[100] Ni, Q. Q.; Zhu, Y. F.; Yu, L. J.; Fu, Y. Q. One-dimensional carbon nanotube@barium titanate@polyaniline multiheterostructures for microwave absorbing application. *Nanoscale Res. Lett.* **2015**, *10*, 174.

[101] Munir, A. Microwave radar absorbing properties of multiwalled carbon nanotubes polymer composites: A review. *Adv. Polym. Technol.* **2017**, *36*, 362–370.

[102] Wen, F. S.; Zhang, F.; Liu, Z. Y. Investigation on microwave absorption properties for multiwalled carbon nanotubes/Fe/Co/Ni nanopowders as lightweight absorbers. *J. Phys. Chem. C* **2011**, *115*, 14025–14030.

[103] Sarkar, D.; Bhattacharya, A.; Nandy, P.; Das, S. Enhanced broadband microwave reflection loss of carbon nanotube ensheathed Ni-Zn-Co-ferrite magnetic nanoparticles. *Mater. Lett.* **2014**, *120*, 259–262.

[104] Li, N.; Huang, G. W.; Li, Y. Q.; Xiao, H. M.; Feng, Q. P.; Hu, N.; Fu, S. Y. Enhanced microwave absorption performance of coated carbon nanotubes by optimizing the Fe_3O_4 nanocoating structure. *ACS Appl. Mater. Interfaces* **2017**, *9*, 2973–2983.

[105] Jiao, Z. M.; Qiu, J. Microwave absorption performance of iron oxide/multiwalled carbon nanotubes nanohybrids prepared by electrostatic attraction. *J. Mater. Sci.* **2018**, *53*, 3640–3646.

[106] Kuang, D. T.; Wang, S. L.; Hou, L. Z.; Luo, H.; Deng, L. W.; Chen, C. S.; Song, M.; Mead, J. L.; Huang, H. A Comparative study on the dielectric response and microwave absorption performance of FeNi-capped carbon nanotubes and FeNi-cored carbon nanoparticles. *Nanotechnology* **2021**, *32*, 105701.

[107] Saeed, M. S.; Seyed-Yazdi, J.; Hekmatara, S. H. Surface modification of MWCNT with cluster form of Fe_2O_3/Fe_3O_4 NPs for improving their microwave absorption performance. *Chem. Phys. Lett.* **2020**, *756*, 137823.

[108] Saeed, M. S.; Seyed-Yazdi, J.; Hekmatara, H. Fe_2O_3/Fe_3O_4/PANI/MWCNT nanocomposite with the optimum amount and uniform orientation of Fe_2O_3/Fe_3O_4 NPs in polyaniline for high microwave absorbing performance. *J. Alloys Compd.* **2020**, *843*, 156052.

[109] Liang, X. H.; Quan, B.; Chen, J. B.; Gu, W. H.; Zhang, B. S.; Ji, G. B. Nano bimetallic@carbon layer on porous carbon nanofibers with multiple interfaces for microwave absorption applications. *ACS Appl. Nano Mater.* **2018**, *1*, 5712–5721.

[110] Song, Y.; Yin, F. X.; Zhang, C. W.; Guo, W. B.; Han, L. Y.; Yuan, Y. Three-dimensional ordered mesoporous carbon spheres modified with ultrafine zinc oxide nanoparticles for enhanced microwave absorption properties. *Nano-Micro Lett.* **2021**, *13*, 76.

[111] Fan, Y. Q.; Li, Y. H.; Yao, Y. L.; Sun, Y.; Tong, B. H.; Zhan, J. Hierarchically porous carbon sheets/Co nanofibers derived from corncobs for enhanced microwave absorbing properties. *Appl. Surf. Sci.* **2020**, *534*, 147510.

[112] Liu, P. B.; Zhu, C. Y.; Gao, S.; Guan, C.; Huang, Y.; He, W. J. N-doped porous carbon nanoplates embedded with CoS_2 vertically anchored on carbon cloths for flexible and ultrahigh microwave absorption. *Carbon* **2020**, *163*, 348–359.

[113] Wen, B.; Yang, H. B.; Wang, L.; Qiu, Y. Hierarchical Co_xAl_y layered double hydroxide@carbon composites derived from metal-organic frameworks with efficient broadband electromagnetic wave absorption. *J. Mater. Chem. C* **2020**, *8*, 16418–16426.

[114] Liu, P. B.; Gao, S.; Wang, Y.; Zhou, F. T.; Huang, Y.; Luo, J. H. Metal-organic polymer coordination materials derived Co/N-doped porous carbon composites for frequency-selective microwave absorption. *Compos. Part B: Eng.* **2020**, *202*, 108406.

[115] Zhang, X. M.; Ji, G. B.; Liu, W.; Quan, B.; Liang, X. H.; Shang, C. M.; Cheng, Y.; Du, Y. W. Thermal conversion of an Fe_3O_4@metal-organic framework: A new method for an efficient Fe-Co/nanoporous carbon microwave absorbing material. *Nanoscale* **2015**, *7*, 12932–12942.

[116] Chen, Y. J.; Cao, M. S.; Wang, T. H.; Wan, Q. Microwave absorption properties of the ZnO nanowire-polyester composites. *Appl. Phys. Lett.* **2004**, *84*, 3367–3369.

[117] Wang, L.; Li, X.; Li, Q. Q.; Yu, X. F.; Zhao, Y. H.; Zhang, J.; Wang, M.; Che, R. C. Oriented polarization tuning broadband absorption from flexible hierarchical ZnO arrays vertically supported on carbon cloth. *Small* **2019**, *15*, 1900900.

[118] Feng, W.; Wang, Y. M.; Chen, J. C.; Wang, L.; Guo, L. X.; Ouyang, J. H.; Jia, D. C.; Zhou, Y. Reduced graphene oxide decorated with *in-situ* growing ZnO nanocrystals: Facile synthesis and enhanced microwave absorption properties. *Carbon* **2016**, *108*, 52–60.

[119] Zhou, Z. W.; Chu, L. S.; Hu, S. C. Microwave absorption behaviors of tetra-needle-like ZnO whiskers. *Mater. Sci. Eng.: B* **2006**, *126*, 93–96.

[120] Wu, Q. B.; Zhao, W.; Zeng, G. X.; Zhang, H. Y.; Wei, A. X.; Wang, J. Microwave absorption properties of Mn- and Ni-doped zinc oxides. *J. Vac. Sci. Technol. A* **2011**, *29*, 03A113.

[121] Tang, X.; Hu, K. A. Preparation and electromagnetic wave absorption properties of Fe-doped zinc oxide coated barium ferrite composites. *Mater. Sci. Eng.: B* **2007**, *139*, 119–123.

[122] Cao, J.; Fu, W. Y.; Yang, H. B.; Yu, Q. J.; Zhang, Y. Y.; Liu, S. K.; Sun, P.; Zhou, X. M.; Leng, Y.; Wang, S. M. et al. Large-scale

synthesis and microwave absorption enhancement of actinomorphic tubular ZnO/$CoFe_2O_4$ nanocomposites. *J. Phys. Chem. B* **2009**, *113*, 4642–4647.

[123] Guan, X. M.; Yang, Z. H.; Zhou, M.; Yang, L.; Peymanfar, R.; Aslibeiki, B.; Ji, G. B. 2D MXene nanomaterials: Synthesis, mechanism, and multifunctional applications in microwave absorption. *Small Struct.* **2022**, *3*, 2200102.

[124] Wu, Y. H.; Wang, G. D.; Yuan, X. X.; Fang, G.; Li, P.; Ji, G. B. Heterointerface engineering in hierarchical assembly of the Co/$Co(OH)_2$@carbon nanosheets composites for wideband microwave absorption. *Nano Res.* **2023**, *16*, 2611–2621.

[125] Gu, W. H.; Ong, S. J. H.; Shen, Y. H.; Guo, W. Y.; Fang, Y. T.; Ji, G. B.; Xu, Z. J. A lightweight, elastic, and thermally insulating stealth foam with high infrared-radar compatibility. *Adv. Sci.* **2022**, *9*, 2204165.

[126] Huang, Q. Q.; Zhao, Y.; Wu, Y.; Zhou, M.; Tan, S. J.; Tang, S. L.; Ji, G. B. A dual-band transceiver with excellent heat insulation property for microwave absorption and low infrared emissivity compatibility. *Chem. Eng. J.* **2022**, *446*, 137279.

[127] Bao, S. S.; Song, Z. J.; Mao, R. J.; Li, Y.; Zhang, S. H.; Jiang, Z. Y.; Li, X. A.; Xie, Z. X. Synthesis of hollow rod-like hierarchical structures assembled by CoFe/C nanosheets for enhanced microwave absorption. *J. Mater. Chem. C* **2021**, *9*, 13860–13868.

[128] Han, Z.; Li, D.; Wang, H.; Liu, X. G.; Li, J.; Geng, D. Y.; Zhang, Z. D. Broadband electromagnetic-wave absorption by FeCo/C nanocapsules. *Appl. Phys. Lett.* **2009**, *95*, 023114.

[129] Yan, L. L.; Liu, J.; Zhao, S. C.; Zhang, B.; Gao, Z.; Ge, H. B.; Chen, Y.; Cao, M. S.; Qin, Y. Coaxial multi-interface hollow Ni-Al_2O_3-ZnO nanowires tailored by atomic layer deposition for selectivefrequency absorptions. *Nano Res.* **2017**, *10*, 1595–1607.

[130] Liu, Q. H.; Xu, X. H.; Xia, W. X.; Che, R. C.; Chen, C.; Cao, Q.; He, J. G. Dependency of magnetic microwave absorption on surface architecture of $Co_{20}Ni_{80}$ hierarchical structures studied by electron holography. *Nanoscale* **2015**, *7*, 1736–1743.

[131] Almessiere, M. A.; Algarou, N. A.; Slimani, Y.; Sadaqat, A.; Baykal, A.; Manikandan, A.; Trukhanov, S. V.; Trukhanov, A. V.; Ercan, I. Investigation of exchange coupling and microwave properties of hard/soft $(SrNi_{0.02}Zr_{0.01}Fe_{11.96}O_{19})/(CoFe_2O_4)_x$ nanocomposites. *Mater. Today Nano* **2022**, *18*, 100186.

[132] Tao, F. J.; Green, M.; Van Tran, A. T.; Zhang, Y. L.; Yin, Y. S.; Chen, X. B. Plasmonic Cu_9S_5 nanonets for microwave absorption. *ACS Appl. Nano Mater.* **2019**, *2*, 3836–3847.

[133] Lv, H. L.; Liang, X. H.; Ji, G. B.; Zhang, H. Q.; Du, Y. W. Porous three-dimensional flower-like Co/CoO and its excellent electromagnetic absorption properties. *ACS Appl. Mater. Interfaces* **2015**, *7*, 9776–9783.

[134] Duan, Y. P.; Liu, Z.; Jing, H.; Zhang, Y. H.; Li, S. Q. Novel microwave dielectric response of Ni/Co-doped manganese dioxides and their microwave absorbing properties. *J. Mater. Chem.* **2012**, *22*, 18291–18299.

[135] Jazirehpour, M.; Seyyed Ebrahimi, S. A. Effect of aspect ratio on dielectric, magnetic, percolative and microwave absorption properties of magnetite nanoparticles. *J. Alloys Compd.* **2015**, *638*, 188–196.

[136] Gill, N.; Singh, J.; Puthucheri, S.; Singh, D. Thin and broadband two-layer microwave absorber in 4–12 GHz with developed flaky cobalt material. *Electron. Mater. Lett.* **2018**, *14*, 288–297.

[137] Li, Q. Q.; Liu, J. W.; Zhao, Y. H.; Zhao, X. B.; You, W. B.; Li, X.; Che, R. C. "Matryoshka doll"-like CeO_2 microspheres with hierarchical structure to achieve significantly enhanced microwave absorption performance. *ACS Appl. Mater. Interfaces* **2018**, *10*, 27540–27547.

[138] Zhang, R. X.; Wang, L.; Xu, C. Y.; Liang, C. Y.; Liu, X. H.; Zhang, X. F.; Che, R. C. Vortex tuning magnetization configurations in porous Fe_3O_4 nanotube with wide microwave absorption frequency. *Nano Res.* **2022**, *15*, 6743–6750.

[139] Liu, X. F.; Hao, C. C.; He, L. H.; Yang, C.; Chen, Y. B.; Jiang, C. B.; Yu, R. H. Yolk–shell structured Co-C/Void/Co_9S_8 composites with a tunable cavity for ultrabroadband and efficient low-frequency microwave absorption. *Nano Res.* **2018**, *11*, 4169–4182.

[140] Yang, B. T.; Fang, J. F.; Xu, C. Y.; Cao, H.; Zhang, R. X.; Zhao, B.; Huang, M. Q.; Wang, X. Y.; Lv, H. L.; Che, R. C. One-dimensional magnetic FeCoNi alloy toward low-frequency electromagnetic wave absorption. *Nano-Micro Lett.* **2022**, *14*, 170.

[141] Cheng, Y. F.; Bi, H.; Wang, C.; Cao, Q.; Jiao, W. L.; Che, R. C. Dual-ligand mediated one-pot self-assembly of Cu/ZnO core/shell structures for enhanced microwave absorption. *RSC Adv.* **2016**, *6*, 41724–41733.

[142] Liu, L.; He, P. G.; Zhou, K. C.; Chen, T. F. Microwave absorption properties of helical carbon nanofibers-coated carbon fibers. *AIP Adv.* **2013**, *3*, 082112.

[143] Tong, G. X.; Wu, W. H.; Guan, J. G.; Wang, J. P.; Ma, J.; Yuan, J. H.; Wang, S. L. Solution synthesis and novel magnetic properties of ball-chain iron nanofibers. *J. Mater. Res.* **2011**, *26*, 2590–2598.

[144] Liang, C. Y.; Wang, Z. J. Controllable fabricating dielectric-dielectric SiC@C core–shell nanowires for high-performance electromagnetic wave attenuation. *ACS Appl. Mater. Interfaces* **2017**, *9*, 40690–40696.

[145] Huang, Y.; Xie, A. M.; Seidi, F.; Zhu, W. Y.; Li, H.; Yin, S.; Xu, X.; Xiao, H. N. Core–shell heterostructured nanofibers consisting of Fe_7S_8 nanoparticles embedded into S-doped carbon nanoshells for superior electromagnetic wave absorption. *Chem. Eng. J.* **2021**, *423*, 130307.

[146] Li, X. H.; Guo, X. H.; Liu, T. C.; Zheng, X. L.; Bai, J. T. Shape-controlled synthesis of Fe nanostructures and their enhanced microwave absorption properties at L-band. *Mater. Res. Bull.* **2014**, *59*, 137–141.

[147] Niu, F. X.; Wang, Y. X.; Ma, L. R.; Xie, Z. Y.; Wang, Y. Y.; Wang, C. G.; Mao, Y. P. Achieving enhanced dielectric property via growing Co-Ni-P nano-alloys on SiC nanowires with 3D conductive network. *J. Alloys Compd.* **2019**, *778*, 933–941.

[148] Li, Z. C.; Ye, F.; Cheng, L. F.; Wang, P.; Guo, C. C.; Li, M. H.; Zhang, L. T. Synthesis of Si-C-N aligned nanofibers with preeminent electromagnetic wave absorption in ultra-broad band. *J. Mater. Chem. C* **2021**, *9*, 16966–16977.

[149] Yang, J. N.; Guan, G. G.; Yan, L.; Xu, J. H.; Xiang, J.; Zhang, K. Y. FeCo/ZnO composite nanofibers for broadband and high efficiency microwave absorption. *Adv. Mater. Interfaces* **2021**, *8*, 2101047.

[150] Liu, X. G.; Geng, D. Y.; Meng, H.; Shang, P. J.; Zhang, Z. D. Microwave-absorption properties of ZnO-coated iron nanocapsules. *Appl. Phys. Lett.* **2008**, *92*, 173117.

[151] He, P.; Hou, Z. L.; Zhang, K. L.; Li, J.; Yin, K.; Feng, S.; Bi, S. Lightweight ferroferric oxide nanotubes with natural resonance property and design for broadband microwave absorption. *J. Mater. Sci.* **2017**, *52*, 8258–8267.

[152] Wang, X.; Gong, R. Z.; Li, P. G.; Liu, L. Y.; Cheng, W. M. Effects of aspect ratio and particle size on the microwave properties of Fe-Cr-Si-Al alloy flakes. *Mater. Sci. Eng.: A* **2007**, *466*, 178–182.

[153] Gill, N.; Puthucheri, S.; Singh, D.; Agarwala, V. Critical analysis of frequency selective surfaces embedded composite microwave absorber for frequency range 2–8 GHz. *J. Mater. Sci.: Mater. Electron* **2017**, *28*, 1259–1270.

[154] Qian, K.; Li, Q. F.; Sokolov, A.; Yu, C. J.; Kulik, P.; Fitchorova, O.; Chen, Y. J.; Chinnasamy, C.; Harris, V. G. Electromagnetic shielding effectiveness of amorphous metallic spheroidal- and flake-based magnetodielectric composites. *J. Mater. Sci. Technol.* **2021**, *83*, 256–263.

[155] Yan, J.; Huang, Y.; Zhang, X. Y.; Gong, X.; Chen, C.; Nie, G. D.; Liu, X. D.; Liu, P. B. MoS_2-decorated/integrated carbon fiber: Phase engineering well-regulated microwave absorber. *Nano-Micro Lett.* **2021**, *13*, 114.

[156] Wang, Z.; Cheng, Z.; Fang, C. Q.; Hou, X. L.; Xie, L. Recent advances in MXenes composites for electromagnetic interference shielding and microwave absorption. *Compos. Part A: Appl. Sci. Manuf.* **2020**, *136*, 105956.

[157] Huang, L. N.; Chen, C. G.; Li, Z. J.; Zhang, Y. P.; Zhang, H.; Lu, J. G.; Ruan, S. C.; Zeng, Y. J. Challenges and future perspectives on microwave absorption based on two-dimensional materials and structures. *Nanotechnology* **2019**, *31*, 162001.

[158] Wang, P.; Zhang, J. M.; Chen, Y. W.; Wang, G. W.; Wang, D.;

Wang, T.; Li, F. S. Magnetism and microwave absorption properties of Fe_3O_4 microflake-paraffin composites without and with magnetic orientation. *J. Electron. Mater.* **2018**, *47*, 721–729.
[159] Liu, Y. F.; Wang, J.; Li, J. Y.; Tian, W.; Jian, X. Electrical discharge approach for large-scale and high-thermostability FeCoNi Kovar alloy microwave absorbers covering the low-frequency bands. *J. Alloys Compd.* **2022**, *907*, 164509.
[160] Duan, Y. P.; Pang, H. F.; Wen, X.; Zhang, X. F.; Wang, T. M. Microwave absorption performance of $FeCoNiAlCr_{0.9}$ alloy powders by adjusting the amount of process control agent. *J. Mater. Sci. Technol.* **2021**, *77*, 209–216.
[161] Zhang, Y. L.; Piao, M. X.; Zhang, H.; Zhang, F.; Chu, J.; Wang, X.; Shi, H. F.; Li, C. L. Synthesis of mesoporous hexagonal cobalt nanosheets with low permittivity for enhancing microwave absorption performances. *J. Magn. Magn. Mater.* **2019**, *486*, 165272.
[162] Abshinova, M. A.; Li, Z. W. Effect of milling time on dynamic permeability values of reduced carbonyl iron filled composites. *J. Magn. Magn. Mater.* **2014**, *369*, 147–154.
[163] Turtelli, R. S.; Grössinger, R.; Kussbach, C.; Sinnecker, J. P. Study of frequency dependencies of the complex magnetic Ac-permeability aftereffect in amorphous $Fe_{64}Co_{21}B_{15}$ and $Fe_8Co_{77}B_{15}$ alloys. *J. Appl. Phys.* **1998**, *83*, 1581–1587.
[164] Ma, F.; Qin, Y.; Li, Y. Z. Enhanced microwave performance of cobalt nanoflakes with strong shape anisotropy. *Appl. Phys. Lett.* **2010**, *96*, 202507.
[165] Wu, M. Z.; Zhang, Y. D.; Hui, S.; Xiao, T. D.; Ge, S. H.; Hines, W. A.; Budnick, J. I.; Taylor, G. W. Microwave magnetic properties of $Co_{50}/(SiO_2)_{50}$ nanoparticles. *Appl. Phys. Lett.* **2002**, *80*, 4404–4406.
[166] He, J. H.; Wang, W.; Guan, J. G. Internal strain dependence of complex permeability of ball milled carbonyl iron powders in 2–18 GHz. *J. Appl. Phys.* **2012**, *111*, 093924.
[167] Zhang, X. F.; Dong, X. L.; Huang, H.; Lv, B.; Lei, J. P.; Choi, C. J. Microstructure and microwave absorption properties of carbon-coated iron nanocapsules. *J. Phys. D: Appl. Phys.* **2007**, *40*, 5383–5387.
[168] Aharoni, A. Effect of surface anisotropy on the exchange resonance modes. *J. Appl. Phys.* **1997**, *81*, 830–833.
[169] Peng, K. S.; Fang, G.; Guo, C.; Liu, C. Y.; Xu, G. Y.; Xiao, A. D.; Zhang, Y. T.; Zhang, Y. J. Microwave absorption enhancement of FeCoNi contributed by improved crystallinity and flake-like particles. *J. Magn. Magn. Mater.* **2019**, *490*, 165488.
[170] You, W. B.; Che, R. C. Excellent NiO-Ni nanoplate microwave absorber via pinning effect of antiferromagnetic–ferromagnetic interface. *ACS Appl. Mater. Interfaces* **2018**, *10*, 15104–15111.
[171] Shi, X. F.; You, W. B.; Li, X.; Wang, L.; Shao, Z. Z.; Che, R. C. *In-situ* regrowth constructed magnetic coupling 1D/2D Fe assembly as broadband and high-efficient microwave absorber. *Chem. Eng. J.* **2021**, *415*, 128951.
[172] Zhang, Y. B.; Wang, P.; Wang, Y.; Qiao, L.; Wang, T.; Li, F. S. Synthesis and excellent electromagnetic wave absorption properties of parallel aligned FeCo@C core–shell nanoflake composites. *J. Mater. Chem. C* **2015**, *3*, 10813–10818.
[173] Zheng, J. J.; He, X. S.; Li, Y. C.; Zhao, B.; Ye, F. C.; Gao, C. F.; Li, M. J.; Li, X. P.; E, S. J. Viscoelastic and magnetically aligned flaky Fe-based magnetorheological elastomer film for wide-bandwidth electromagnetic wave absorption. *Ind. Eng. Chem. Res.* **2020**, *59*, 3425–3437.
[174] Min, D. D.; Zhou, W. C.; Qing, Y.; Luo, F.; Zhu, D. M. Greatly enhanced microwave absorption properties of highly oriented flake carbonyl iron/epoxy resin composites under applied magnetic field. *J. Mater. Sci.* **2017**, *52*, 2373–2383.
[175] Liu, Q. H.; Cao, Q.; Bi, H.; Liang, C. Y.; Yuan, K. P.; She, W.; Yang, Y. J.; Che, R. C. CoNi@SiO_2@TiO_2 and CoNi@Air@TiO_2 microspheres with strong wideband microwave absorption. *Adv. Mater.* **2016**, *28*, 486–490.
[176] Zhao, B.; Guo, X. Q.; Zhao, W. Y.; Deng, J. S.; Fan, B. B.; Shao, G.; Bai, Z. Y.; Zhang, R. Facile synthesis of yolk–shell Ni@void@SnO_2(Ni_3Sn_2) ternary composites via galvanic replacement/Kirkendall effect and their enhanced microwave absorption properties. *Nano Res.* **2017**, *10*, 331–343.
[177] Li, H.; Bao, S. S.; Li, Y. M.; Huang, Y. Q.; Chen, J. Y.; Zhao, H.; Jiang, Z. Y.; Kuang, Q.; Xie, Z. X. Optimizing the electromagnetic wave absorption performances of designed Co_3Fe_7@C yolk–shell structures. *ACS Appl. Mater. Interfaces* **2018**, *10*, 28839–28849.
[178] Liu, Z. W.; Che, R. C.; Wei, Y.; Liu, Y. P.; Elzatahry, A. A.; Dahyan, D. A.; Zhao, D. Broadening microwave absorption via a multi-domain structure. *APL Mater.* **2017**, *5*, 046104.
[179] Deng, Z. M.; Li, Y.; Zhang, H. B.; Zhang, Y.; Luo, J. Q.; Liu, L. X.; Yu, Z. Z. Lightweight Fe@C hollow microspheres with tunable cavity for broadband microwave absorption. *Compos. Part B: Eng.* **2019**, *177*, 107346.
[180] Zeng, Q.; Xiong, X. H.; Chen, P.; Yu, Q.; Wang, Q.; Wang, R. C.; Chu, H. R. Air@rGO€Fe_3O_4 microspheres with spongy shells: Self-assembly and microwave absorption performance. *J. Mater. Chem. C* **2016**, *4*, 10518–10528.
[181] He, N.; He, Z. D.; Liu, L.; Lu, Y.; Wang, F. Q.; Wu, W. H.; Tong, G. X. Ni^{2+} Guided phase/structure evolution and ultra-wide bandwidth microwave absorption of Co_xNi_{1-x} alloy hollow microspheres. *Chem. Eng. J.* **2020**, *381*, 122743.
[182] Cheng, Y.; Cao, J. M.; Li, Y.; Li, Z. Y.; Zhao, H. Q.; Ji, G. B.; Du, Y. W. The outside-in approach to construct Fe_3O_4 nanocrystals/mesoporous carbon hollow spheres core–shell hybrids toward microwave absorption. *ACS Sustainable Chem. Eng.* **2018**, *6*, 1427–1435.
[183] Liu, P. B.; Gao, S.; Liu, X. D.; Huang, Y.; He, W. J.; Li, Y. T. Rational construction of hierarchical hollow CuS@CoS_2 nanoboxes with heterogeneous interfaces for high-efficiency microwave absorption materials. *Compos. Part B: Eng.* **2020**, *192*, 107992.
[184] You, W. B.; Bi, H.; She, W.; Zhang, Y.; Che, R. C. Dipolar-distribution cavity γ-Fe_2O_3@C@α-MnO_2 nanospindle with broadened microwave absorption bandwidth by chemically etching. *Small* **2017**, *13*, 1602779.
[185] Liu, J. W.; Cheng, J.; Che, R. C.; Xu, J. J.; Liu, M. M.; Liu, Z. W. Synthesis and microwave absorption properties of yolk–shell microspheres with magnetic iron oxide cores and hierarchical copper silicate shells. *ACS Appl. Mater. Interfaces* **2013**, *5*, 2503–2509.
[186] Liu, Y.; Liu, X. X.; Wang, X. J. Double-layer microwave absorber based on $CoFe_2O_4$ ferrite and carbonyl iron composites. *J. Alloys Compd.* **2014**, *584*, 249–253.
[187] Ling, A.; Tan, G. G.; Man, Q. K.; Lou, Y. X.; Chen, S. W.; Gu, X. S.; Li, R. W.; Pan, J.; Liu, X. C. Broadband microwave absorbing materials based on MWCNTs' electromagnetic wave filtering effect. *Compos. Part B: Eng.* **2019**, *171*, 214–221.
[188] Anwar, R. S.; Mao, L. F.; Ning, H. S. Frequency selective surfaces: A review. *Appl. Sci.* **2018**, *8*, 1689.
[189] Chen, W. Q.; Xiao, P. S.; Chen, H. H.; Zhang, H. T.; Zhang, Q. C.; Chen, Y. S. Polymeric graphene bulk materials with a 3D cross-linked monolithic graphene network. *Adv. Mater.* **2019**, *31*, 1802403.
[190] Kong, L.; Yin, X. W.; Xu, H. L.; Yuan, X. Y.; Wang, T.; Xu, Z. W.; Huang, J. F.; Yang, R.; Fan, H. Powerful absorbing and lightweight electromagnetic shielding CNTs/RGO composite. *Carbon* **2019**, *145*, 61–66.
[191] Zhou, X. F.; Jia, Z. R.; Feng, A. L.; Wang, X. X.; Liu, J. J.; Zhang, M.; Cao, H. J.; Wu, G. L. Synthesis of fish skin-derived 3D carbon foams with broadened bandwidth and excellent electromagnetic wave absorption performance. *Carbon* **2019**, *152*, 827–836.
[192] Wang, S. S.; Zhao, Y.; Gao, M. M.; Xue, H. L.; Xu, Y. C.; Feng, C. H.; Shi, D. X.; Liu, K. H.; Jiao, Q. Z. Green synthesis of porous cocoon-like rGO for enhanced microwave-absorbing performances. *ACS Appl. Mater. Interfaces* **2018**, *10*, 42865–42874.
[193] Li, T.; Zhi, D. D.; Chen, Y.; Li, B.; Zhou, Z. W.; Meng, F. B. Multiaxial electrospun generation of hollow graphene aerogel spheres for broadband high-performance microwave absorption. *Nano Res.* **2020**, *13*, 477–484.
[194] Zhang, Z. W.; Cai, Z. H.; Xia, L.; Zhao, D.; Fan, F.; Huang, Y. Synergistically assembled cobalt-telluride/graphene foam with high-performance electromagnetic wave absorption in both gigahertz and terahertz band ranges. *ACS Appl. Mater. Interfaces* **2021**, *13*, 30967–30979.

[195] Wang, K. F.; Chu, W. S.; Li, H.; Chen, Y. J.; Cai, Y. L.; Liu, H. Z. Ferromagnetic Ti_3CNCl_2-decorated RGO aerogel: From 3D interconnecting conductive network construction to ultra-broadband microwave absorber with thermal insulation property. *J. Colloid Interface Sci.* **2021**, *604*, 402–414.

[196] Guo, C.; Itoh, K.; Sun, D. M.; Kondo, Y.; Fuji, M. Carbon nanotube/polysiloxane foams with tunable absorption bands for electromagnetic wave shielding. *ACS Appl. Nano Mater.* **2020**, *3*, 5944–5954.

[197] Aslam, M. A.; Ding, W.; ur Rehman, S.; Hassan, A.; Bian, Y. C.; Liu, Q. C.; Sheng, Z. G. Low cost 3D bio-carbon foams obtained from wheat straw with broadened bandwidth electromagnetic wave absorption performance. *Appl. Surf. Sci.* **2021**, *543*, 148785.

[198] Zhang, M.; Ling, H. L.; Wang, T.; Jiang, Y. J.; Song, G. Y.; Zhao, W.; Zhao, L. B.; Cheng, T. T.; Xie, Y. X.; Guo, Y. Y. et al. An equivalent substitute strategy for constructing 3D ordered porous carbon foams and their electromagnetic attenuation mechanism. *Nano-Micro Lett.* **2022**, *14*, 157.

[199] Xi, J. B.; Liu, Y. J.; Wu, Y.; Hu, J. H.; Gao, W. W.; Zhou, E. Z.; Chen, H. H.; Chen, Z. C.; Chen, Y. S.; Gao, C. Multifunctional bicontinuous composite foams with ultralow percolation thresholds. *ACS Appl. Mater. Interfaces* **2018**, *10*, 20806–20815.

[200] Lou, Z. C.; Li, R.; Wang, P.; Zhang, Y.; Chen, B.; Huang, C. X.; Wang, C. C.; Han, H.; Li, Y. J. Phenolic foam-derived magnetic carbon foams (MCFs) with tunable electromagnetic wave absorption behavior. *Chem. Eng. J.* **2020**, *391*, 123571.

[201] Jiao, Z. B.; Huyan, W. J.; Yang, F.; Yao, J. R.; Tan, R. Y.; Chen, P.; Tao, X. W.; Yao, Z. J.; Zhou, J. T.; Liu, P. J. Achieving ultra-wideband and elevated temperature electromagnetic wave absorption via constructing lightweight porous rigid structure. *Nano-Micro Lett.* **2022**, *14*, 173.

[202] Zhang, Y.; Huang, Y.; Zhang, T. F.; Chang, H. C.; Xiao, P. S.; Chen, H. H.; Huang, Z. Y.; Chen, Y. S. Broadband and tunable high-performance microwave absorption of an ultralight and highly compressible graphene foam. *Adv. Mater.* **2015**, *27*, 2049–2053.

[203] Huang, Z. Y.; Chen, H. H.; Huang, Y.; Ge, Z.; Zhou, Y.; Yang, Y.; Xiao, P. S.; Liang, J. J.; Zhang, T. F.; Shi, Q. et al. Ultra-broadband wide-angle terahertz absorption properties of 3D graphene foam. *Adv. Funct. Mater.* **2018**, *28*, 1704363.

[204] Chen, H. H.; Huang, Z. Y.; Huang, Y.; Zhang, Y.; Ge, Z.; Ma, W. L.; Zhang, T. F.; Wu, M. M.; Xu, S. T.; Fan, F. et al. Consecutively strong absorption from gigahertz to terahertz bands of a monolithic three-dimensional Fe_3O_4/graphene material. *ACS Appl. Mater. Interfaces* **2019**, *11*, 1274–1282.

[205] Yang, X.; Duan, Y. P.; Li, S. Q.; Huang, L. X.; Pang, H. F.; Ma, B.; Wang, T. M. Constructing three-dimensional reticulated carbonyl iron/carbon foam composites to achieve temperature-stable broadband microwave absorption performance. *Carbon* **2022**, *188*, 376–384.

[206] Wang, Y. Y.; Sun, W. J.; Dai, K.; Yan, D. X.; Li, Z. M. Flexible and heat-resistant carbon nanotube/graphene/polyimide foam for broadband microwave absorption. *Compos. Sci. Technol.* **2021**, *212*, 108848.

[207] Wu, F.; Li, Y.; Lan, X. Q.; Huang, P. K.; Chong, Y. K.; Luo, H. B.; Shen, B.; Zheng, W. G. Large-scale fabrication of lightweight, tough polypropylene/carbon black composite foams as broadband microwave absorbers. *Compos. Commun.* **2020**, *20*, 100358.

[208] Li, W. C.; Li, C. S.; Lin, L. H.; Wang, Y.; Zhang, J. S. All-dielectric radar absorbing array metamaterial based on silicon carbide/carbon foam material. *J. Alloys Compd.* **2019**, *781*, 883–891.

[209] Li, X. M.; Zhou, G. Y.; Yang, Q.; Zhu, X. T.; Ren, G. N.; Liu, L. Preparation and performance of electromagnetic wave absorbing foamed ceramics with high closed porosity and gradient SiC distribution. *Ceram. Int.* **2020**, *46*, 2294–2299.

[210] Li, W. C.; Lin, L. H.; Li, C. S.; Wang, Y.; Zhang, J. S. Radar absorbing combinatorial metamaterial based on silicon carbide/carbon foam material embedded with split square ring metal. *Results Phys.* **2019**, *12*, 278–286.

[211] Qin, M.; Zhang, L. M.; Zhao, X. R.; Wu, H. J. Lightweight Ni foam-based ultra-broadband electromagnetic wave absorber. *Adv. Funct. Mater.* **2021**, *31*, 2103436.

[212] Sun, H. D.; Zhang, Y.; Wu, Y.; Zhao, Y.; Zhou, M.; Liu, L.; Tang, S. L.; Ji, G. B. Broadband absorption of macro pyramid structure based flame retardant absorbers. *J. Mater. Sci. Technol.* **2022**, *128*, 228–238.

[213] Huang, Q. Q.; Wang, G. H.; Zhou, M.; Zheng, J.; Tang, S. L.; Ji, G. B. Metamaterial electromagnetic wave absorbers and devices: Design and 3D microarchitecture. *J. Mater. Sci. Technol.* **2022**, *108*, 90–101.

[214] Zhang, H. T.; Zhang, J. S.; Zhang, H. Y. Computation of radar absorbing silicon carbide foams and their silica matrix composites. *Comput. Mater. Sci.* **2007**, *38*, 857–864.

[215] Liu, Q. L.; Cao, B.; Feng, C. L.; Zhang, W.; Zhu, S. M.; Zhang, D. High permittivity and microwave absorption of porous graphitic carbons encapsulating Fe nanoparticles. *Compos. Sci. Technol.* **2012**, *72*, 1632–1636.

[216] Liu, Y.; He, D. L.; Dubrunfaut, O.; Zhang, A. N.; Zhang, H. L.; Pichon, L.; Bai, J. B. GO-CNTs hybrids reinforced epoxy composites with porous structure as microwave absorbers. *Compos. Sci. Technol.* **2020**, *200*, 108450.

[217] Yang, X. C.; Jing, M. X.; Shen, X. Q.; Meng, X. F.; Dong, M. D.; Huang, D. Q.; Wang, Y. D. Microwave absorption of sandwich structure based on nanocrystalline $SrFe_{12}O_{19}$, $Ni_{0.5}Zn_{0.5}Fe_2O_4$ and α-Fe hollow microfibers. *J. Nanosci. Nanotechnol.* **2014**, *14*, 2419–2424.

[218] Choi, J.; Jung, H. T. A new triple-layered composite for high-performance broadband microwave absorption. *Compos. Struct.* **2015**, *122*, 166–171.

[219] Wang, T.; Wang, P.; Wang, Y.; Qiao, L. A broadband far-field microwave absorber with a sandwich structure. *Mater. Des.* **2016**, *95*, 486–489.

[220] Sun, H.; Che, R. C.; You, X.; Jiang, Y. S.; Yang, Z. B.; Deng, J.; Qiu, L. B.; Peng, H. S. Cross-stacking aligned carbon-nanotube films to tune microwave absorption frequencies and increase absorption intensities. *Adv. Mater.* **2014**, *26*, 8120–8125.

[221] Jeong, H.; Le, D. H.; Lim, D.; Phon, R.; Lim, S. Reconfigurable metasurfaces for frequency selective absorption. *Adv. Opt. Mater.* **2020**, *8*, 1902182.

[222] Li, W.; Wu, T. L.; Wang, W.; Zhai, P. C.; Guan, J. G. Broadband patterned magnetic microwave absorber. *J. Appl. Phys.* **2014**, *116*, 044110.

[223] Tong, X. C. *Functional Metamaterials and Metadevices*; Springer: Cham, 2018.

[224] Li, W. W.; Xu, M. Z.; Xu, H. X.; Wang, X. W.; Huang, W. Metamaterial absorbers: From tunable surface to structural transformation. *Adv. Mater.* **2022**, *34*, 2202509.

[225] Yu, P.; Besteiro, L. V.; Huang, Y. J.; Wu, J.; Fu, L.; Tan, H. H.; Jagadish, C.; Wiederrecht, G. P.; Govorov, A. O.; Wang, Z. M. Broadband metamaterial absorbers. *Adv. Opt. Mater.* **2019**, *7*, 1800995.

[226] Hannan, S.; Islam, M. T.; Soliman, M. S.; Mohd Sahar, N. B.; Jit Singh, M. S.; Faruque, M. R. I.; Alzamil, A. A Filling-factor engineered, perfect metamaterial absorber for multiple applications at frequencies set by IEEE in C and X bands. *J. Mater. Res. Technol.* **2022**, *19*, 934–946.

[227] Zhang, C.; Cheng, Q.; Yang, J.; Zhao, J.; Cui, T. J. Broadband metamaterial for optical transparency and microwave absorption. *Appl. Phys. Lett.* **2017**, *110*, 143511.

[228] Pang, Y. Q.; Wang, J. F.; Cheng, Q.; Xia, S.; Zhou, X. Y.; Xu, Z.; Cui, T. J.; Qu, S. B. Thermally tunable water-substrate broadband metamaterial absorbers. *Appl. Phys. Lett.* **2017**, *110*, 104103.

[229] Sun, L. K.; Cheng, H. F.; Zhou, Y. J.; Wang, J. Design of a lightweight magnetic radar absorber embedded with resistive FSS. *IEEE Antennas Wirel. Propag. Lett.* **2012**, *11*, 675–677.

[230] Winson, D.; Choudhury, B.; Selvakumar, N.; Barshilia, H.; Nair, R. U. Design and development of a hybrid broadband radar absorber using metamaterial and graphene. *IEEE Trans. Antennas Propag.* **2019**, *67*, 5446–5452.

[231] Panwar, R.; Lee, J. R. Progress in frequency selective surface-based smart electromagnetic structures: A critical review. *Aerosp. Sci. Technol.* **2017**, *66*, 216–234.

[232] Costa, F.; Monorchio, A. A frequency selective radome with wideband absorbing properties. *IEEE Trans. Antennas Propag.* **2012**, *60*, 2740–2747.
[233] Li, W. W.; Chen, M. J.; Zeng, Z. H.; Jin, H.; Pei, Y. M.; Zhang, Z. Broadband composite radar absorbing structures with resistive frequency selective surface: Optimal design, manufacturing and characterization. *Compos. Sci. Technol.* **2017**, *145*, 10–14.
[234] Zhang, Z.; Wang, C. X.; Yang, H. Y.; Wang, P. D.; Chen, M. J.; Lei, H. S.; Fang, D. N. Broadband radar absorbing composites: Spatial scale effect and environmental adaptability. *Compos. Sci. Technol.* **2020**, *197*, 108262.
[235] Shen, Y.; Zhang, J. Q.; Meng, Y. Y.; Wang, Z. L.; Pang, Y. Q.; Wang, J. F.; Ma, H.; Qu, S. B. Merging absorption bands of plasmonic structures via dispersion engineering. *Appl. Phys. Lett.* **2018**, *112*, 254103.
[236] Tao, J. Q.; Xu, L. L.; Pei, C. B.; Gu, Y. S.; He, Y. R.; Zhang, X. F.; Tao, X. W.; Zhou, J. T.; Yao, Z. J.; Tao, S. F. et al. Catfish effect induced by anion sequential doping for microwave absorption. *Adv. Funct. Mater.* **2023**, *33*, 2211996.
[237] Zhou, Q.; Yin, X. W.; Ye, F.; Liu, X. F.; Cheng, L. F.; Zhang, L. T. A novel two-layer periodic stepped structure for effective broadband radar electromagnetic absorption. *Mater. Des.* **2017**, *123*, 46–53.
[238] Zhang, C.; Yin, S.; Long, C.; Dong, B. W.; He, D. P.; Cheng, Q. Hybrid metamaterial absorber for ultra-low and dual-broadband absorption. *Opt. Express* **2021**, *29*, 14078–14086.
[239] Zhang, K. L.; Zhang, J. Y.; Hou, Z. L.; Bi, S.; Zhao, Q. L. Multifunctional broadband microwave absorption of flexible graphene composites. *Carbon* **2019**, *141*, 608–617.
[240] Huang, Y. X.; Song, W. L.; Wang, C. X.; Xu, Y. N.; Wei, W. Y.; Chen, M. J.; Tang, L. Q.; Fang, D. N. Multi-scale design of electromagnetic composite metamaterials for broadband microwave absorption. *Compos. Sci. Technol.* **2018**, *162*, 206–214.
[241] Zhou, Q.; Shi, T. T.; Xue, B.; Gu, S. Y.; Ren, W.; Ye, F.; Fan, X. M.; Du, L. F. Multi-scale integrated design and fabrication of ultra-broadband electromagnetic absorption utilizing multi-walled carbon nanotubes-based hierarchical metamaterial. *Compos. Sci. Technol.* **2023**, *232*, 109877.
[242] Duan, Y. B.; Liang, Q. X.; Yang, Z.; Li, Z. H.; Yin, H. Y.; Cao, Y.; Li, D. C. A wide-angle broadband electromagnetic absorbing metastructure using 3D printing technology. *Mater. Des.* **2021**, *208*, 109900.
[243] Wang, T. T.; Lu, X. F.; Wang, A. A review: 3D printing of microwave absorption ceramics. *Int. J. Appl. Ceram. Technol.* **2020**, *17*, 2477–2491.
[244] Zhou, R.; Wang, Y. S.; Liu, Z. Y.; Pang, Y. Q.; Chen, J. X.; Kong, J. Digital light processing 3D-printed ceramic metamaterials for electromagnetic wave absorption. *Nano-Micro Lett.* **2022**, *14*, 122.
[245] Wang, J. Q.; Wu, Z.; Xing, Y. Q.; Li, B. J.; Huang, P.; Liu, L. Multi-scale design of ultra-broadband microwave metamaterial absorber based on hollow carbon/MXene/Mo_2C microtube. *Small*, in press, https://doi.org/10.1002/smll.202207051.
[246] Yang, R. B.; Yang, J. J.; Lo, S. T. Wideband square spiral metamaterial absorbers based on flaky carbonyl iron/epoxy composites. *AIP Adv.* **2020**, *10*, 015141.
[247] Li, W.; Wu, T. L.; Wang, W.; Guan, J. G.; Zhai, P. C. Integrating non-planar metamaterials with magnetic absorbing materials to yield ultra-broadband microwave hybrid absorbers. *Appl. Phys. Lett.* **2014**, *104*, 022903.
[248] Shen, Y.; Zhang, J. Q.; Wang, W. J.; Pang, Y. Q.; Wang, J. F.; Ma, H.; Qu, S. B. Integrating absorber with non-planar plasmonic structure for *k*-vector matching absorption enhancement. *J. Appl. Phys.* **2018**, *124*, 225101.
[249] Liu, Y.; Zhao, K.; Drew, M. G. B.; Liu, Y. A theoretical and practical clarification on the calculation of reflection loss for microwave absorbing materials. *AIP Adv.* **2018**, *8*, 015223.
[250] Liu, Y.; Lin, Y. R.; Zhao, K.; Drew, M. G. B.; Liu, Y. Microwave absorption properties of Ag/$NiFe_{2-x}Ce_xO_4$ characterized by an alternative procedure rather than the main stream method using "reflection loss". *Mater. Chem. Phys.* **2020**, *243*, 122615.
[251] Xie, P. T.; Li, H. Y.; He, B.; Dang, F.; Lin, J.; Fan, R. H.; Hou, C. X.; Liu, H.; Zhang, J. X.; Ma, Y. et al. Bio-gel derived nickel/carbon nanocomposites with enhanced microwave absorption. *J. Mater. Chem. C* **2018**, *6*, 8812–8822.
[252] Nan, C. W.; Shen, Y.; Ma, J. Physical properties of composites near percolation. *Annu. Rev. Mater. Res.* **2010**, *40*, 131–151.
[253] Lv, H. L.; Guo, Y. H.; Wu, G. L.; Ji, G. B.; Zhao, Y.; Xu, Z. J. Interface polarization strategy to solve electromagnetic wave interference issue. *ACS Appl. Mater. Interfaces* **2017**, *9*, 5660–5668.
[254] Quan, B.; Liang, X. H.; Ji, G. B.; Cheng, Y.; Liu, W.; Ma, J. N.; Zhang, Y. N.; Li, D. R.; Xu, G. Y. Dielectric polarization in electromagnetic wave absorption: Review and perspective. *J. Alloys Compd.* **2017**, *728*, 1065–1075.
[255] Qin, M.; Zhang, L. M.; Wu, H. J. Dielectric loss mechanism in electromagnetic wave absorbing materials. *Adv. Sci.* **2022**, *9*, 2105553.
[256] Liu, Q. H.; Cao, Q.; Zhao, X. B.; Bi, H.; Wang, C.; Wu, D. S.; Che, R. C. Insights into size-dominant magnetic microwave absorption properties of CoNi microflowers via off-axis electron holography. *ACS Appl. Mater. Interfaces* **2015**, *7*, 4233–4240.
[257] Green, M.; Liu, Z.; Xiang, P.; Tan, X.; Huang, F.; Liu, L.; Chen, X. Ferric metal-organic framework for microwave absorption. *Mater. Today Chem.* **2018**, *9*, 140–148.
[258] Lv, H. L.; Yang, Z. H.; Wang, P. L.; Ji, G. B.; Song, J. Z.; Zheng, L. R.; Zeng, H. B.; Xu, Z. J. A voltage-boosting strategy enabling a low-frequency, flexible electromagnetic wave absorption device. *Adv. Mater.* **2018**, *30*, 1706343.
[259] Jia, Z. R.; Lan, D.; Lin, K. J.; Qin, M.; Kou, K. C.; Wu, G. L.; Wu, H. J. Progress in low-frequency microwave absorbing materials. *J. Mater. Sci.: Mater. Electron.* **2018**, *29*, 17122–17136.
[260] Duan, B. F.; Zhang, J. M.; Wang, G. W.; Wang, P.; Wang, D.; Qiao, L.; Wang, T.; Li, F. S. Microwave absorption properties of easy-plane anisotropy Fe-Si powders with surface modification in the frequency range of 0.1–4 GHz. *J. Mater. Sci.: Mater. Electron.* **2019**, *30*, 13810–13819.
[261] Pang, H.; Duan, Y.; Gao, M.; Huang, L.; Liu, X.; Li, Z. Electromagnetic wave absorption performance of $FeCoNiMn_{0.5}Al_{0.2}$ high entropy alloys governed by nanocrystal evolution. *Mater. Today Nano* **2022**, *20*, 100243.
[262] Qiao, M. T.; Lei, X. F.; Ma, Y.; Tian, L. D.; Su, K. H.; Zhang, Q. Y. Well-defined core–shell Fe_3O_4@polypyrrole composite microspheres with tunable shell thickness: Synthesis and their superior microwave absorption performance in the Ku band. *Ind. Eng. Chem. Res.* **2016**, *55*, 6263–6275.
[263] Chen, Z. M.; Zhang, Y.; Wang, Z. D.; Wu, Y.; Zhao, Y.; Liu, L.; Ji, G. B. Bioinspired moth-eye multi-mechanism composite ultra-wideband microwave absorber based on the graphite powder. *Carbon* **2023**, *201*, 542–548.
[264] Green, M.; Van Tran, A. T.; Chen, X. B. Obtaining strong, broadband microwave absorption of polyaniline through data-driven materials discovery. *Adv. Mater. Interfaces* **2020**, *7*, 2000658.
[265] Green, M.; Van Tran, A. T.; Chen, X. B. Maximizing the microwave absorption performance of polypyrrole by data-driven discovery. *Compos. Sci. Technol.* **2020**, *199*, 108332.
[266] Green, M.; Van Tran, A. T.; Chen, X. B. Realizing maximum microwave absorption of poly(3, 4-ethylenedioxythiophene) with a data-driven method. *ACS Appl. Electron. Mater.* **2020**, *2*, 2937–2944.
[267] Xu, X. Q.; Ran, F. T.; Fan, Z. M.; Cheng, Z. J.; Xie, Z. M.; Lv, T.; Liu, Y. Y. Microstructural engineering of flexible and broadband microwave absorption films with hierarchical superstructures derived from bimetallic metal-organic framework. *Carbon* **2021**, *178*, 320–331.
[268] Lv, H. L.; Yang, Z. H.; Xu, H. B.; Wang, L. Y.; Wu, R. B. An electrical switch-driven flexible electromagnetic absorber. *Adv. Funct. Mater.* **2020**, *30*, 1907251.
[269] Cheng, Y.; Seow, J. Z. Y.; Zhao, H. Q.; Xu, Z. J.; Ji, G. B. A flexible and lightweight biomass-reinforced microwave absorber.

Nano-Micro Lett. **2020**, *12*, 125.
[270] Chambers, B. A smart radar absorber. *Smart Mater. Struct.* **1999**, *8*, 64–72.
[271] Llorente-Romano, S.; Garca-Lampérez, A.; Sarkar, T. K.; Salazar-Palma, M. An exposition on the choice of the proper S parameters in characterizing devices including transmission lines with complex reference impedances and a general methodology for computing them. *IEEE Antennas Propag. Mag.* **2013**, *55*, 94–112.
[272] Momeni-Nasab, M.; Bidoki, S. M.; Hadizadeh, M.; Movahhedi, M. Fabrication of electromagnetic waves absorbing material by ink-jet printing method. *J. Mater. Sci.: Mater. Electron.* **2020**, *31*, 7093–7099.
[273] Wang, T.; Han, R.; Tan, G. G.; Wei, J. Q.; Qiao, L.; Li, F. S. Reflection loss mechanism of single layer absorber for flake-shaped carbonyl-iron particle composite. *J. Appl. Phys.* **2012**, *112*, 104903.
[274] Spain, E.; Venkatanarayanan, A. Review of physical principles of sensing and types of sensing materials. *Compr. Mater. Process.* **2014**, *13*, 5–46.
[275] Wang, H.; Yang, L.; Zhang, X. N.; Ang, M. H. Permittivity, loss factor and Cole–Cole model of acrylic materials for dielectric elastomers. *Results Phys.* **2021**, *29*, 104781.
[276] Ji, J. D.; Huang, Y.; Yin, J. H.; Zhao, X. C.; Cheng, X. W.; He, S. L.; Li, X.; He, J.; Liu, J. P. Synthesis and electromagnetic and microwave absorption properties of monodispersive Fe_3O_4/α-Fe_2O_3 composites. *ACS Appl. Nano Mater.* **2018**, *1*, 3935–3944.
[277] Aharoni, A. Exchange resonance modes in a ferromagnetic sphere. *J. Appl. Phys.* **1991**, *69*, 7762–7764.
[278] Wang, H.; Dai, Y. Y.; Gong, W. J.; Geng, D. Y.; Ma, S.; Li, D.; Liu, W.; Zhang, Z. D. Broadband microwave absorption of CoNi@C nanocapsules enhanced by dual dielectric relaxation and multiple magnetic resonances. *Appl. Phys. Lett.* **2013**, *102*, 223113.
[279] Xue, J. M.; Yin, X. W.; Ye, F.; Zhang, L. T.; Cheng, L. F. Theoretical prediction and experimental verification on EMI shielding effectiveness of dielectric composites using complex permittivity. *Ceram. Int.* **2017**, *43*, 16736–16743.